IRCASE 2020

INTERNATIONAL RESEARCH CONFERENCE ON APPLIED SCIENCES AND ENGINEERING 2020 (IRCASE 2020)

eISBN: 978-967-2426-20-2

13-14 December 2020

Proceeding:
International Research Conference on Applied Sciences and Engineering 2020
(IRCASE 2020)

13 – 14 December 2020

eISBN: 978-967-2426-20-2

Published By:

GLOBAL ACADEMIC EXCELLENCE
(M) SDN BHD -1257579-U

Lot 1156 Tingkat 2 Kompeni Niaga LUTH
Jalan Dato Pati, 15000 Kota Bharu ,
Kelantan, MALAYSIA
Website: www.egax.org
Email: publication@egax.org

Contents

International Research Conference on Applied Sciences
and Engineering 2020 (IRCASE 2020)
eISBN 978-967-2426-20-2
13th – 14th December 2020

RISK ASSESSMENT IN CHEMISTRY LABORATORY, FACULTY OF CHEMICAL ENGINEERING, UITM PASIR GUDANG CAMPUS

Salmi Nur Ain Sanusi[1]
Siti Hajar Anaziah Muhamad[1]
Sharifah Iziuna Sayed Jamaludin[1]
Mohd Zaki Sukor [1]
Wan Hasnidah Wan Osman[2]

[1]Faculty of Chemical Engineering, Universiti Teknologi MARA (UiTM) Johor Branch, Pasir Gudang Campus, Malaysia, (E-mail: salmi7612@uitm.edu.my)
[2]Faculty of Bioengineering and Technology, Universiti Malaysia Kelantan, (UMK), Malaysia, (E-mail: hasnidah.osman@umk.edu.my)

Abstract: *Accident can happen anytime and anywhere. To avoid the accident, the hazard must be reduced and controlled. In this study, the method of Hazard Identification, Risk Assessment and Risk Control (HIRARC) was used in order to minimise the hazard. This study was conducted in Chemistry Laboratory, Faculty of Chemical Engineering, UiTM Pasir Gudang Campus. This laboratory was chosen because most of the first-year students did their experiments which involved chemicals and apparatus in this laboratory. This study started with identified the potential hazards, followed by risk assessment, which is to calculate the risk level and lastly implementing the risk control, if necessary. From the results obtained, there were 8 major routine activities in this laboratory. The highest risk level value was 6, which contributed from 3 activities. The activities are handling chemicals in the fume hood, disposing acidic waste chemicals and preparing solutions. There are some recommended controls measures need to be implemented to make sure the risk level can be reduced in the future. In conclusion, the HIRARC method used in this study is a useful method to identify the potential hazard in order to minimised the accident rate.*

Keywords: *Hazard Identification, Risk Assessment, HIRARC*

Introduction

Laboratories, as well as other workplace is the place where the work conducted is exposed to hazards and risk. Due to the hazardous operations in laboratories, it is exposed to accident and has potential of injuries, illness and damage (Lehmann et al., 2009) (Dodo et al., 2020). Laboratories in any institution require students and staff to conform with basic safety principles to reduce injuries and accidents. The laboratories must contain sufficient space and special design according to the nature of the laboratories themselves (Al-Obaidi et al., 2018) to minimize the potential accidents.

To overcome and reduce the number of accidents, Department of Occupational Safety and Health (DOSH), an organization's body under the Ministry of Human Resources is responsible to ensure a safe environment, safety and health of the worker at the workplace. DOSH always conduct investigation every month by sector or state to analyze the accident rate and the factor that contribute to the accident. According to DOSH guidelines, Hazard Identification, Risk Assessment and Risk Control (HIRARC) is a method used to identify all the hazards, risks and introduce preventive measures so that the risks can be reduced or controlled. Identifying hazard and accessing risks are important to reduce the probability of accidents and should be a big issue (Barahim 2010) (Rout & Sikdar 2017). Not only that, but it can also avoid incidents that are costly, time consuming, stressful and inconvenient (Ahmad et al., 2016).

Risk is important to be quantified and assessed in support for risk management. Organizations that have already carried out risk assessment in their work, have experienced positive changes in their practice (Shuaib et al., 2009). The risk assessment process should be continuous performed and should not be regarded as a one-off practice.

HIRARC consist of Hazard Identification, Risk Assessment and Risk Control. Hazard identification is the process of examining each work area and work task for the purpose of identifying all the potential hazards (Ahmad et al., 2016). Risk assessment is the process after the potential hazards being identified. Risk assessment is the process where the level of risk will be categorized based on risk matrix (DOSH, 2008). Lastly, risk control will be implemented if necessary, depends on the level of the risk.

In this study, HIRARC was conducted in Chemistry Laboratory, Faculty of Chemical Engineering, UiTM Pasir Gudang Campus to determine the risk level. Chemistry Laboratory in this institution is the laboratory where most first-year students did their experiments. Normally they will be involved with chemicals and apparatus in this laboratory. This study was conducted in the hope of preventing unwanted incident as reported by some researchers.

Al-Dahhan et al. (2017) reported that some unwanted incidents happened in the fume cupboard/hood in their chemistry laboratories because of the maintenance issues. The periodic maintenance of fume cupboard is an essential part to avoid the degradation capacity of the ventilation, in turn can reduce the accident. The study conducted by Hussein et al. (2017) revealed some accidents happened in their chemical laboratory in 2016 due to lack of maintenance and safety test by qualified personnel. The accident was chemical spillage, accompanied by water flood. This accident was caused by a blocked sink while a rusty and old water tap was dripping water for at least 19 hours before the accident.

Due to these reasons, this paper was discussed about risk assessment in Chemistry Laboratory, Faculty of Chemical Engineering, UiTM Pasir Gudang Campus. The risk assessment is important to implemented in this laboratory because first-year students need to be exposed to safety precautions at the initial stage.

Methodology

Method used in this study as shown in flowchart from Figure 1 below.

Figure 1: Methodology Step

Hazard Identification

To identify type of hazards exist in the laboratories, observations have been made by the team members with the cooperation of Assistant Science Officers who are familiar with the equipment’s, materials and all the possible hazards. The hazards being identified from the activities that almost done by students in this laboratory. Risk identification is the basis of risk management (Li et al., 2019).

Risk Assessment

Risk assessment refers to the possibility of quantitatively measuring the impact or loss caused by a particular phenomenon associated with the activities (Li et al., 2019). The identified hazards will be rated in two terms; likelihood and severity. Likelihood indicates the number of event's occurrence in certain time. It is assessed based on the experience, analysis and measurement (Shuaib et al., 2009). Likelihood (L) has rating from 'most likely' to 'inconceivable'. Table 1 shows the rating for likelihood.

Table 1: Likelihood and Rating

Likelihood (L)	Classification	Rating
Most likely	The most likely result of the hazard/event being realized	5
Possible	Has a good chance of occurring and is not unusual	4
Conceivable	Might be occur at some time in future	3
Remote	Has not been known to occur after many years	2
Inconceivable	Is practically impossible and has never occurred	1

Source: (Department of Occupational Safety and Health, Ministry of Human Resource, 2008)

Severity (S) indicates the level of effects on health, environment or equipment. It can be divided into five categories which are negligible, minor, serious, fatal and catastrophic. The explanation for severity as shown in Table 2.

Table 2: Severity and Rating

Severity (S)	Classification	Rating
Catastrophic	Numerous fatalities, uncoverable property damage	5
Fatal	Approximately one single fatality, major property damage	4
Serious	Non-fatal injury, permanent disability	3
Minor	Disabling but not permanent injury	2
Negligible	Minor abrasions, bruises. Cuts, first aid type injury	1

Source: (Department of Occupational Safety and Health, Ministry of Human Resource, 2008)

Risk of each hazard can be calculated by using Equation 1 below. The equation helps to categorize the hazard either at high, medium or low level.

$$R = Likelihood\ (L)\ x\ Severity(S) \qquad (1)$$

Table 3 below shows the Risk Matrix values which consists of likelihood (L) and severity (S). Risk matrix ranking is a common tool used for risk assessment in many industries (Muniandy, 2015). There are three risk levels which are high (red), medium (yellow) and low (green).

Table 3: Risk Matrix

	Severity (S)				
Likelihood (L)	1	2	3	4	5
5	5	10	15	20	25
4	4	8	12	16	20
3	3	6	9	12	15
2	2	4	6	8	10
1	1	2	3	4	5

Source: (Department of Occupational Safety and Health, Ministry of Human Resource, 2008)
Risk level: 15-25 = high
5-12 = medium
1-4 = low

Risk Control

Risk control is a step or improvement that need to be done in order to avoid risk at the workplace. Risk control is the last step in HIRARC flow chart because it is run when all the previous methodology is done. To implement the control measures of hazard, hierarchy of control is provided, and it has five parts which are elimination, substitution, engineering control, administrative control and Personal Protective Equipment (PPE). Implementing risk control for every hazard need to follow the hierarchy of control (Agwu, 2012 and Adiputra, 2015) as shown in Figure 2.

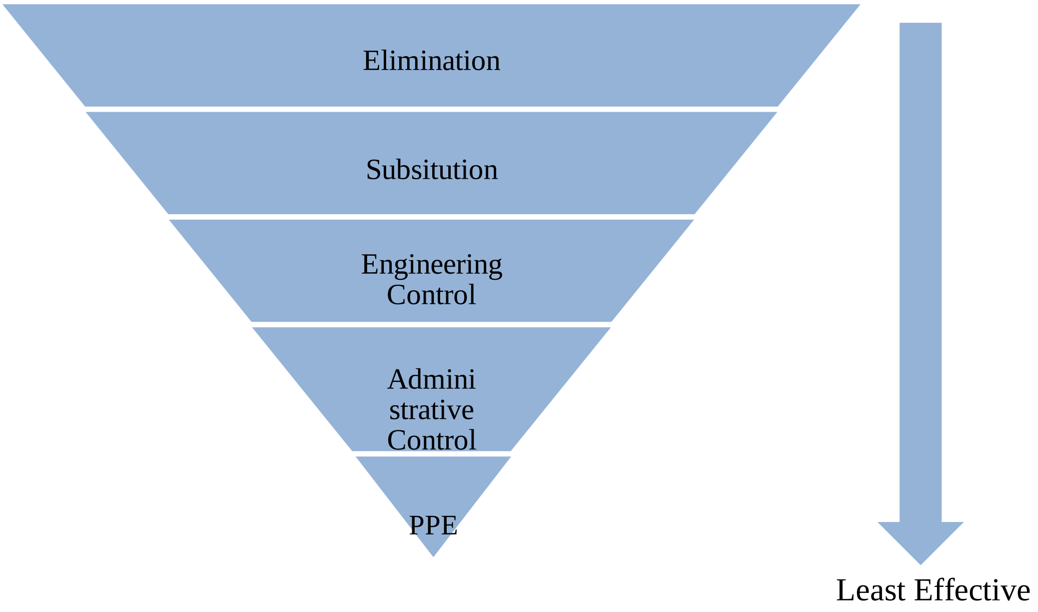

Figure 2: Hierarchy of Controls

Source: (National Institute for Occupational Safety and Health)

Results and Discussion

The results of risk level in Chemistry Laboratory was shown in Table 4. The risk level was ranked based on risk matrix. There are some activities and possible hazards occurred in this laboratory.

Table 4: Risk Level of Hazard in Chemistry Laboratory

Activity	Potential Hazard	Risk Level
Handling chemical in the fume chamber	Hazardous material exposure	6 (Medium)
Disposing acidic waste chemical	Reactions from harmful chemical	6 (Medium)
Preparing solution	Hazardous material exposure	6 (Medium)
Heating or drying process in the oven	High temperature tray in the oven	4 (Low)
Titration process	Potentially harmful chemical	2 (Low)

As shown from the table, the risk level for all potential hazards is in the medium and low range. For an activity that use chemicals like handling chemicals in the fume hood, disposing acidic waste chemicals and preparing a solution, there are some potential hazards that might be occurred. The risk level for all activities mention above is 6, which is in the medium range. Based on DOSH (2008), if the risk level is medium, it is suggested to implement a temporary control measures to avoid the accident.

The person who handle chemicals in fume hood and prepare a solution can have the potential of being exposed to the hazardous chemicals. So, to avoid from any accident happen, it is suggested that the person need to wear proper personal protective equipment (PPE) like thick gloves, safety glasses and safety shoes. The person needs to know the suitable PPE before they want to handle any chemicals. The study conducted by Dodo et al. (2020) also revealed that the users in laboratories must have knowledge on potential hazards to increase the safety awareness and practices.

For an activity of disposing acidic waste chemicals, the potential hazard that may occur is reactions may occur between harmful chemicals. The risk level for this potential hazard also 6. To avoid from any undesired event, it is recommended that all waste containers is clear and properly label to avoid any confusion from users. This control measure also agrees with study conducted by Al-Obaidi et al. (2018). From the study, they suggested that clear labelling system and proper storage is important in postgraduate laboratories that have many different types of chemicals. Other than that, in this chemistry laboratory, all containers need to be separated based on their category and the user need to clear up all the spillage immediately (if any) as some of safety precautions. All recommendations mentioned above is under administrative control in hierarchy of control.

Another two activities in this chemistry laboratory have the low risk level. The activities are heating or drying samples in the oven and titration process. For low risk level, the hazard may be considered as acceptable and further reduction may not be necessary (DOSH, 2008).

Overall, the finding in this study which is medium and low risk level were aligned with studies conducted by Shuaib et al. (2009) and Ibrahim et al. (2019). From their studies, they also conducted risk assessment in the laboratory at their institution and found the results is in low and medium range.

Conclusion

In conclusion, this chemistry laboratory in Faculty of Chemical Engineering, UiTM Pasir Gudang Campus has medium and low range of risk level. The value of risk level 6 (medium) is somehow near to low risk level. However, it is strongly recommended that safety precautions need to be taken to make sure the safety of people in this laboratory is at the top level and to avoid any accident happen in the future. Further studies also need to focus more on other laboratories due to variations of hazards and risks.

Acknowledgment

This research is supported by Geran Penyelidikan Bestari Sepadanan Fasa 1/2020 UiTM Cawangan Johor. The author also would like to thank all technical teams, Faculty of Chemical Engineering, UiTM Pasir Gudang Campus for their support throughout this study.

References

Adiputra, M.F. 2015. Risk Control Enhancement Using Safety Climate Factors for HIARC Method in Steel Product Industry. Thesis Dissertation, University Technology of Malaysia.

Agwu, M. O. 2012. The Effects of Risk Assessment (HIRARC) on Organisational Performance in Selected Construction Companies in Nigeria. British Journal of Economics Management & Trades, 2(3). pp. 212–224.

Ahmad, A.C., Nianti, I., Zin, M., Othman, M.K., and Muhamad, N.H. 2016. Hazard Identification, Risk Assessment and Risk Control (HIRARC) Accidents at Power Plant. MATEC Web of Conferences, 66. pp. 1–6.

Al-Dahhan, W.H, Abd Ali, A., and Yousif, E. 2017. Lack of Maintenance in a Chemical Laboratory has Almost Caused an Accident. Open Access Journal of Chemistry. 1(1). pp 63-66.

Al-Obaidi, O., Abdallh, M., Al-Dahhan, W.H., Yusop, R., Ahmed, A., and Yousif, E. 2018. Risk Assessment in Postgraduate Laboratories. Journal Public Health Catalog, 1(3). pp 1-4.

Barahim, F. 2010. Hazard Identification, Risk Assessment and Risk Control (HIRARC) in a Corrugated Box. Thesis Dissertation, University of Malaya.

Department of Occupational Safety and Health, Ministry of Human Resource. 2008. Guideline for Hazard Identification, Risk Assessment and Risk Control.

Dodo, S.M., Abdulkadir, S.A., Malgwi, G.S., Ibrahim, V., and Jahun, B.G. 2020. Hazard Identification and Risk Assessment in Material Engineering Laboratory. World Academics Journal of Engineering Sciences, 7(2). pp 45-50.

Hussein, F.H, Al-Dahhan, W.H, Al-Zuhairi, A.J., Rodda, K.E., and Yousif, E. 2017. Maintenance and Testing of Fume Cupboard. Open Journal of Safety and Technology, 7. pp 69-75

Ibrahim, M.Z., Abu Samah, M.A., Zulkifly, A.H., and Mohd Jan, N.H. 2019. Development of OSH Risk Assessment in IIUM Orthopaedics Research Laboratory According to ISO/IEC 17025:2017 Accreditation. International Journal of Recent Technology and Engineering, 8(1C2) pp. 260-265

Lehmann, C.C., Haight, J.M., and Michael, J.H., 2009. Effects of Safety Training on Risk Tolerance: An Examination of Male Workers in The Surface Mining Industry. Journal of SH&E Research, 4(3) pp. 1-22.

Li, N., Hu, L., Jin, A., and Li, J. 2019. Biosafety Laboratory Risk Assesssment. Journal of Biosafety and Biosecurity, 1(2019) pp. 90-92.

Muniandy, K. 2015. HIRARC Study for Occupational Safety and Health Evaluation of Clinical Waste Handlers at A Hospital and an Incineration Plant", Thesis Dissertation, University of Malaya.

National Institute for Occupational Safety and Health, https://www.cdc.gov/niosh/topics/hierarchy/default.html

Rout, B.K. and Sikdar, B.K. 2017. Hazard Identification, Risk Assessment and Control Measures as an Effective Tool of Occupational Health Assessment of Hazardous Process in An Iron Ore Pelletizing Industry. Indian Journal of Occupational & Environmental Medicine. 21:56-76.

Shuaib, N.A., Ghazali, M.F., Asyraf, C.D.M., and Azmi, H. 2009. Applications of HIRARC at UniMAP Laboratories. National Symposium on Advancements in Ergonomics and Safety, pp. 167-171.

International Research Conference on Applied Sciences
and Engineering 2020 (IRCASE 2020)
eISBN 978-967-2426-20-2
13th – 14th December 2020

EXPERIMENTAL PERFORMANCE ANALYSIS OF A DIRECT EVAPORATIVE COOLER

Zulkurnain Bin Hassan[1]
Dr Mohd Suffian Bin Misaran@Misran [2]
Nancy Julius Siambun[3]

[1]Faculty of Engineering, Universiti Malaysia Sabah (UMS), Malaysia, (E-mail: zulkurnainhassan@gmail.com)
[2]Faculty of Engineering, Universiti Malaysia Sabah (UMS), Malaysia, (E-mail: suffian@ums.edu.my)
[3]Faculty of Engineering, Universiti Malaysia Sabah (UMS), Malaysia, (E-mail: nancyjs@ums.edu.my)

Abstract: *In recent years, the direct evaporative cooler has been introduced because of low energy consumption and easy maintenance. The evaporative cooling system is useful in places where the climate is hot and dry. The objective of this work is to investigate the performance of an evaporative cooler in hot and humid regions. The performance of a direct evaporative cooling system is evaluated with different operating conditions. Rectangular shaped honeycomb cooling pads with a length of 26 cm, width of 20 cm and thickness of 5 cm is used as a cooling media. Parameters for the performance assessment were inlet temperature, saturation efficiency, cooler capacity, feasibility index and output temperature. The results showed that the output temperature of the air varies between 24.9°C and 26.7°C, while the cooling capacity is between 1.06 kW and 2.08 kW and saturation efficiency between 67.23% to 77.27% is achievable. The results showed that evaporative cooling is achievable with feasibility index $11.86 \leq F^* \leq 17.84$. The results show that the evaporative cooler can reduce dry bulb temperature up to a maximum of 7.6°C with relative humidity in the range of 68% to 77%. The results also affirmed that cooler capacity and the saturation index are higher where the feasibility indexes are comparatively low.*

Keywords: *Direct Evaporative Cooler, feasibility index, performance, saturation efficiency, cooler capacity*

Introduction

The surrounding air temperature is gradually increasing day by day due to global warming, making its uncomfortable to stay in a room without a proper cooling system. Air conditioners are becoming a primary home appliance across the world to transform the indoor condition to the human comfort range. In order to establish human comfort zone, the indoor temperature and relative humidity play a major role. Room with a temperature of 25 ◦C and 55% relative humidity is considered to be under comfortable zone (ANSI/ASHRAE standard 55–2010)

Evaporative cooling may offer an alternative to mechanical refrigeration cooling for air conditioning, depending on the climatic conditions and building load characteristics. This concept is enhanced again at the present status when energy-saving and environment-preserving are two subjects in all engineering fields due to its characteristics of zero pollution, energy efficiency, simplicity and good indoor air quality. The evaporative cooling is an energy-saving and environmentally friendly cooling technology where the heat is absorbed and the air is cooled through the water evaporation process.

An evaporative cooler is energy savings because the only power-consuming components are fans and water pumps. By only uses water as the working fluid, an Evaporative cooler also an environmentally friendly and energy-efficient. (Foster, R. E. 2013). Evaporative cooling methods can be divided into a direct evaporative cooling (DEC) and indirect evaporative cooling (IEC), depending upon whether the air is in contact with water or not.

Malaysia, located at 3°08'20.4"N latitude and 101°41'12.8"E longitude is an equatorial country with tropical climate conditions. A tropical climate country has fairly consistent weather conditions throughout the year, where the average daytime dry bulb temperature, wet bulb temperature, and relative humidity are 32°C, 25°C and 62% respectively (C.K. Tang and N. Chin 2013). The lower relative humidity of daytime hours is indicative that evaporative cooling systems can potentially be used to lower indoor temperatures (K.P. Arandara, R.A. Attalage and M.T.R. Jayasinghe 2010).

The need for indoor cooling in Malaysia is imperative for thermal comfort and conventional air conditioning system is used in majority of buildings. Air conditioning energy consumption accounts for 49% of total energy consumption in a typical office building in Malaysia (C.K. Tang and N. Chin 2013). Therefore, there is a need to study alternative cooling solutions that require lower operational energy, and evaporative coolers are a candidate. Direct evaporative coolers consist of a fan that actively passes air through a wet cooling pad; this effectively lowers the dry bulb temperature and aids thermal comfort. The process is considered adiabatic, meaning there is no heat gain, or heat loss, because sensible heat is converted to latent heat

Many studies have dealt with the performance of direct evaporative cooling. In Malaysia Mohammad, A. T., Mat, S. B., Sulaiman, M. Y., Sopian, K., & Al-Abidi, A. A. (2013) was doing “Experimental Performance of a Direct Evaporative Cooler Operating in Kuala Lumpur”, The result shows the output temperature of the air varies between 27.5°C and 29.4° C, while the cooling capacity is between 1.384 kW and 5.358 kW

Julian Saw & Ong Rui Fong 2019 studied the Effects and Usefulness of Evaporative Cooling in Malaysia. The investigation was conducted to evaluate the effectiveness of evaporative cooling in providing human thermal comfort based on Fanger’s Predicted Mean Vote – Predicted Percentage Dissatisfied (PMV-PPD) method and Adaptive model in compliance with ASHRAE 55. The results show that the evaporative cooler can reduce dry bulb temperature up to a maximum of 6.6°C and suggest that evaporative cooling systems may be a possible cooling solution in Malaysia given the space has low heat gains.

Direct evaporative cooling efficiency effected by speed and the dry-bulb temperature of frontal air, and the temperature of the incoming water because decreased air velocity and incoming water temperature will increased with frontal air dry-bulb temperature (Chenguang and Agwu 2012)

Dai and Sumathy using (Y.J. Dai and K. Sumathy 2002) a mathematical model to predict and discuss the interface temperature of the falling film in a cross-flow direct evaporative cooler and results show that the system performance could be improved by optimizing the mass flow

rates of the feed water and processed air, as well as the different dimensions of the pad.

The smaller the Feasibility index F* evaporative cooling number, the more feasible the evaporative cooling system (R. Poku, T. W. Oyinki and E. A. Ogbonnaya 2017). It indicates the evaporative cooling potential to give thermal comfort. According to Watt, J. R (Watt, J. R. 1963), F* comfort cooling; 11 F* 16 for relief (lenitive) cooling and for F* >16 not recommended for the use of evaporative cooling systems. In Malaysia, average daytime F* is 18, just outside the recommended margins. Thus, Malaysian climate conditions are not favourable for evaporative cooling systems. This study seeks to experimentally study the effectiveness of direct evaporative cooling in providing thermal comfort.

Direct Evaporative Cooling (DEC)

The principle of DEC is to convert sensible heat to latent heat. Non-saturated air is cooled by heat and mass transfer, which increases by forcing the moment of air through an enlarged liquid water surface area for evaporation by using fans or blowers. Fig 1 shows the schematic diagram of direct evaporative cooling system where water is running in loop and the makeup water entering the sump to replace evaporated water must be at same adiabatic saturation temperature of the incoming air. In DEC, heat and mass transferred between air and water decreases the dry bulb temperature of air and increases its humidity, keeping the enthalpy constant in an ideal process.

An environmental condition such as inlet temperature and relative humidity, pad material, pad thickness and density, pad air face velocity, and water flow in pads was the factors that affect the performance of the evaporative cooling system (Ndukwu, M. C. and Manuwa, S. I. (2014).

An evaporative cooler can become more effective when temperatures are high, relative humidity is very low, water is available for the purpose and air is conductive (Rusten, E. 1985).

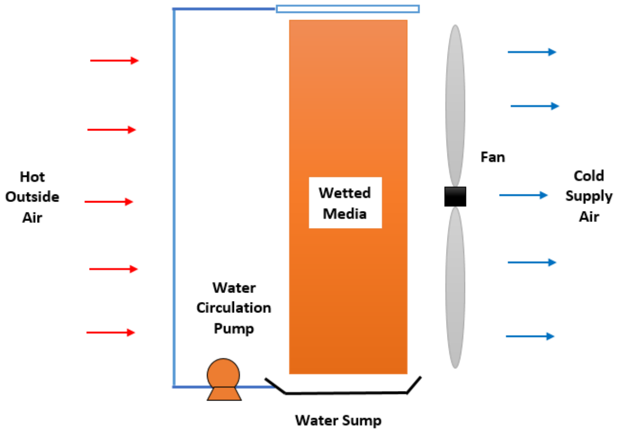

Figure 1: Schematic Diagram of Direct Evaporative Cooler

Methods and Experiment Setup

The study was carried out in Kolej Komuniti Kota Marudu, Sabah at location of 6.0367°N, 116.1186°E and the measurement was taken between 10:00 am and 03:00 p.m. The experiment was conducted in the month of October. The direct evaporative cooling that was used for study consists consisted mainly of axial fan at the end of unit and a pump to sprinkle water on the upper side of the pad. Air passes through the unit in horizontal configuration. The evaporative cooling was made of metal sheet. A honeycomb cooling pad was used as cooling media with a length of 26 cm, width of 20 cm and thickness of 5 cm. The 21-Watt axial fan were made to run at around 2500 rpm and 10-Watt, 220 V AC submersible pump has a flow rate of 800L/H

Experimental tests were carried out to evaluate the performance of the direct evaporative cooling unit. To measure the air temperature and relative humidity at inlet and outlet points of the evaporative cooling unit, readings of the two type-K thermocouples with accuracy of ± 0.1°C as well as the, dry- and wet-bulb temperatures for ambient air were recorded using the sling psychrometer. Anemometer was installed at the inlet point of the evaporative cooling unit to measure the air velocity. The mass flow rate of air entering the evaporative cooling unit was determined by using the air velocity and the cross-section area of the inlet duct. Pyrometer was used to record the solar radiation in the test location.

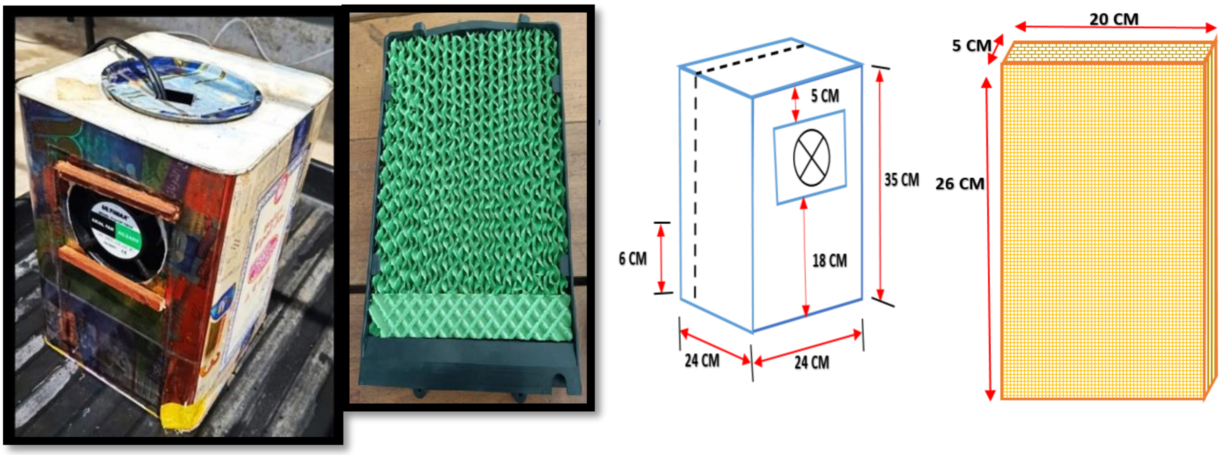

Figure 2: Photograph of a direct evaporative cooling and its pad

Performance Evaluation

The DEC cooling efficiency (ε) is defined as the ratio of the air temperature difference and the difference between dry-bulb and wet-bulb inlet air temperatures, as shown in equation (1).

$$\varepsilon = \frac{T1 - T2}{T1 - Twb} \times 100 \qquad (1)$$

The dry bulb temperature of the outlet air can be calculated using equation (2) Watt, R. J. and Brown, W. K. (1994).

$$T_2 = T_1 - \varepsilon_{DEC}(T1 - T_{wb1}) \qquad (2)$$

Cooling capacity is the rate where the heat is removed, while temperature remains constant. Cooling load or cooling capacity is calculated using equation (3).

$$Qc = m_a C_{pa} (T_1 - T_2) \qquad (3)$$

Feasibility index (F*) is specified in equation (4):

$$F^* = T_{wb} - (T_1 - T_{wb}) \qquad (4)$$

Where:
Qc = cooling capacity (kJ/h)
ma = air flow rate (kg/s)
C_{pa} = Specific heat of air (J/kgK)
T_1 = Evaporative inlet dry bulb temperature, °C
T_2 = Evaporative outlet dry bulb temperature, °C
T_{wb} = Evaporative inlet wet bulb temperature, °C

The smaller the F* number, the more feasible the evaporative cooling system. It indicates the evaporative cooling potential to give thermal comfort. The greater the difference between the two temperatures, the greater is the evaporative cooling effect. According to Watt, J.R 1963, the comfort cooling is when the F* is at ≤ 10. The relative (lenitive) cooling is when the F* is at $11 \leq F^* \leq 16$, while $F^* > 16$ is not recommended for the use of evaporative cooling systems. In Malaysia, the average daytime F* is 18, which is exceeding the recommended margins (Watt, J. R, 1963).

Result and Discussion

The constructed system was tested to assess its performance. The experimental readings of dry-bulb temperature of the inlet and outlet air, solar radiation, saturation efficiency and cooling capacity were recorded and shown in Table 1. Table 2 summaries the average, maximum and minimum values. During the experimentation, the inlet air conditions of the dry bulb temperature was between 29.5°C to 33.5°C, the air relative humidity was between 68% to 77%, and the solar radiation was between 333.5 to 903.7 W/m^2. The average air velocity during the experiments was 4.55 m/sec and the water mass flow rate was 0.2548 kg/s.

Table 1: Experimental data and the performance parameters

Time	T_1(^{0}C)	T_{WB}(^{0}C)	T_2(^{0}C)	EFFICIENCY (%)	F*	Q_C (KW)
10.00 a.m.	29.5	23.55	25.5	67.23	17.60	1.063
10.15 a.m.	29.8	23.72	25.6	69.08	17.64	1.175
10.30 a.m.	30.2	24.02	25.7	72.82	17.84	1.423
10.45 a.m.	30.4	22.77	25.2	68.15	15.14	1.551
11.00 a.m.	30.7	22.86	25.0	72.70	15.02	1.741
11.15 a.m.	31.0	23.24	25.4	72.16	15.48	1.610
11.30 a.m.	31.5	22.84	24.9	76.21	14.18	1.990
11.45 a.m.	31.7	22.73	25.6	68.00	13.76	1.640
12.00 p.m.	32.0	22.98	25.7	69.84	13.96	2.017
12.15 p.m.	32.2	23.35	25.4	76.84	14.50	1.780
12.30 p.m.	32.5	22.19	25.8	64.99	11.88	2.269
12.45 p.m.	32.8	23.12	25.9	71.28	13.44	1.908
1.00 p.m.	32.9	23.21	25.8	73.27	13.52	1.964
1.15 p.m.	32.9	22.99	25.4	75.68	13.08	1.935
1.30 p.m.	33.3	22.58	25.7	70.90	11.86	2.073
1.45 p.m.	33.3	22.63	26.0	68.42	11.96	1.991
2.00 p.m.	33.4	23.79	26.4	72.84	14.18	1.958
2.15 p.m.	33.5	23.82	26.7	70.25	14.14	2.029
2.30 p.m.	33.3	24.37	26.4	77.27	15.44	1.983
2.45 p.m.	32.8	23.32	26.0	71.73	13.84	2.103
3.00 p.m.	32.8	23.61	25.9	75.08	14.42	2.381

Table 2: Value of the experimental test for average, maximum and minimum

Technical parameters	Performance		
	Average	Max	Min
Dry-Bulb Inlet T_1 (^{O}C)	32.02	33.5	29.5
Web-bulb Inlet T_{WB} (^{O}C)	23.22	24.37	22.63
Dry-Bulb Outlet T_2 (^{O}C)	25.71	26.7	24.9
Solar Radiation (W/M^2)	620.88	903.7	333.5
Efficiency (%)	71.65	77.27	67.23
Feasibility Index (F)	14.42	17.84	11.86
Cooling Capacity Q_C (KW)	1.84	2.38	1.06
Air Velocity (m/s)	4.55	5.39	4.03
Relative humidity RH (%)	71.53	77	68

The variation of the dry bulb temperature between inlet air temperature and outlet air temperature is shown in Fig.3. It is possible to obtain a maximum temperature difference up to 7.6°C at relative humidity of 42.5 %, and minimum temperature difference up to 2.1°C at a relative humidity of 81.1%.

The variation of the dry bulb temperature between inlet air temperature and outlet air temperature is shown in Fig.3. It is noticeable that it was possible to obtain the maximum temperature difference up to 7.6°C at a relative humidity of 42.5 %, and the minimum temperature difference up to 2.1°C at a relative humidity of 81.1%.

The performance of saturation efficiency with the time is illustrates by graph in Fig. 4. The performance of an evaporative cooler was evaluated from the value of saturation efficiency. The outlet dry-bulb temperature has a direct effect on the saturation efficiency of the evaporative cooler. The variation of saturation efficiency with time is shown in Fig. 4, the efficiency is between 67.23% to 77.27% range.

Numerous researches had proven that saturation efficiency of commonly used cooling pad materials fall within 50% to 90% (Kulkarni, R. K. & Rajput, S. P. S. 2011)

The maximum saturation efficiency was recorded at the time 2:30 p.m., with a dry-bulb temperature and relative humidity of 36°C and 74%, respectively. The saturation efficiency decreases with increasing the mass flow rate of air.

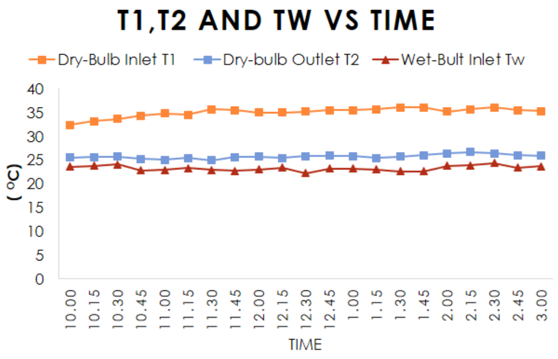

Figure. 3: Dry-bulb inlet, dry-bulb Outlet and Wet-bulb inlet with time

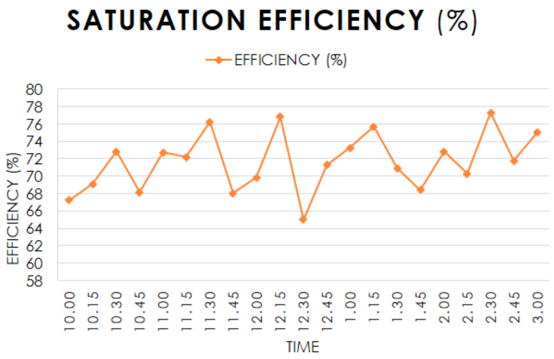

Figure. 4: Performance of saturation efficiency with the time

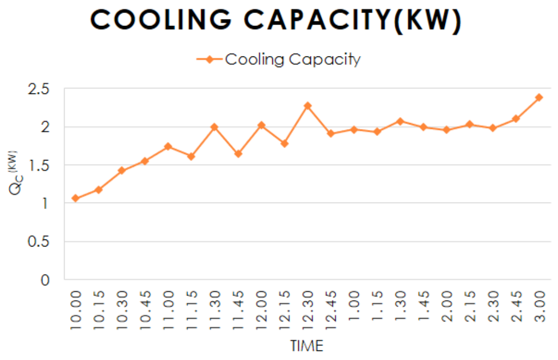

Figure. 5: Variation of cooling capacity with time

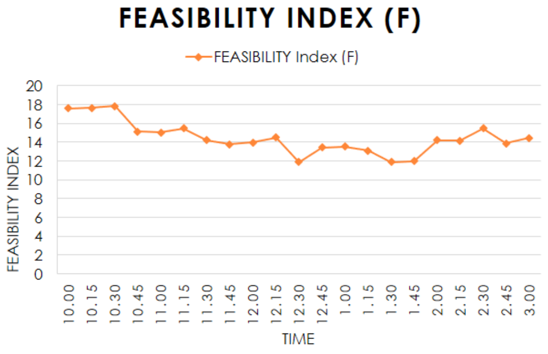

Figure 6: Variation of feasibility index with time

The variation of cooling capacity with the time of test is shown in Fig. 5. The graph plot shows that the cooling capacity varies between 1.3 kW and 5.3 kW. The maximum cooling capacity was recorded at the time 1:50 PM, while the minimum cooling capacity was recorded at the time 8:30 AM. The cooling capacity was resultant from the drop in the dry bulb temperature of air.

The variation of feasibility index with time is shown in Fig.6. The F* value remained relatively constants between 10:00 a.m. to 3:00 p.m., ranging from 11.86 to 17.84. This value is well below the F* of the average Malaysian Daytime which has F* = 18. The F* value peaked between 10:00 – 10:30 a.m. The lower the F* number, the more feasible the evaporative cooling becomes. Hence, the most effective time for the evaporative cooler operation is from 11:00 a.m. to 1:45 p.m. In other words, the greater the difference between T_1 and T_w the greater the evaporative cooling effects.

Conclusion

Evaporative air cooling system is energy efficient and can be used as an alternative to the conventional system and has a large application potential to provide thermal comfort by cooling and humidification of the ambient air at reduced operating cost. It is not only cheap solution but also sustainable and environmentally friendly for air conditioning. An experimental study was carried out to evaluate the performance of a direct evaporative cooler in humid regions.

Experimental result shows that application of direct evaporative cooling unit in hot and humid regions had successfully decreased the dry bulb temperature up to 7.6°C. The saturation efficiency varies from 67.23% to 77.27 %, and the cooling capacity ranges is between 1.06 kW to 2.08 kW. The direct evaporative cooler can be applying in humid places like Malaysia by drying the air before the evaporative process using the desiccant dehumidification concept. The evaporative air-cooling system is energy efficient and can be used as an alternative to the conventional system and has a large application potential to provide thermal comfort by cooling and humidification of the ambient air at reduced operating cost.

Acknowledgements

The authors wish to convey sincere gratitude to Universiti Malaysia Sabah (UMS) for supporting the current research work thru UMS research grant, project no. GA19100.

References

ANSI/ASHRAE standard 55–2010: Thermal Environmental Conditions for Human Occupancy, American Society for Heating, Refrigerating and Air Conditioning Engineers Inc, 1791 Tullie Circle, NE, Atlanta, GA 30329.

Chenguang Sheng and Agwu Nnanna. Empirical correlation of cooling efficiency and transport phenomena of direct evaporative cooler. Appl. Therm. Eng. 2012; 40: 48–55

C.K. Tang and N. Chin, Building Energy Efficiency Technical Guidelines for Passive Design, 1st ed. Kuala Lumpur: Building Sector Energy Efficiency Project (BSEEP), 2013, pp. 32-35.

D. H. W. Li and T. N. T. Lam, “Determining the optimum tilt angle and orientation for solar energy collection based on measured solar radiance data”, International Journal Photoenergy, Vol. 2007, Article ID

Foster, R. E. (2013) Evaporative Air-Conditioning Contributions to Reducing GreenhouseGas Emissions and Global Warming. Retrieved 10 February, 2017 from the World Wide Web: http://citeseerx.ist.psu.edu/viewdoc/download?doi=10.1.1.576.710 7&rep=rep1&type=pdf

K.P. Arandara, R.A. Attalage and M.T.R. Jayasinghe, “Thermal Comfort with Evaporative Cooling for Tropical Climates”, International Conference on Sustainable Built Environment (ICSBE-2010), December 2010.

Kulkarni, R. K. and Rajput, S. P. S. (2011) “Comparative Performance of Evaporative Cooling pads of alternative Materials”. International Journal of Advanced Engineering Sciences and Technologies, Vol. 10, Issue 2, pp 239-244.

L. Y. G. Seng, Lalchand and G. M. S. Lin, "Economical, environmental and technical analysis of building integrated photovoltaic systems in Malaysia", Energy Policy, vol. 36, No. 6, pp. 2130-42, 2008.

M. Mattei, G. Notton, C. Cristofari, M. Muselli, P. Poggi, "Calculation of the polycrystalline PV module temperature using a simple method of energy balance", Renewable Energy, vol. 31, No. 4, pp. 553–567, 2006.

Mohammad, A. T., Mat, S. B., Sulaiman, M. Y., Sopian, K., & Al-Abidi, A. A. (2013). Experimental Performance of a Direct Evaporative Cooler Operating in Kuala Lumpur. Int. J. of Thermal & Environmental Engineering, 6(1), 15–20

Ndukwu, M. C. and Manuwa, S. I. (2014) Review of Research and Application of Evaporative Cooling In Preservation of Fresh Agricultural Produce. Int J Agric & Biol Eng. Vol. 7, No.5: pp. 85-102

R. Poku, T. W. Oyinki and E. A. Ogbonnaya, "The Effects of Evaporative Cooling in Tropical Climate", American Journal of Mechanical Engineering, vol. 5, no. 4, pp. 145-150, 2017.

Rusten, E. (1985) Understanding Evaporative Cooling, Volunteers in Technical Assistance. Technical Paper #35. VITA, Virginia, USA

Sushmita, M.D., Hemant, D., and Radhacharan, V. (2008) Vegetables in Evaporative Cool Chamber and in Ambient, Macmillan Publi. Ltd., London and Basingstoke, pp. 1-10.

Watt, J. R. (1963) Evaporative air conditioning. New York: The Industrial Press, p.300

Sozen Adnan, Ozalp Mehmet, Arcaklioglu Erol. Prospects for utilisation of solar driven ejector-absorption cooling system in Turkey", Applied Thermal Engineering, vol. 24, No. 7, pp. 1019-1035, 2004.

Watt, R. J. and Brown, W. K. (1994) Evaporative Air Conditioning Hand Book, 3rd edn(The Fairmane Press Inc, Liburn GA). pp.185-189.

Y.J. Dai and K. Sumathy. Theoretical study on a crossflow direct evaporative cooler using honeycomb paper as packing material. Appl. Therm. Eng. 2002; 22: 1417– 1430

International Research Conference on Applied Sciences
and Engineering 2020 (IRCASE 2020)
eISBN 978-967-2426-20-2
13th – 14th December 2020

DYNAMIC ADSORPTION OF LEAD BY NOVEL GRAPHENE OXIDE-POLYETHERSULFONE NANOCOMPOSITE MEMBRANE IN FIXED-BED COLUMN

Nik Rashida Nik Abdul Ghani[1]
Mohammed Saedi Jami[1]

[1]Department of Biotechnology Engineering, Kuliyyah of Engineering, International Islamic University Malaysia, 53100 Kuala Lumpur

Abstract: *The existence of a high dosage of heavy metals in industrial effluents represents the greatest challenge in wastewater treatment. Of these heavy metals, lead (Pb) is recognized as a longstanding contaminant due to rapid industrialization in the semiconductor and electronics industries that are harmful to the environment and human health. The development of a modified graphene oxide nanocomposite membrane was sought as a potential adsorbent for the removal of lead ions by continuous adsorption. In this study, graphene oxide-polyethersulfone nanocomposite (GPN) membrane was fabricated via non-solvent induced phase inversion (NIPS) method where the modification of membrane was conducted by incorporating graphene oxide (GO) in the matrix polymer solution. The effect of the dynamic adsorption process was investigated together with the influence of flowrate, initial lead concentration, and bed height. The adsorption was efficient with 10 ml/min of flow rate, 100 ppm of feed concentration, and 0.06 cm of bed height in terms of the elevated adsorption capacity. The experimental adsorption data were evaluated to predict the breakthrough curve of lead adsorption onto the membrane using the Thomas model, the Bohart-Adams model, the Yoon-Nelson model, and the dose-response model. The breakthrough curves were well fitted with the Bohart-Adams model and the maximum adsorption capacity was found to be 1614 mg/g with the initial Pb concentration of 100 ppm at a flow rate of 10 ml/min. The high coefficient of determination (R^2) and the low sum of squared errors (SSE) on the Bohart-Adams models indicate a good fit of the experimental data for the effect of flowrate, feed concentration and bed height.*

Keywords: *dynamic adsorption, graphene-oxide, nanocomposite membrane, breakthrough models*

Introduction

Heavy metal pollution is one of the global problems due to rapid industrialization and urbanization. Of these heavy metals, lead (Pb) is one of the common and most toxic pollutants in natural waters. The Pb contaminants are predominantly associated with wastewater effluents from the semiconductor and electronics industries that are harmful to the environment and human health (Pramanik et al. 2016; Krause et al., 2015). An effective treatment method to overcome the contaminated wastewater by heavy metal residues remains a great challenge. Common conventional methods that had been utilized to remove heavy metals including Pb from wastewater effluents are chemical precipitation, solvent extraction, ion exchange, electrochemical removal, and coagulation. However, these methods have limitations such as inconvenient, large space needed, incomplete removal, high energy consumption low efficiency, generation of toxic sludge, and expensive disposal (Siddiqui & Chaudhry 2017; Burakov et al. 2018; Shukla et al. 2018).

Recent developments in nanotechnology and membrane technology have further increased the effectiveness of adsorbent materials providing innovative systems for improving environmental remediation. Graphene is a nanomaterial with a two-dimensional mesh of carbon atoms arranged in the form of a honeycomb lattice which is the lightest, strongest, thinnest and best heat and electricity conducting material. Significantly, the development of next-generation filtration and separation membranes using graphene-based material has stood up to scrutiny and proved to be efficient in water purification (Naushad, 2018). Graphene oxide (GO), a highly oxidized form of graphene sheet, has been investigated due to easy dispersion in aqueous solution as these oxygen moieties make GO hydrophilic (Yoon et al. 2016). The GO-based membrane becomes an emerging method in wastewater treatment because of its hydrophilicity, ease of fabrication, strong mechanical stability and industrial scale production (Mkhoyan et al., 2009; Peng et al., 2017). Therefore, this study aims to fabricate the asymmetric GO-polyethersulfone nanocomposite (GPN) membrane via a non-soluble induced phase separation (NIPS) method for lead removal. The modification of PES membrane was conducted by incorporating graphene oxide GO in the matrix polymer solution. The produced GPN membrane then was utilized for the dynamic adsorption study. Dynamic adsorption analysis is the best approach to understand the irregular flow patterns and to obtain design models that could be applicable for the commercialization of membrane systems due to the limitation of the batch adsorption system where the treatment of small volume of polluted wastewater and inaccessible authentic data for scale-up (Manirethan et al., 2019).

Materials and Methods

Materials and Chemicals

All reagents used for fabrication were analytical grade. Lead nitrate ($PbNO_3$; 99%) was purchased from R&M Chemicals. Deionized water was used as the nonsolvent for polymer precipitation and sample preparation. Commercial grade polyethersulfone (PES) (Ultrason E6020P, MW = 75,000 g mol−1 and glass transition temperature 225 °C) was supplied by BASF, Ludwigshafen, Germany. Polyvinylpyrrolidone (PVP) (MW = 40,000 g mol−1) was used as a pore-forming additive for the membrane preparation and N, N- dimethylformamide (DMF, 99.5%) as a solvent, and were all purchased from R&M chemicals, Canada. The synthesized graphene oxide was used throughout the experiment.

Fabrication of GPN membrane

The graphene oxide polymer nanocomposite (GPN) membranes were prepared by the phase inversion method according to Wang et al., (2019) with some modifications. Dimethylformamide (DMF) was used as a solvent and deionized water as the non-solvent. Firstly, GO was dispersed in DMF and sonicated for 1 h. Then, PES and polyvinylpyrrolidone (PVP) were added to the above mixture and was stirred at 50 °C for 24 h to obtain a well-dispersed casting solution. Then, the resulting homogenous casting solution was put on an ultrasonic bath and degassed to eliminate air bubbles. Subsequently, the casting solution was poured on a clean glass plate (210 × 297× 5 mm) to cast the membrane of 200 μm thickness. After 60 seconds of pre-evaporation at room temperature, it was immersed into the non-solvent bath (coagulation bath) and kept in the container for up to 24 h. The prepared membrane was washed with deionized water and then preserved in water before use.

Dynamic adsorption experimental setup

The continuous adsorption of Pb (II) by GPN membrane was conducted according to Zhang et al., (2019) with slight modification. The dynamic adsorption process was set up in a stainlesssteel cylindrical column with an inner diameter of 2.2 cm and a height of 30 cm. The fibre membranes were cut into a circle shape with an effective membrane area is 3.8 cm^2 before they were placed in the cell holder. A layer of woven wire mesh filter was constructed on each end of the cell to support the membrane, and a perforated filter disc was placed in one end of the cell to prevent leakage. The well-organized cell was then sealed for the solutions to flow through. The schematic of the column set up is shown in Figure 1. The flow rate of the feed solutions was controlled by a peristaltic pump and the solutions were pumped in a down-flow mode. The treated sample at the exit of the column was collected at pre-defined time intervals. The final concentration of Pb in the solution was determined by a spectrophotometer.

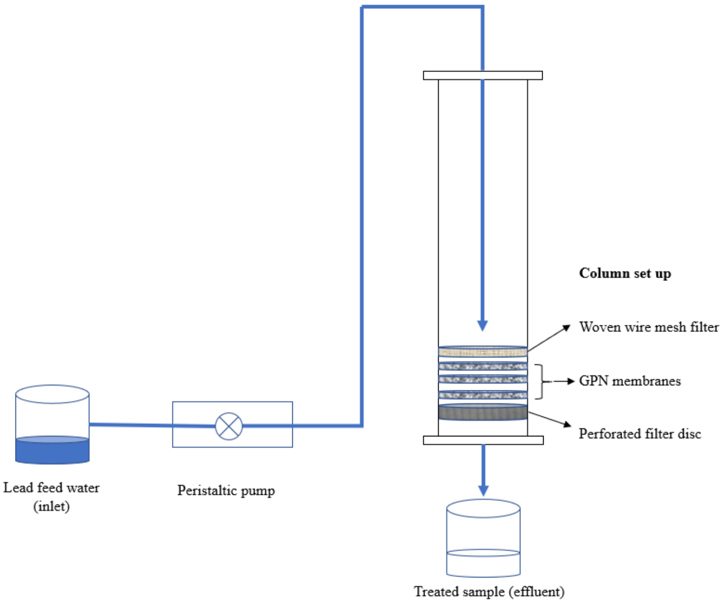

Figure 1: Dynamic adsorption experimental setup for Pb removal

Effect of feed concentration, flow rate, and bed height

To investigate the continuous Pb adsorption on GPN membranes under various conditions, experiments were performed at different initial feed concentrations (100, 200, and 300 ppm), different flow rates (10, 15 and 20 ml/min), and different bed heights (0.02, 0.04, and 0.06 cm). In each experiment, one layer of the membrane was used except in the study of the effect of bed height where multiple layers were used. The initial Pb feed solutions were prepared in deionized water. The pH of the initial feed solutions was adjusted to pH 5.0 ± 0.2 to prevent the formation of lead precipitates. The effluent was collected after a pre-determined time and measured for the residual Pb. The amount of lead (Pb) adsorbed on the membrane (q, mg/g) was calculated based on Equation 1 below (Van Elteren et al., 2013):

$$q = \frac{\int_0^t (C_0 - C_t) Q \, dt}{X} \qquad (1)$$

where C_0 (mg/L) is the initial concentration, C_t (mg/L) is the effluent concentration at time t (min), Q (mL/min) is the flow rate, and X (mg) is the mass of membranes. $C_t/C_0 = 0.2$ was defined as the breakthrough point and $C_t/C_0 = 0.9$ as the saturation point, while q_b (mg/g) and q_s (mg/g) refer to the adsorption capacity at breakthrough and saturation points, respectively. Bed utilization efficiency (Ɛ, %) is defined as the ratio of q_b to q_s, where a higher value of bed utilization efficiency signifies a better dynamic adsorption performance.

$$\mathcal{E}\% = \frac{q_b}{q_s} \tag{2}$$

Results and Discussion

Effect of feed concentration

Basically, changes in feed concentration affects the shape of the breakthrough curves (Tsai et al., 2016). In this study, different Pb feed concentrations (100, 200 and 300 ppm) were investigated at a constant flow rate of 10 ml/min and 0.02 cm bed height. The breakthrough in columns with high feed concentrations was reached much earlier (50 min for 300 ppm and 80 min for 200 ppm) compared to the low feed concentration (100 min for 100 ppm), as shown in Figure 2. In terms of the adsorption capacity, at the breakthrough point, the Pb adsorption capacity for 100, 200 and 300 ppm were 7215, 12152 and 7408 mg/g, respectively while at the saturation point the Pb adsorption capacity was 967, 4348 and 1252 mg/g, respectively. The adsorption capacity at 200 ppm is slightly higher due to the lower concentration difference between initial and final concentration. However, the dynamic adsorption performance was better for lower concentration feed solution where the bed utilization efficiency for 100, 200 and 300 ppm were 74, 27 and 59 %, respectively.

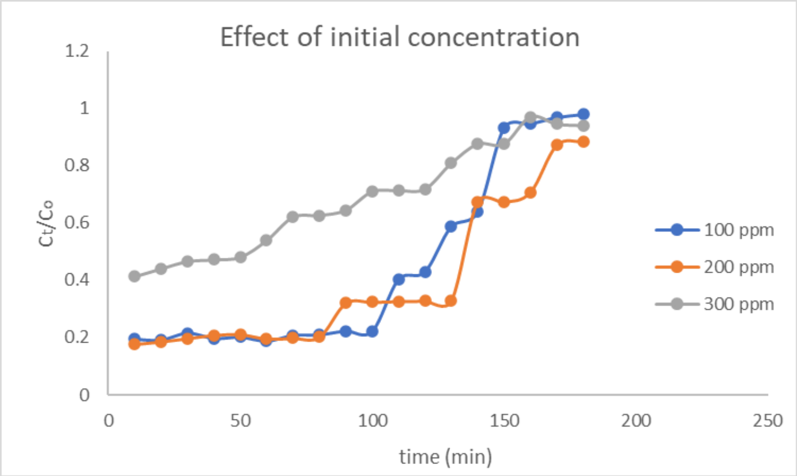

Figure 2: Effect of initial feed concentration on breakthrough curves: C_t/C_0 vs time

Effect of flow rate

The effect of flow rate on the breakthrough curve of Pb adsorption by GPN membrane is shown in Figure 3. The slopes of the curves became steeper when the flow rate increased from 10 to 20 mL/min. This result revealed that at a higher flow rate, the time required to reach the breakthrough and saturation point is decreased. This phenomenon occurred due to the residence time of Pb solution in the column or on the GPN membrane was reduced, leading to an earlier breakthrough time when the flow rate increased (Zhang et al. 2019). The Pb adsorption capacity on GPN membranes is inversely proportional to the flow rate. The values of adsorption capacity decreased from 7215 to 476 mg/g and from 1047 to 590 mg/g at the breakthrough point and saturation point, respectively. In terms of bed utilization efficiency, the results showed 68, 64 and 8% for flow rates 10, 15 and 20 ml/min, correspondingly. Therefore, a lower flow rate and longer contact time were optimal for Pb removal due to higher adsorption capacity and higher bed utilization efficiency.

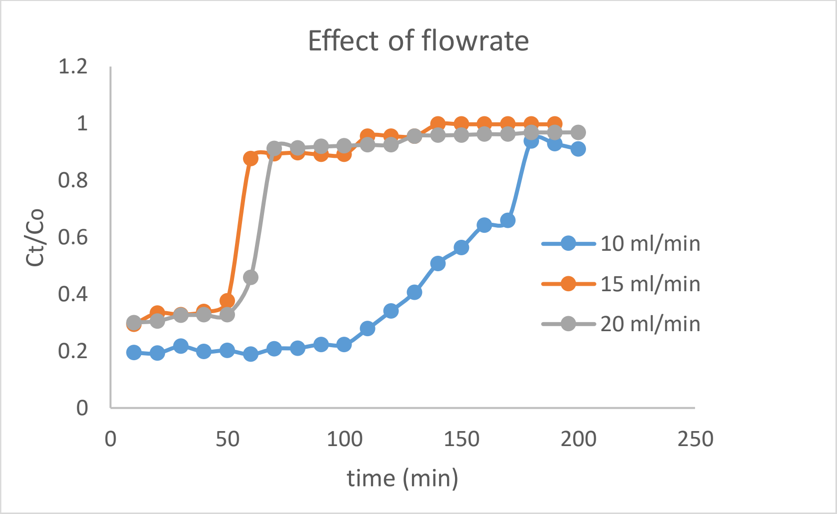

Figure 3: Effect of the flow rate of Pb adsorption on breakthrough curves: C_t/C_0 vs time

Effect of bed height

The effect of bed height on breakthrough curves was studied at a constant flow rate of 10 ml/min and a constant initial feed concentration of 200 ppm and the result is illustrated in Figure 4. The breakthrough curves shifted to the right and prolonged the breakthrough point at high bed height. Experimentally, 1, 2 and 3 layers of GPN membranes were positioned in the fixed-bed column equivalent to a bed height of 0.02, 0.04 and 0.06 cm, respectively. The adsorption capacity at the breakthrough point was elevated from 227 to 8617 mg/g when the bed height is increased as well as the adsorption capacity at the saturation point. This result describes that the more available active sites for adsorption at the higher bed height due to an increase in the membrane active area (Ji et al., 2013). The summary of the adsorption capacity at the breakthrough and saturation point as well as bed utilization efficiency were presented in Table 1.

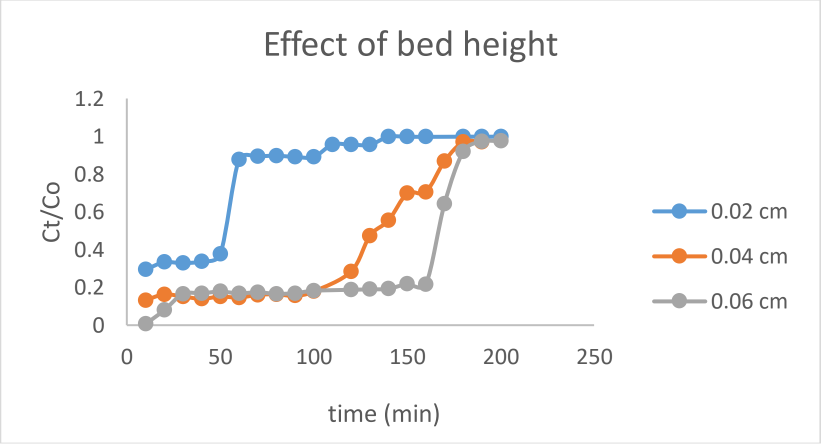

Figure 4: Effect of bed height of Pb adsorption on breakthrough curves: C_t/C_0 vs time

Table 1: Adsorption capacity and bed utilization efficiency for each effect of parameters

Feed concentration	**100ppm**	**200 ppm**	**300 ppm**
q_b (mg/g)	7215.238	12152.38	7408.571
q_s (mg/g)	967.5714	4348.571	1252.571
$\mathcal{E}$ (%)	74.5	27.9	59.1
Flow rate	**10 ml/min**	**15 ml/min**	**20 ml/min**
q_b (mg/g)	7215.238	5941.905	476.1905
q_s (mg/g)	1047.429	927.1429	590
$\mathcal{E}$ (%)	68.8	64	8
Bed height	**0.02 cm**	**0.04 cm**	**0.06 cm**
q_b (mg/g)	227.619	5909.143	8617.143
q_s (mg/g)	74.66667	1056	1024.19
$\mathcal{E}$ (%)	30.4	55.9	84.1

Modelling of breakthrough curves

The experimental continuous adsorption data were modelled to provide mathematical and quantitative approaches in designing a column adsorption process successfully. In this work, three models, namely the Thomas model, the Bohart-Adams model and the Yoon-Nelson model, have been used to predict the breakthrough curves of Pb adsorption onto the GPN membranes. These three models were commonly utilized in the determination of breakthrough curves for the adsorption of organic compounds and inorganic ions in a fixed-bed column (Bhaumik et al., 2013; Perendija et al., 2020; Zhang et al., 2019). The Thomas model is mainly assuming the Langmuir isotherm and follows second-order reversible reaction kinetics, where it is specifically suitable to estimate the adsorption process in which external and internal diffusion is not the rate-limiting step (Kumar et al., 2016; Thomas, 1944). The Bohart-Adams model assumes the non-instantaneous equilibrium and therefore, the adsorption rate is directly proportional to the adsorbate concentration and the adsorbent residual capacity (Bohart & Adams, 1920; Vijayalakshmi & Sudha, 2018). The Yoon-Nelson model is a simple theoretical model where it is assumed that the probability of adsorbate molecule is related to the adsorbate breakthrough and its adsorption process (Kutty et al., 2019; Yoon & Nelson, 1984).

The non-linear fittings of the experimental data were performed in Microsoft Excel solver (Microsoft 365). The breakthrough curves for all three parametric effects are shown in Figure 5 (a-c). The parameters and values of all three models were tabulated in Table 1. The fitting curves for optimal parameters of 100 ppm of feed concentration, 10 ml/min of flow rate and 0.06 cm of bed height are shown in Figures 5, 6 and 7 while the model equations and parameters are listed in Table 1. Notably that the fittings of Thomas and Yoon-nelson models are overlapped with each other due to the same mathematical equation form of these two models in spite of different model parameters. A good fit of the experimental data to the breakthrough models is demonstrated by the high coefficient of determination (R^2) and low sum of squared errors (*SSE*). In this present study, the R^2 of the Bohart-Adams model was higher than other two models and the *SSE* of C_t/C_0 of the Bohart-Adams model was much lower than those of the Thomas and Yoon-Nelson models. Therefore, this Bohart Adams model was found to be well-fitted in predicting the dynamic adsorption of Pb on GPN membrane indicating that the adsorption rate is proportional to the residual capacity of the adsorbent and the concentration of the adsorbate. Then, the experiments were done on the optimum parameters condition of 100 ppm of initial Pb feed concentration, 10 ml/min of flow rate and 0.06 cm of bed height with maximum adsorption capacity of 1614 mg/g.

a) b)

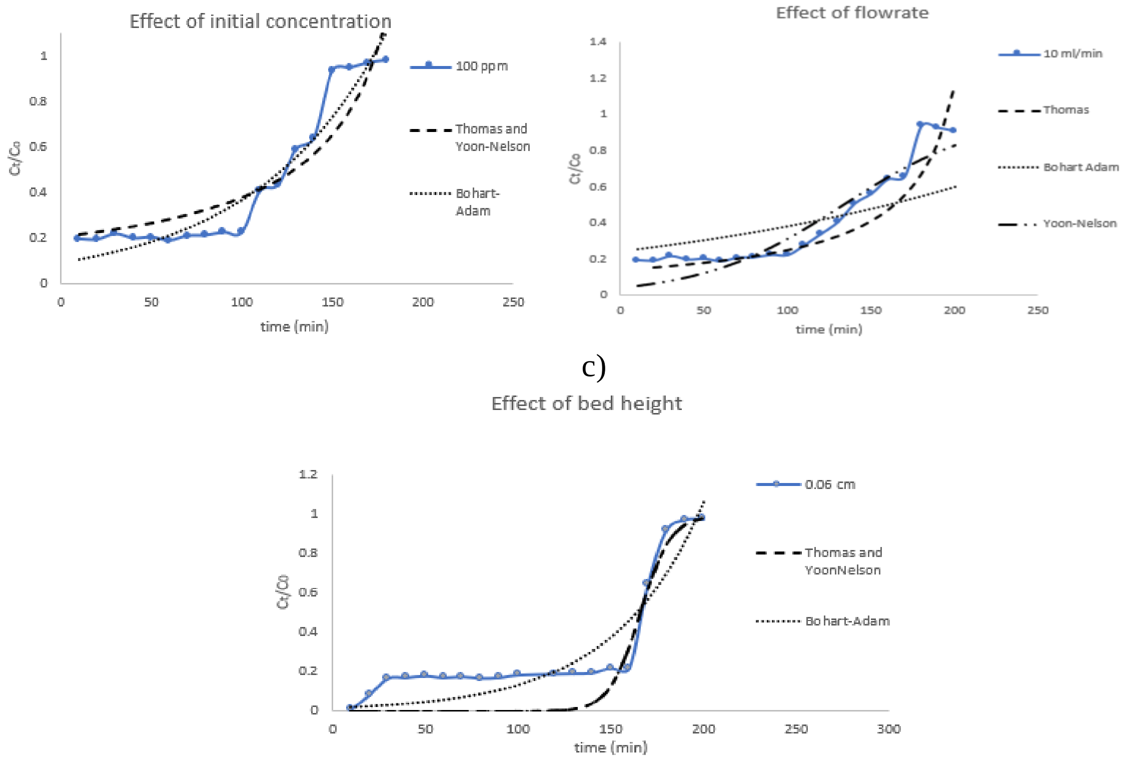

Figure 5: Non-linear fittings of breakthrough curves using the Thomas, Yoon-Nelson and Bohart-Adams models

Table 2: Breakthrough models and model parameters based on non-linear regressions for Pb adsorption on GPN membranes

Model	**Model formula**	**Linearized expression**	**Parameter**	**Effect of initial concentration**	**Effect of bed height**	**Effect of flow rate**
Thomas[a]	$\frac{C_t}{C_o} = \frac{1}{1 + e^{\frac{k_T q_0 X}{Q} - k_T C_o t}}$	$ln\left(\frac{C_0}{C_t} - 1\right) = \frac{k_T q_0 X}{Q} - k_T C_0 t$	Theoretical q_0 *(mg/g)*	5790.2	31571.2	5500
			k_T *(mL/min.mg)*	2.23 x 10^{-4}	6.09 x 10^{-4}	3.14 x 10^{-4}
			R^2	0.9515	0.9832	0.9319
			SSE	0.2373	0.3458	0.2778
Bohart-Adams[b]	$\frac{C_t}{C_o} = e^{k_{BA} C_0 t - \frac{k_{BA} N_0 Z}{u}}$	$\ln\left(\frac{C_0}{C_t}\right) = k_{BA} C_0 t - \frac{k_{BA} N_0 Z}{u}$	N_o *(mg/L)*	60250	143327	10.9 x 10^4
			k_{BA} *(L/mg.min)*	1.4 x10^{-4}	1.0 x 10^{-4}	4.54 x 10^{-5}
			R^2	0.9987	0.9997	0.9867
			SSE	0.1292	0.2873	0.5714
Yoon-Nelson[c]	$\frac{C_t}{C_0} = \frac{1}{1 + e^{k_{YN}(\tau - t)}}$	$\ln\left(\frac{C_0}{C_t} - 1\right) = k_{YN}\tau - k_{YN} t$	k_{YN} *(min^{-1})*	0.05	0.1218	0.0237
			τ *(min)*	70	165	133.08
			R^2	0.9515	0.9832	0.9645
			SSE	0.2373	0.3458	0.1678

Note: [a]k_T (mL/(min mg)), Thomas rate constant, and q_0 (mg/g), predicted adsorption capacity; [b]K_{BA} (L/(mg min)), Bohart-Adams kinetics constant, N_0 (mg/L), maximum volumetric adsorption capacity, μ (cm/min), linear velocity of the fluid, and *Z* (cm), bed height; [c]k_{YN} (min^{-1}), Yoon and Nelson's rate constant, and τ (min), time required for 50% breakthrough

Conclusion

In conclusion, The GPN membrane demonstrated good comparative properties to the commercial membrane in terms of adsorption capacity and removal efficiency. It is therefore believed that embedment of GO and PVP to modify the polyethersulfone membrane is an excellent approach to develop high performance membrane and enhance selectivity, and stability of the membrane. The utilization of the GPN membrane in the wastewater treatment can be assessed in further studies of filtration behaviour towards the removal of other contaminants. The development of the GPN membrane would be the best alternative to revolutionize wastewater treatment and beneficial for making this technology accessible to Malaysia.

References

Bhaumik, M., Setshedi, K., Maity, A., & Onyango, M. S. (2013). Removal from water using fixed bed column of polypyrrole/Fe 3O4 nanocomposite. *Separation and Purification Technology*, *110*, 11–19. https://doi.org/10.1016/j.seppur.2013.02.037

Bohart, G. S., & Adams, E. Q. (1920). Some aspects of the behavior of charcoal with respect to chlorine. *Journal of the Franklin Institute*, *189*(5), 669. https://doi.org/10.1016/s0016-0032(20)90400-3

Ji, F., Li, C., Xu, J., & Liu, P. (2013). Colloids and Surfaces A : Physicochemical and Engineering Aspects Dynamic adsorption of Cu (II) from aqueous solution by zeolite / cellulose acetate blend fiber in fixed-bed. *Colloids and Surfaces A: Physicochemical and Engineering Aspects*, *434*, 88–94. https://doi.org/10.1016/j.colsurfa.2013.05.045

Krause, A., Zimmermann, K. F., & Chowdhury, S. (2015). *2014_meyer_estrin_GSJ-subsidiary-strategy.pdf*. *9400*.

Kumar, D., Pandey, L. K., & Gaur, J. P. (2016). Metal sorption by algal biomass: From batch to continuous system. *Algal Research*, *18*, 95–109. https://doi.org/10.1016/j.algal.2016.05.026

Kutty, S. R. M., Almahbashi, N. M. Y., Nazrin, A. A. M., Malek, M. A., Noor, A., Baloo, L., & Ghaleb, A. A. S. (2019). Heliyon Adsorption kinetics of colour removal from palm oil mill ef fl uent using wastewater sludge carbon in column studies. *Heliyon*, *5*(August), e02439. https://doi.org/10.1016/j.heliyon.2019.e02439

Manirethan, V., Gupta, N., Balakrishnan, R. M., & Raval, K. (2019). Batch and continuous studies on the removal of heavy metals from aqueous solution using biosynthesised melanin-coated PVDF membranes. *Environmental Science and Pollution Research*, *27*(20), 24723–24737. https://doi.org/10.1007/s11356-019-06310-8

Mkhoyan, K. A., Contryman, A. W., Silcox, J., Derek, A., Eda, G., Mattevi, C., Miller, S., Chhowalla, M., Mkhoyan, K. A., Contryman, A. W., Silcox, J., Stewart, D. A., Eda, G., Mattevi, C., & Miller, S. (2009). *Atomic and Electronic Structure of Graphene-Oxide*. https://doi.org/10.1021/nl8034256

Naushad, M. (2018). A new generation material graphene: Applications in water technology. In *A New Generation Material Graphene: Applications in Water Technology*. Springer International Publishing. https://doi.org/10.1007/978-3-319-75484-0

Peng, W., Li, H., Liu, Y., & Song, S. (2017). A review on heavy metal ions adsorption from water by graphene oxide and its composites. *Journal of Molecular Liquids*, *230*, 496–504. https://doi.org/10.1016/j.molliq.2017.01.064

Perendija, J., Veličković, Z. S., Cvijetić, I., Rusmirović, J. D., Ugrinović, V., Marinković, A. D., & Onjia, A. (2020). Batch and column adsorption of cations, oxyanions and dyes on a magnetite modified cellulose-based membrane. *Cellulose*, *27*(14), 8215–8235. https://doi.org/10.1007/s10570-020-03352-x

Thomas, H. C. (1944). Heterogeneous Ion Exchange in a Flowing System. *Journal of the American Chemical Society*, *66*(10), 1664–1666. https://doi.org/10.1021/ja01238a017

Tsai, W., Luna, M. D. G. De, Bermillo-arriesgado, H. L. P., Futalan, C. M., Colades, J. I., & Wan, M. (2016). *Competitive Fixed-Bed Adsorption of Pb (II), Cu (II), and Ni (II) from Aqueous Solution Using Chitosan-Coated Bentonite*. *2016*(Ii).

Van Elteren, J. T., Grilc, M., Beeston, M. P., Reig, M. S., & Grgić, I. (2013). An integrated experimental-modeling approach to study the acid leaching behavior of lead from sub-micrometer lead silicate glass particles. *Journal of Hazardous Materials*, *262*, 240–249. https://doi.org/10.1016/j.jhazmat.2013.08.052

Vijayalakshmi, K., & Sudha, P. N. (2018). *MODELING FIXED BED COLUMN FOR LEAD (II) REMOVAL FROM AQUEOUS SOLUTION USING NANOCHITOSAN / SODIUM ALGINATE / MICROCRYSTALLINE CELLULOSE BEADS*. *7*(8), 340–362. https://doi.org/10.20959/wjpr20188-11022

Wang, X., Feng, M., Liu, Y., Deng, H., & Lu, J. (2019). Fabrication of graphene oxide blended polyethersulfone membranes via phase inversion assisted by electric field for improved separation and antifouling performance. *Journal of Membrane Science*, *577*, 41–50. https://doi.org/10.1016/j.memsci.2019.01.055

Yoon, Y. H., & Nelson, J. H. (1984). Application of Gas Adsorption Kinetics I. A Theoretical Model for Respirator Cartridge Service Life. *American Industrial Hygiene Association Journal*, *45*(8), 509–516. https://doi.org/10.1080/15298668491400197

Zhang, S., Shi, Q., Christodoulatos, C., Korfiatis, G., & Meng, X. (2019). Adsorptive filtration of lead by electrospun PVA/PAA nanofiber membranes in a fixed-bed column. *Chemical Engineering Journal*, *370*, 1262–1273. https://doi.org/10.1016/j.cej.2019.03.294

International Research Conference on Applied Sciences and Engineering 2020 (IRCASE 2020)
eISBN 978-967-2426-20-2
13th – 14th December 2020

EFFECT OF FIBRE DIRECTION ON REPAIRING TENSILE FAILURE OF GLASS FIBRE/POLYESTER COMPOSITE

Verawaty Ismail[1]
Mohd Hilmi Ariffin[2]
Mohammad Syahadan Maksom[3]

[1] Department of Mechanical Engineering, Polytechnic Mukah, Malaysia, (E-mail: verawaty@pmu.edu.my)
[2] Department of Mechanical Engineering, Polytechnic Mukah, Malaysia, (E-mail: hilmi@pmu.edu.my)
[3] Department of Mechanical Engineering, Polytechnic Mukah, Malaysia, (E-mail: syahadan@pmu.edu.my)

Abstract: *Orientations of the fibres play important roles to improve the strength and stiffness of a composite. This study is focused on the effect of fibre directions of a composite at 0°, 90° and 45° on repairing tensile failure of glass fibre/polyester composite. This experiment, carried out to investigate said effects using on fabricated unidirectional glass fibre that drawn from a woven glass fibre with polyester resin used as the binding materials. Unidirectional test specimens had been successfully fabricated, fractured and then repaired with varying fibre directions. Tensile tests on the repaired composite specimen were prepared according to the ASTM D3039/D3039M. The repairs with 0°, 45° and 90° fibre direction provided the highest tensile strength at 119.234 MPa, 53.270 MPa and 31.943 MPa respectively. The average Young Modulus results on all three series of specimens mended with 0°, 90° and 45° fibre directions are at 10217.505 MPa, 7239.747 MPa and 12103.192 MPa respectively. Physical compositions for the fabricated specimens were determined with burnout test. The fibre weight and volume ratio of 0° and 90° fibre directions show some consistency at 0.47 and 0.344 respectively. The fibre weight and volume of the 45° fibre direction is the highest at 0.506 and 0.354 due to its fibre repair directions.*

Keywords: *fibreglass, repaired fibreglass, fibre direction, tensile test, burnout test*

Introduction

A composite is when two or more natural or artificial materials are combined together to create a superior and unique material and having a recognizable interface between them. Most composites consist of fibres of one material tightly bound into another material called a matrix. The matrix binds the fibres together somewhat like an adhesive and makes them more resistant to external damage, whereas the fibres make the matrix stronger and stiffer and help resist cracks and fractures. Composites are seen as a practical application nowadays as an alternative to metallic materials due to its lightweight and superior properties, mainly utilized in aerospace structures, high-speed boats and trains where weight is major considerations for the applications.

Glass fibre/Polyester composite is a composite material consists of glass fibre as reinforcement and polyester as binding matrix material. Fibreglass offers high tensile strength, heat and fire resistance, durable and many other properties as reinforcement of composite, but most importantly, glass fibre offers high strength to weight ratio for many applications. As for polyester resins, regardless of its lower performance to that of epoxy resins is easier to handle and cost lower than epoxies making it widely used for most marine structures. The mechanical properties of fibreglass composite mainly depend on the volume ratio of the fibre and matrix along with the individual properties of the fibre and composite themselves.

Fibre directions or orientations of a composite may refers to 0°, in which forces are applied in the same direction of the fibres, 90° for when the fibre direction is perpendicular to applied force and the 45° when the fibre direction is at 45° diagonally to the applied force. The orientations of the fibres apparently plays important roles to improve the strength and stiffness of a composite. To date, many research had been performed to investigate the effect of fibre orientations in the mechanical properties of composite materials and proven to have major roles in increasing some properties of the materials. Bakir and Hashem [1] reported that the tensile strength is the highest in specimen with 0° fibre orientation and lowest in the specimen with 90° fibre direction. H.W Wang et.al [2] analytical results indicate highest Young's Modulus of the 0° fibre orientation and lowest at about 45° fibre direction.

However, there was limited studies done on the effect of fibre directions on repairing tensile failure of fibreglass composite. Tensile failure in unidirectional reinforced fibreglass composite occurs when tensile loading is subjected parallel to the fibre direction; usually indicate how a material react to forces being applied in tension. Because of the nature of the fibreglass composite, usually tensile failure can be repaired by mechanically cleaning and patching the affected area. This experiment aims to investigate said effects using a unidirectional glass fibre that drawn from a woven glass fibre with polyester resin used as the binding materials. A series of specimens are prepared and fractured intentionally to allow for repairing process. Initial calculation of weight ratio of the fibre:resin used to fabricate the specimen is 50:50 and will be later confirmed after burnt out procedures.

Experimental

Materials

Continuous glass fibre drawn from woven E-glass fibre fabric was used as the reinforcing material. Polyester was opted as the matrix material with corresponding hardener as it was easier to handle, cost lower and the most common resin for fibreglass boats construction compared to epoxy resin.

Preparation of Test Specimens

A series of unidirectional, continuous fibreglass-reinforced polyester test specimens as in Figure 1A manually using hand lay-up process and cured overnight at room temperature. Test specimens were prepared according to ASTM D3039/D3039M-14 [9] for unidirectional fibre composite testing. Initial test specimens had a length of 250 mm, 15 mm width and a thickness of 1 mm for 0° with tabs from the same material of 1.5 mm thickness were fixed to both end of the specimens (Figure 1B) to prevent gripping damage on specimens during tensile test. The weight fibre-weight fractions in composite were pre-determined at 50% and the fibre was not conditioned before fabricating the composite.

Figure 1: (A) Fabricated Unidirectional Specimen, (B) Specimens with Tabs

The specimens in Figure 1 were prepared for preliminary testing until failure. After tensile failure the specimens will be repaired to serve the purpose of the study. Preliminary tensile tests on the samples were carried out to find out the initial tensile strength and the pattern of the tensile fracture of the fabricated samples. Test result showed that original sample can withstand up to 10 kN of applied force, making its tensile strength at about 701 MPa before breaking. However, from preliminary tensile test, it turned out the reinforcing fibres are being pulled from end to end (refer Figure 2A*)* making the sample coupons were in total damage and impossible to repair.

Figure 2: (A) Fractured Test Specimen from Preliminary Tensile Test, (B) Fractured Test Specimen After an Incision Was Introduced.

To prevent total damage, a notch was introduced right in the middle of test strips as the initiation point of fracture. A small notch or incision using cutter was initiated on each sample before pulling the sample to ensure uniform fracture along in the middle of the initial sample as shown in Figure 2B. Fractured samples were then repaired using same fibre glass and matrix with different fibre directions. Repairing was done by modifying the repairing method proposed by Zimmerman et.al. in US Patent No.5,601,676 [3] for Composite Joining and Repair referring to Figure 3.

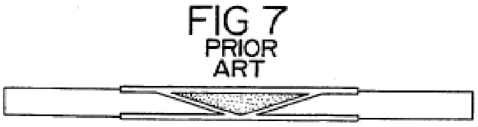

Figure 3: Repairing Composite Method

(Source: US Patent, No. 5,601, 676)

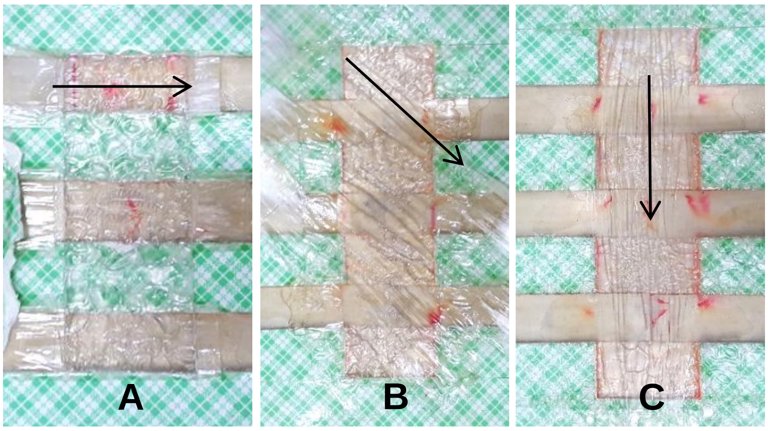

Figure 4: Repairing Specimens at (A) 0°, (B) 45° and (C) 90° Fibre Directions.

The fractured samples were mechanically prepared by abrading the affected area at a radius about 12 times the thickness of the samples. The abraded area was then cleaned using acetone to ensure the area to be repaired was contaminant free. Then, fibreglass patches in three layers applied to the prepared area according to desired fibre directions. The repaired specimen was then pressed with steel and brick weight to squeeze excess resins away from repaired area and to initiate uniform pressure at the patch interface. The specimens were removed once they were fully cured in room temperature. The test specimens were lightly sanded and cleaned to restore them to their original appearance before being put to tests. Test strips were repaired using fibre orientation of 0°, 45° and 90° to investigate the effects of fibre directions on the repaired fibreglass composite as shown in Figure 5.

Characterization

Tensile tests on the repaired composite specimen were conducted according to the ASTM D3039/D3039M–14 Standard Test Method for Tensile Properties of Polymer Matrix Composite Materials. The testing was performed on Shimadzu Universal Testing Machine AG-20KNX with test speed of 1 mm/min.

Figure 5: Tensile Test on Universal Testing Machine

To calculate the tensile strength, the following equation is used:

$$\sigma = P_{max}/A \qquad (1)$$

Where; σ = tensile strength, MPa
P_{max} = maximum load prior to failure, N
A = average cross-sectional area, m^2

The fibre volume ratio plays an important role to achieve appropriate structural performance for a composite material. Engineering designer often uses the fibre volume ratio to derive lamina properties and structural properties. The best way to confirm the fibre weight ratio is with a burnout test. The tests were carried out by placing specimens in ceramic crucible in electric furnace at about 700°C - 900°C as in Figure 6. After the resin was burnt out, the sample was cooled and weighted. By comparing sample weights before and after the burn, the fibre weight ratio can be calculated.

Figure 6: (A) Specimen Sample in Ceramic Cubicle placed in the Crucible Furnace, (B) Remains of Fibre after Burnout Test

The resin weight is the difference between the composite and fibre weights:

$$W_{resin} = W_{composite} - W_{fibre} \quad (2)$$

The vendor data on the density of both the fibre and the resins have to be acquired to calculate the fibre volume ratio. The fibre/resin volume ratio is calculated using;

$$\frac{V_{fibre}}{V_{resin}} = \left(\frac{W_{fibre}}{W_{resin}}\right)\left(\frac{\rho_{resin}}{\rho_{fibre}}\right) \quad (3)$$

Therefore, the matrix volume ratio is given by;

$$V_m = \frac{1}{1+\left(\frac{V_{fibre}}{V_{resin}}\right)} \quad (4)$$

Finally, the fibre volume ratio is given by;

$$V_f = 1 - V_m - V_{voids} \quad (5)$$

Results and Discussion

Repaired Specimens Tensile Strength

Test specimens were tested as per standard in ASTM D3039/D3039M to evaluate their tensile strength. The results of tests on all three series of specimens mended with 0°, 90° and 45° fibre direction was tabulated in Table 1.

Table 1: Results of Tensile Test on Unidirectional Repaired Specimens with 0°, 45° and 90° Fibre Directions

Sample	Max. Force (N)	Tensile Strength (MPa)	Young's Modulus (MPa)
0°	1788.51	119.234	10217.505
90°	479.15	31.943	7239.747
45°	799.04	53.270	12103.192

Observations of tensile properties for unidirectional specimens repaired with 0° fibre direction show that the specimen can withstand up to 1788.51 N applied force. The specimens repaired with 90° fibre direction only been able to hold up to 479.15 N, while the 45° patched batch of specimens can stand a maximum load of 799.04 N. The unidirectional specimens mended with 0° fibre direction also has the highest tensile strength of 119.234 MPa average amongst all fibre directions used in this research. Lowest tensile strength was exhibited by specimens using 90° fibre orientations at 31.943 MPa, while the 45° fibre direction has a tensile strength of 53.72 MPa average.

Overall, the tensile strengths of specimens repaired with varied fibre direction can be compared in **Figure 7** with 0° fibre direction repairs exhibit tensile strength doubled the strength of the specimens with 90° and 45° fibre direction.

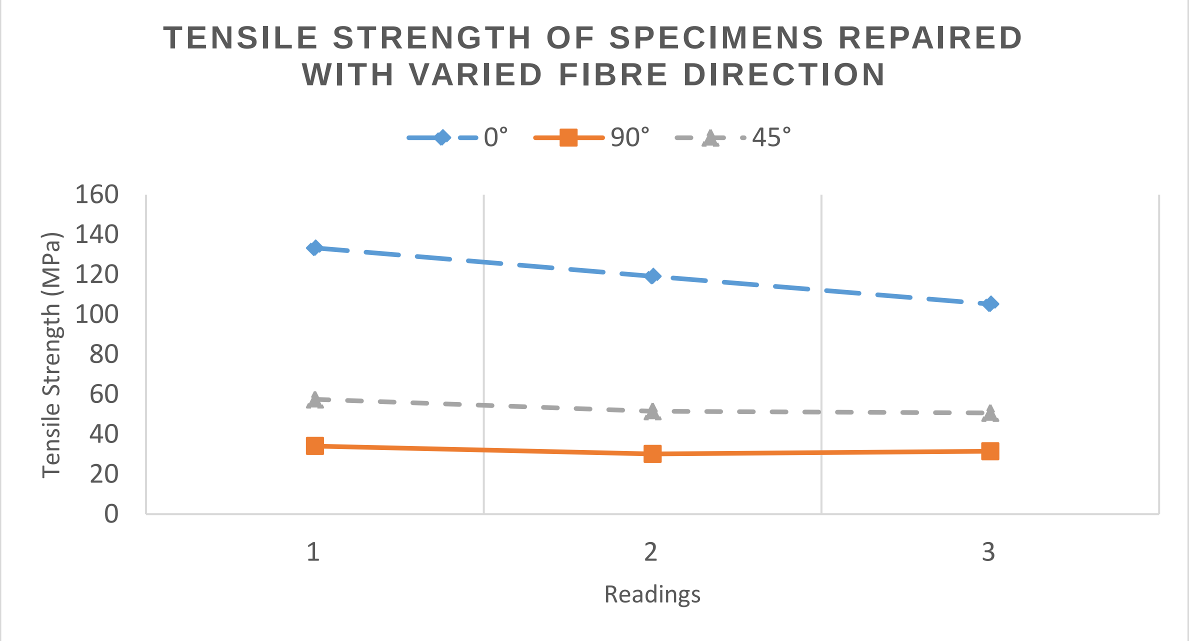

Figure 7: Tensile Test Results of Specimens Repaired with Varied Fibre Direction

The results basically the same of the tensile strength exhibited in precious works on the fibre directions effect on the composites. The 0° unidirectional repairs proven to be most effective in the repairing tensile fracture in this study. This is due to the direction of fibre repairs and the formerly fabricated specimens is the same providing the grips between previous and newly repaired fibres in the specimens. This fact clearly suggested that repairing tensile fracture in the same direction of the former specimens and applied load is preferable to maintain as much tensile properties as possible in repairing fibre process.

However, the tensile strength of the composite had greatly reduced greatly by about 83% from the former 0° unidirectional specimen. This is most probably due to: (1) the uneven fibre alignment between the repaired and prior fibre; (2) discontinuation of the fibre along the specimen, (3) strength of the adhesive bonds or; (4) ineffective repairing technique being carried out in this study. The techniques provided by Zimmerman et. al. [3] are actually 3-dimensional bonding with interlocking fractured pieces in U, V, W and S-shaped configuration at the fracture area for composite panel with a minimum of 3 mm thickness and much wider panels. But, in this study the techniques were unable to be fully adopted due to lack of thickness and width of the specimens, making the repairs only able to be performed on the top of the fracture line instead of both top and bottom side of the specimen.

The stress-strain curves of the tensile tests are also able to exhibit the ability of the material to resist deformations under load, also known as the Young's Modulus. The greater in the modulus of elasticity, the stiffer the material, or the smaller the elastic strain that results from the application of a given stress (Callister W.D, 2000) [8]. The

Young's Modulus of the specimens generally can be presented by the stress-strain slope in **Figure 8** which shows the 45° fibre direction has the highest modulus at about 12103.192 MPa and lowest on the 90° fibre direction with 7239.747 MPa.

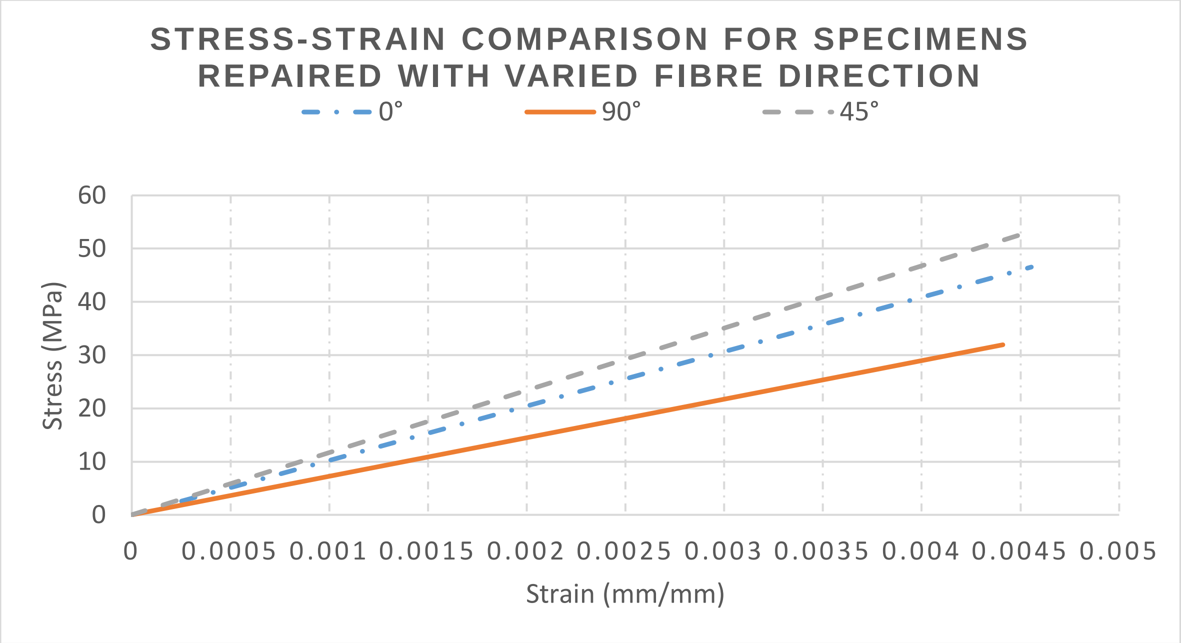

Figure 8: Stress-Strain Comparison for Specimens with Varied Fibre Direction

Based on the value of Young's Modulus from the experiment, it can be inferred as the 45° fibre direction repaired specimens were the stiffest and only elongate slightly before break, while the 90° fibre direction showed the lowest stiffness. This result can be confirmed visually from the fracture pattern in **Figure 9A** and **9C**. This however contrasting to a study by Wang et. al. [2], Young's Modulus of the 45° specimens is the lowest and the highest on the 0° fibre direction specimens, analytically and experimentally. From this experiment, the value of the Young's Modulus of 0° fibre direction repairs still fairly high as suggested. The fracture pattern in **Figure 9B** shows small elastic strain from the repaired part of the specimens and most of repairing fibre pulled out from the specimen. As in the 45° fibre direction repairs may be able to exhibit higher Young's Modulus due to the change in fibre direction in the repair area. The change of direction provides grasps from prior specimen (at 0° unidirectional) and repaired fibre and making its stiffer and unable to elongate well in the direction of applied tensile load. Specimen in **Figure 9C** shows not only a part of the repairing fibre pulled out from the specimen, it also manages to fracture a portion of the prior specimen body due to the grasp from repairing fibre.

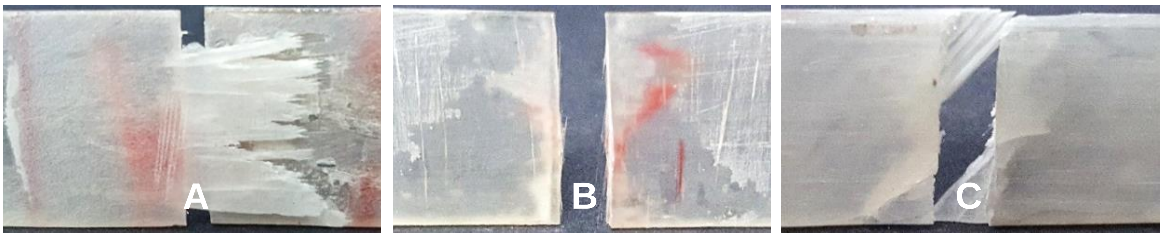

Figure 9: Fracture Patterns of the (A)0°, (B)90° and (C) 45° Repair Fibre Directions.

Composite Fibre Volume Ratio

Burnout test was carried out to investigate a critical property of the fabricated fibreglass-polyester composite specimens in this experiment, which is the fibre volume ratio. Burnout test was performed by sampling a specimen from each series of the fibre directions.

Table 2: Fibre Weight and Volume Ratio of Specimens for 0°, 90°, 45° Fibre Repair Directions

Sample	Fibre Weight Ratio	Fibre Volume Ratio
0°	0.472	0.344
90°	0.473	0.344
45°	0.506	0.354

Although initially, the calculation of fibre weight usage is aimed for 50:50 ratio of fibre to resin, the final weight ratios are as indicated in **Table 2**. There was slight shortage in fibre weight probably because of more resin added during repair procedure. Overall, the fibre weight and volume ratio of 0° and 90° fibre directions show some consistency at 0.47 and 0.34 respectively. The fibre weight and volume of the 45° fibre direction is the highest at 0.506 and 0.354 due to its fibre repair directions. More fibre is added to cover up the repair area diagonally.

Conclusion

The experimental on tensile strength for three different fibre direction on repairing tensile failure of fibre glass/polyester composite have been carried out to investigate the effect of the fibre directions on the repaired composite. Unidirectional test specimens had been successfully fabricated, fractured and then repaired with varying fibre directions of 0°, 90° and 45°. It can be concluded that from the test results, the 0° fibre direction provided the highest tensile strength and most ideal fibre direction for repairing tensile fracture of former 0° unidirectional specimens. The 0° test specimens also have fairly high Young's Modulus which suggests this direction of repaired fibre makes the repaired specimen stiff and inferred that there are still grasps between the prior and repairing fibre. This study is performed on fibre weight and volume ratio of average 0.483 and 0.347 respectively.

References

[1] Bakir, B., & Hashem, H. (2013). Effect of fibre orientation for fibre glass reinforced composite material on mechanical properties. *International Journal of Mining, Metallurgy and Mechanical Engineering (IJJMME)*, 1(5), 341-345.

[2] Wang, H. W., Zhou, H. W., Gui, L. L., Ji, H. W., & Zhang, X. C. (2014). Analysis of effect of fibre orientation on Young's modulus for unidirectional fibre reinforced composites. *Composites Part B: Engineering*, 56, 733-739.

[3] Zimmerman, K. B., & Liu, D. (1997). U.S. Patent No. 5,601,676. Washington, DC: U.S. Patent and Trademark Office.

[4] Brahim, S. B., & Cheikh, R. B. (2007). Influence of fibre orientation and volume fraction on the tensile properties of unidirectional Alfa-polyester composite. *Composites Science and Technology*, 67(1), 140-147.

[5] Shih, G. C., & Ebert, L. J. (1987). The effect of the fibre/matrix interface on the flexural fatigue performance of unidirectional fibreglass composites. *Composites Science and Technology*, 28(2), 137-161.

[6] Thomason, J. L., & Vlug, M. A. (1996). Influence of fibre length and concentration on the properties of glass fibre-reinforced polypropylene: Tensile and flexural modulus. *Composites Part A: Applied science and manufacturing*, 27(6), 477-484.

[7] Almeida, J. H., Angrizani, C. C., Botelho, E. C., & Amico, S. C. (2015). Effect of fibre orientation on the shear behavior of glass fibre/epoxy composites. *Materials & Design* (1980-2015), 65, 789-795.

[8] Callister, W.D. (2000). *Materials Science and Engineering: An Introduction*. John Wiley and Sons, Inc., New York.

[9] Standard, A. S. T. M. D3039/D3039M-14 (2014). *Standard Test Method for Tensile Properties of Polymer Matrix Composite Materials.* ASTM International, West Conshohocken, PA.

THE EFFECT OF MALTODEXTRIN AND ACACIA GUM ON ENCAPSULATION OF FIG POWDER PHYSICOCHEMICAL PROPERTIES

Noorsabrina M Salbi[1]
Norhayati Muhammad[2]
Norazlin Abdullah[3]

[1]Faculty of Applied Sciences and Technology, Universiti Tun Hussein Onn Malaysia (UTHM), Malaysia, (E-mail: ms.noorsabrina@gmail.com)
[2]Faculty of Applied Sciences and Technology, Universiti Tun Hussein Onn Malaysia (UTHM), Malaysia, (E-mail: norhayatim@uthm.edu.my)
[3]Faculty of Applied Sciences and Technology, Universiti Tun Hussein Onn Malaysia (UTHM), Malaysia, (E-mail: norazlinh@uthm.edu.my)

Abstract: *In this study, the effect of coating material composition on the encapsulation of physical and chemical properties of fig powder was investigated. As coating material maltodextrin and acacia gum at different ratios were chosen (100% and 75%:25%). The core to coating ratio was 1:1. The microcapsules were prepared with high-speed homogenizer at 10000 rpm for 10 min. The vacuum dried microcapsules were analyzed in terms of moisture, total soluble solid, bulk and tapped density, Carr's index, Hausher ratio, total flavonoid content, and antioxidant activity. The antioxidant activity was mostly higher when coating ratio was 100% acacia gum in the core and coating ratio of 1:1 as compared to others. There was positive correlation between total flavonoid content and antioxidant activity. Combination of coating agent in ratio 75%: 25% vice versa significantly improve the physical properties of fig powder. The ratio of maltodextrin and gum arabic had significant effect on all physical and chemical properties analyzed.*

Keywords: *Encapsulation, maltodextrin, acacia gum, fig powder*

Introduction

Fig have been known since ancient times for its phytochemical that relates to its curative properties which have been utilized for the treatment of various ailment (Muhammed & Shamsi, 2016). In general, polyphenol is a powerful antioxidant which classified in three main classes; phenolic acids, flavonoids, and stilbenoids. Flavonoid is the most natural biological response modifiers among others (Cao, Sofic, & Prior, 1997). In biological systems, oxidative damage results from an imbalance in free radicals and antioxidants. As a result, oxidative stress will lead to cell membrane disintegration, protein damage, and DNA mutation. Furthermore, it will initiate or propagate aging and several diseases, such as neurodegenerative disorders, cancer, liver cirrhosis, cardiovascular diseases, atherosclerosis, cataracts, diabetes, and inflammation. Phenolic compounds, such as phenols, phenolic acids, flavonoids, tannins, and anthocyanins, have received considerable attention for their high antioxidant activity (Mnari et al., 2016). Antioxidant activity can act in various ways, such as inhibiting free radical oxidation reactions by preventing the formation of free lipid radicals; acting as singlet oxygen quenchers; reducing agents which produce stable compounds from hydroperoxide; acting as metal chelators and acting as inhibitors of pro-oxidative enzymes (Ma & Zhang, 2017).

Encapsulation is a process in which one material is entrapped or coated with another material in order to protect the coated material against adverse conditions and the nutritional deterioration. The coated one is named as core or active material and the surrounding one is coating material (Mcnamee et al.1998). In addition to protection, by encapsulation process, controlling the release of core material and masking the undesired properties of core material can be achieved (Dubey et al. 2009). Coating materials have significant role in stability of the encapsulation process. Different kinds of coating materials are used for encapsulation process such as polysaccharides, proteins and lipids (Mcnamee et al., 1998). Maltodextrin has good solubility in water and low viscosity values even at high concentrations. These properties make maltodextrin useful for coating material. On the other hand, maltodextrins are deficient in terms of emulsification property and surface-active features. For this reason, combining other coating materials with maltodextrin is required to form stable capsules (Rosenberg and Sheu, 1995). Acacia gum is composed of branched arrangement of simple sugars like galactose, glucuronic acid, arabinose and rhamnose and small amount of covalently bonded protein. This protein gives functional properties to acacia (Mcnamee et al., 1998). It has high water solubility and low viscosity than other gum types (Madene et al. 2006). In addition, it can create a protective film around core material and acts like emulsifier. In other words, it prevents aggregation by forming a thick layer (Zuidam and Nedović, 2010).

As stated by Farhangi et al. (2014), figs can remove the kidney and urinary bladder stone, release intestinal pain, pile, dyspepsia, and anorexia. Fruit contains pentose, amino acid, tyrosine, enzyme, cravin, lipase, protease, and sugar. The most phytochemical content of figs is flavonoids which are quercetin and luteolin (Marwat et al., 2009). The investigation by Soni et al. (2014) deals with the nutritional, phytochemical, antioxidant and antibacterial activity of dried fruit of fig (Ficus carica) indicates that its polyphenols contribute to its high antioxidant activity. The rich content of flavonoids in fig contribute to anti-cancer, antioxidant, anti-inflammation, anti-acne, anti-bacterial (Mahmoudi et al., 2018). The objective of this study was to encapsulate fig juice. Moreover, the effects of coating materials with different type and ratio were investigated in terms of physical and chemical properties.

Material and Methods

Material

Figs was taken from the local market in Johor, Malaysia. Maltodextrin and acacia gum were the coating materials and purchased from VIS Foodtech Ingredient Supply Sdn. Bhd. (Kuala Lumpur, Malaysia). The reagents used in the experiments, which were aluminium chloride ($AlCl_3$), methanol (CH_3OH), potassium acetate (CH_3CO_2K), quercetin ($C_{15}H_{10}O_7$), and DPPH (2,2-diphenyl-1-picrylhydrazyl) were all bought from Merck Germany.

Encapsulation

The fig juice was prepared by laboratory juice maker (KEA0236, Alpha, China). Coating materials were prepared in 4 different compositions (100% maltodextrin, 100% acacia gum, 25% acacia gum with 75% maltodextrin and 25% maltodextrin with 75% acacia gum). In addition, the mixture of coating materials was homogenized at 6000 rpm for 2 min. Then, the 50g juice and coating material were separately weighted for encapsulation with 1:1 core to coating ratio. In order, to get capsules, the mixtures were homogenized by high-speed homogenizer (IKA T18 digital Ultra-Turrax, Selangor, Malaysia) at 1000 rpm for 10 min. Then, capsules were vacuum dried at 35°C for 24 hours.

Physical Properties

The physical properties of fig powder were evaluated by moisture content, total soluble solid (°Brix), angle of repose value, bulk density, tapped density, Hausner ratio and Carr's index. The moisture content of powder was determined by placing 5g of powder in moisture analyzer (Precisa XM 66, Switzerland). ºBrix was determined by first preparing a blend of 1 g of fig powder with 10 ml of distilled water. This blend could stand for 1hour at room temperature and stirring manually sporadically. Determination of °Brix was carried out using a hand refractometer (Atago PAL-BX/RI, Japan). The refractometer prism surface was cleaned with distilled water and tissue paper, followed by placing a drop of the sample on the prism of the refractometer. The reading was taken by looking through the eyepiece of the refractometer and the soluble sugar was expressed in °Brix (AOAC, 2000). The Carr's index were identified by determining the bulk density (Db) and tapped density (Dt) of powder. Bulk density was obtained by collecting 50 cm^3 sieved powder (sieve no.20) and introduce into a 100ml graduated cylinder. Then, cylinder was dropped three times from height 1 inch at 2 seconds intervals. The density was calculated by dividing the weight of sample in grams by the final tapped volume in cm^3 of the sample in cylinder. The method was repeated for tapped density with different tapped times (100 times). The Carr's index then were calculated as Eq (1):

$$\text{Carr's index (\%)} = [(Db - Dt)/ Dt] \times 100 \tag{1}$$

Material and Methods

Chemical Properties

Both total flavonoid content (TFC) and antioxidant activity were performed to evaluate the chemical properties of fig powder. TFC was determined spectrophotometrically according to the Dowd method describe by Ramamoorthy and Bono (2007) with slight modification. The 1 ml of sample solution (1 mg/ml) are taken and mixed well with 3 ml of methanol. Then, 0.2 ml of 10 % $AlCl_3$ and 0.2 ml of CH_3CO_2K in 1M are added to the mixture. The solution is held at the dark condition for 30 minutes before absorption readings taken at 420 nm using a UV-Visible spectrophotometer (T60 U, PerkinElmer, U.S.) against the blank sample. The total flavonoid content is determined using a standard curve with quercetin (0, 10, 50, 100 and 200 µg/ml) as the standard. TFC is express as mg of quercetin equivalents (QE) / mg of sample. Antioxidant activity was determined by DPPH radical scavenging activity spectrophotometrically, according to Xu et al. (2008), with slight modification. The 0.1mM DPPH solution had been formulated just before the start of the experiment. Mixtures of reaction; 2 ml of sample, 4 ml of 0.1 mM DPPH solution and 2 ml of methanol were incubated for 30 minutes. The blank solution has also been tested (4 ml 0.1 mM DPPH solution and 2 ml methanol). Following incubation, the absorption reduction was measured with a UV-Vis spectrophotometer at 517 nm as compared to blank. The following formulation calculated the activity of radical scavenging (percentage of inhibition) by Eq (2):

$$\text{\% Inhibition} = [(AB-AA)/AB] \times 100 \tag{2}$$

Where: AB is the absorption of blank sample and AA is the absorption of the tested sample

Statistical Analysis

All the tests were performed in triplicate. The analysis of variance (ANOVA) was applied by IBM SPSS Statistics 21 to determine if there is significant difference between coating material composition. Tukey's Multiple Comparison Test was used for comparisons ($p \leq 0.05$).

Result and Discussion

Physical Properties

The moisture contents of the fig powder ranged between 4.07% and 4.78. The values different significantly ($p < 0.05$) with different composition of coating materials. The low moisture contents of the powders indicated that the samples would have good keeping qualities. Moisture content is the amount of water held in a unit volume of bulk powder as percentage by volume. Fig powder with 100% of maltodextrin exhibit the lowest moisture content compared to others as shown in Table 1. According to Barbosa-Canovas et al. (2005), the requirement of moisture content in food powder is between 4% and 6%. Moisture content below 10% is desirable for food powder to ward off mold growth (Hagan, 2007). The total soluble solids (TSS) ranged between 0.75 and 0.81°Brix. The values different significantly ($p < 0.05$) as the composition of coating materials different. The powder with acacia gum had high °Brix compared to powder with maltodextrin. This could be attributed to higher soluble solids in acacia gum than maltodextrin.

Table 1: Physical Properties of Fig Powder

Properties	**Coating material %**			
	100% Maltodextrin	**100% Acacia Gum**	**75% Maltodextrin: 25% Acacia Gum**	**75% Acacia gum: 25% Maltodextrin**
Moisture content	4.07±0.06	4.78±0.01	4.36±0.01	4.68±0.01
Total Soluble Solid (°Brix)	0.76±0.01	0.80±0.01	0.76±0.01	0.81±0.01
Bulk density	0.39±0.03	0.42±0.04	0.42±0.02	0.45±0.07
Tapped density	0.47±0.06	0.50±0.09	0.52±0.06	0.56±0.02
Hausher ratio	1.14±0.01	1.27±0.01	1.15±0.06	1.37±0.06
Carr's Index	12.51±0.03	21.41±0.02	18.12±0.05	24.97±0.07

Different letters within the same column shows significant difference ($p \leq 0.05$)

The bulk density of fig powder, as shown in Table 1, were between 0.39±0.03 g/cm^3 and 0.45±0.07 g/cm^3. The results of the bulk density were significantly different as the $p \leq 0.05$. The values of fig powder with acacia gum in bulk density was higher compared to fig powder with maltodextrin because of the moisture content in fig powder with acacia gum was higher than the fig powder maltodextrin. The results of tapped density showed a significant difference at $p \leq 0.05$. The values of tapped density of fig powder were between 0.47± 0.06 g/cm^3 and 0.56 ± 0.02 g/cm^3. The inter-particle bonding of acacia gum is strong, coherent junction as the water content was higher compared to the maltodextrin particle, resulting in high tapped density. According to Zea et al. (2013), due to the low particle size, it was able to accommodate more inter-particle friction and thus exhibit the lower range of density of fruits powder. It was clear that a change in coating material composition may result in a significant change in the powder density, since the tapped density and bulk density of food powders depends on the combined values between interrelated elements, such as the intensity of attractive inter-particle forces, particle size and number of contact points (Ortega-Rivas, 2005).

Higher Carr's index and Hausner ratio of powder exhibited as 'difficult' to flow. This may be due to the moisture content and hygroscopicity of individual fruit powders. Acacia gum is composed of branched arrangement of simple sugars like galactose, glucuronic acid, arabinose and rhamnose and small amount of covalently bonded protein. Those may be the reason of high Carr's index and Hausner ratio of fig powder with acacia gum compared to fig with maltodextrin (Table 1). Hayes (1987) reported that when the Hausner ratio is between 1.0 and 1.1, the powder is considered to be free flowing, the powder with the Hausner ratio between

1.1 and 1.25 is considered to be medium flowing, while the difficult flowing belongs to powder with the Hausner ratio from 1.25 to 1.4; and the powder has very difficult flowing when the Hausner ratio is greater than 1.4. In relation to handling properties, lower Hausner ratio values indicate desirable cohesiveness properties that are correlated to better flowability characteristics. A free-flowing material has a low tendency for further consolidation, which is helpful for preventing production stoppages at industrial scale.

Chemical Properties

Encapsulation technique has been reported to protect the bioactive compounds' antioxidant activity. For this reason, bioactive compounds were encapsulated into microsystems, so to prevent itself from oxidation/ degradation processes (Lauro et al., 2015). DPPH assay was reported as a percentage of inhibition against DPPH radical and the percentage were ranged from 29.54 to 32.18% (Figure 2). DPPH assay were performed to evaluate the antioxidant capacity of different coating material composition. The antioxidant activity of coating material was type-concentration dependent. There existed positive correlation between flavonoids content and antioxidant activity in fig powder. Different composition of coating materials results in different flavonoid content. When the composition of coating material is 100% of maltodextrin and 100% acacia gum, the total flavonoids content in fig powder were corresponding to 13.38 mg QE/ mg and 17.21 mg QE/ mg. The antioxidant activity by DPPH percentage of inhibition achieved 29.55% and 30.11%, respectively. The total flavonoid and antioxidant activity slightly improved in fig powder with combination of coating materials. The flavonoids content 27.83 mg QE/ mg and 30.99 mg/ QE/ mg were observed for fig powder contain 75% maltodextrin with 25% acacia gum and 75% acacia gum with 25% maltodextrin, respectively, and the DPPH inhibition percentage reached 31.56% and 32.19%.

These results demonstrated that coating materials preserved the antioxidant activity of the encapsulated nature ingredient, and closely related to flavonoids content. The antioxidant activity of fig powder with acacia gum was higher than that with maltodextrin, most likely because the flavonoids content of acacia gum is higher compared to maltodextrin. Different composition of coating materials significantly affects the antioxidant activity. Anyway, it is certain that coating materials preserved and improved the antioxidant activity of encapsulation of fig phytochemical which is flavonoids. The cooperative adsorption of polysaccharide and protein at emulsion interface could provide excellent physical and oxidative stability then prevent flavonoids from oxidation and degradation. Then free radical scavenging ability was improved (Yao et al., 2016).

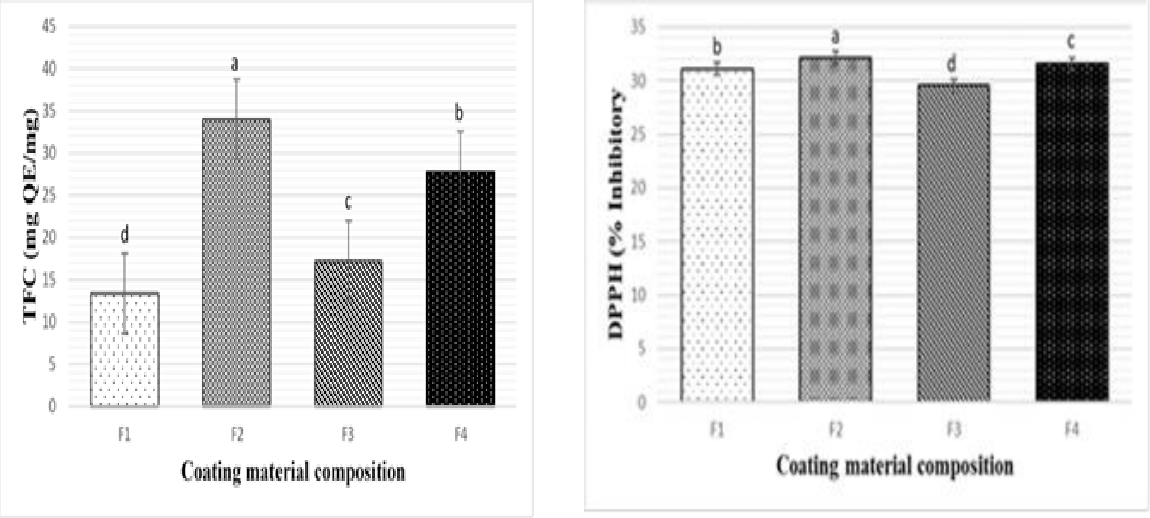

(a) (b)

Figure 1: The Total Flavonoid Content (a) and Antioxidant Activity (b) Value of Fig Powder; F1 (100% Maltodextrin), F2 (100% Acacia Gum), F3 (75% Maltodextrin: 25% Acacia Gum), and F4 (75% Acacia Gum: 25% Maltodextrin). Different letters show significant different ($p \leq 0.05$)

Conclusion

In this study, to get the best encapsulation formulation, fig juice was coated with different ratios of maltodextrin and acacia gum combinations. By changing the ratio of maltodextrin and acacia gum as a coating material, statistically different of moisture, total soluble solid, tapped density, bulk density, Carr’s index and Hausner ratio could be obtained. Usage of different composition of maltodextrin and acacia gum also affect antioxidant activity significantly. Hence, the best formulation for encapsulation of fig juice is 75% acacia gum with 25% maltodextrin. For the future study, Encapsulation of food material with right coating materials combination will improve physical and chemical properties of food powder. Then the food powder can be used in nutraceutical or functional food development.

Conflict of interest

The authors declare no conflict of interest.

Acknowledgement

This work is funded under Prototype Research Grant Scheme by Malaysia’s Ministry of Higher Education (PRGS/11/2020/WAB03/UTHM/01/1). Appreciation also to he Malaysia’s Ministry of Higher Education under Hadiah Latihan Persekutuan (HLP) with Cuti Belajar Bergaji Penuh (CBBP) for the funding of the author PhD research study at Universiti Tun Hussein Onn Malaysia (UTHM). Special thanks to UTHM for having provided facilities for carrying out this research.

References

Ameh, A. O., Isa, M. T., Ahmed, A. S., & Adamu, S. B. (2009). Studies on the use of trona in improving the taste of the extract from Hibiscus sabdariffa calyx. Nigerian Journal of Pharmaceutical Sciences, 8, 7–12

AOAC. (2000). Official methods of analysis of AOAC International (17th ed.). Arlinton, TX: Author

Bhandari, B. R., Datta, N., & T. Howes, Problems associated with spray drying of sugar-rich foods, Drying Technology 15 (1997) 671–684.

Cao, G., Sofic, E., & Prior, R. L. (1997). Original Contribution. 22(5), 749–760.

Dubey, R., Shami, T. C., and Rao, K.. U. B., 2009. Microencapsulation Technology and Applications. Defence Science Journal, 59(1), 82–95.

Eichie, F. E. & Kudehinbu, A. O. (2009). Effect of particle size of granules on some mechanical properties of paracetamol tablets, Journal of Biotechnology 8 (2009) 5913–5916.

Fasoyiro, S. B., Babalola, S. O., & Owosibo, T. (2005). Chemical composition and sensory quality of fruit-flavoured roselle (Hibiscus sabdariffa) drinks. World Journal of Agricultural Sciences, 1, 161–164

Farhangi, H., Ajilian, M., Saeidi, M., & Khodaei, G. H. (2014). Medicinal fruits in Holy Quran. International Journal of Pediatrics.

Hayes, G. D. (1987). Food Engineering Data Handbook. Longman Scientific & Technical: London, p. 200

Lauro, M. R., Crasci, L., Carbone, C., Aquino, R. P., Panico, A. M., & Puglisi, G. (2015). Encapsulation of a citrus by-product extract: Development, characterization and stabilitu studies of a nutraceutical with antioxidant and metalloproteinases inhibitory activity. LWT – Food Science and Technology 62 (1, Part 1), 169-176.

Luvonga, W. A., Njoroge, M. S., Makokha, A., & Ngunjiri, P. W. (2010, November). Chemical characterisation of hibiscus sabdariffa (roselle) calyces and evaluation of its functional potential in the food industry. In Science and Technology and Innovation for Industrialisation and Sustainable Development Proceedings of the 2010 JKUAT Scientific, Technological and Industrialisation Conference (pp. 631– 638). Nairobi: Jomo Kenyatta University of Agriculture and Technology

Madene, A., Jacquot, M., Scher, J., & Desobry, S. (2006). Review Flavour encapsulation and controlled release – a review. International Journal of Food Science and Technology, 41, 1–21.

Mcnamee, B. F., O’Riordan, E. D., & O’Sullivan, M. (1998). Emulsification and Microencapsulation Properties of Gum Arabic. Journal of Agricultural and Food Chemistry, 46, 4551–4555.

Mahmoudi, S., Khali, M., Benkhaled, A., Boucetta, I., Dahmani, Y., Attallah, Z., & Belbraouet, S. (2018). Fresh figs (Ficus carica L.): Pomological characteristics, nutritional value, and phytochemical properties. In European Journal of Horticultural Science (Vol. 83).

Ma, Z. F., & Zhang, H. (2017). Phytochemical constituents, health benefits, and industrial applications of grape seeds: Amini-review. Antioxidants, 6(3), 1–11.

Mnari, A. B., Harzallah, A., Amri, Z., Dhaou Aguir, S., & Hammami, M. (2016a). Phytochemical Content, Antioxidant Properties, and Phenolic Profile of Tunisian Raisin Varieties (Vitis Vinifera L.). International Journal of Food Properties.

Muhammed, P., & Shamsi, M. S. (2016). Tibb-e-Nabawi: Medical Guidance & Teachings of. 2016(May), 1–305.

Marwat, S., Khan, M., Khan, M., Ahmad, M., Zafar, M., & Sultana, S. (2009). Fruit Plant Species Mentioned in the Holy Quran and Ahadith and Their Ethnomedicinal Importance. In American-Eurasian J. Agric. & Environ. Sci (Vol. 5).

Ortega-Rivas, E. (2005). Handling and Processing of Food Powders and Particulates, in “Encapsulated and Powdered Foods”. In: Onwulata, C. (Ed.). CRC Press, pp. 75-144.

Ramamoorthy, P., and Bono, A. (2007). Antioxidant activity, total phenolic and flavonoid content of Morinda citrifolia fruit extracts from various extraction processes. Journal of Engineering Science and Technology.

Rosenberg, M., & Sheu, T. Y. (1995). Microencapsulation by Spray Drying Ethyl Caprylate Protein and Carbohydrate Wall Systems in Whey. Journal of Food Science, 60(1).

Soni, N., Mehta, S., Satpathy, G., & Gupta, R. K. (2014). Estimation of nutritional, phytochemical, antioxidant and antibacterial activity of dried fig (Ficus carica). Journal of Pharmacognosy and Phytochemistry.

Xu, G., Liu, D., Chen, J., Ye, X., Ma, Y., & Shi, J. (2008). Juice components and antioxidant capacity of citrus varieties cultivated in China. Food Chemistry, 106, 2, 545-551.

Yao, X., Xiang, S., Nie, K., Gao, Z., Zhang, W., Fang, Y. (2016). Whey protein isolate/gum Arabic intramolecular soluble complexes improving the physical and oxidative stabilities of conjugated linoleic acid emulsions. RSC Advances 6 (18), 14635-14642

Zea, L.P., Yusof, Y. A., Aziz, M. G., Chin, N. L., & Amaiza, M. A. (2013). Compressibility and Dissolution Characteristics of Mixed Fruit Tablets Made from Guava and Pitaya Fruit Powders. Powder Technology 243, 112-119.

Zuidam, N. J., & Nedović, V. (2010), Encapsulation Technologies for Active Food Ingredients and Food Processing (pp. 31-100). London: Springer.

International Research Conference on Applied Sciences
and Engineering 2020 (IRCASE 2020)
eISBN 978-967-2426-20-2
13th – 14th December 2020

ADVANCES IN ANTIFOULING STRATEGIES IN MEMBRANE ULTRAFILTRATION: A BRIEF REVIEW

Amina Tahreen[1]
Mohammed Saedi Jami[2]

[1]Faculty of Engineering, International Islamic University Malaysia (IIUM), Malaysia, (E-mail: aminatahreen@gmail.com)
[2]Faculty of Engineering, International Islamic University Malaysia (IIUM), Malaysia, (E-mail: saedi@iium.edu.my)

Abstract: *This study briefly reviews the recent advances in membrane and separation technology for antifouling strategies for membrane ultrafiltration. Membrane fouling is inevitable in ultrafiltration due to the eventual membrane pore blockage with foulants. Consequently, flux declines and affects the membrane integrity over time along with elevation in processing time and thereby complicating the overall membrane maintenance. To combat this issue, several studies had been undertaken such as grafting of* TiO_2 *nanotubes (TNTs), graphene oxide nanosheets, zwitterions or polymers in the membrane and also by applying direct current. Moreover, many researchers emphasized on the integration of an enhanced pre-treatment process such as adsorption, coagulation, electrocoagulation and so on. By critically analysing and comparing the existing studies, the impact, suitability, efficiency and sustainability of the antifouling strategies will be discussed in this review. This refined approach of observing the progress in membrane technology will enable the determination of the existing gaps in the studies and will help to expand and propel the field further in separation efficiency.*

Keywords: *Crossflow, Ultrafiltration, Antifouling, Separation, Membrane*

Introduction

In water/wastewater treatment, commercially available polymeric ultrafiltration membranes had drawn significant attention (He et al., 2018). Fouling remains an obstacle that affects long-term membrane efficiency, as membrane technology plays an increasingly important role in water/wastewater treatment systems. Fouling is a pore blocking phenomenon due to pollutants, in membrane filtration, if left unchecked, hinders the membrane performance with dramatic flux decline (Geng et al., 2017). It is an inevitable occurrence as one of the four types of fouling takes over as modelled by Hermia, namely standard blocking, intermediate blocking, complete blocking and cake formation in membrane filtration (Hermia, 1982), presented in Figure 1. Importantly, identifying and establishing the type of blocking taking place for a particular membrane filtration enables the scalability of the system, evaluation of the durable membrane performance, and to devise suitable anti-fouling strategies for improving the membrane integrity and performance.

From the two modes of membrane ultrafiltration operation, crossflow and dead-end, crossflow ultrafiltration stands out to be the most suitable mode for long term and continuous treatment of water/wastewater. As the constant inflow of feed in crossflow mode, disrupts the settling of foulants on the membrane surface, the frequent build of cake layer due to the parallel feed and permeate direction, can be minimized to a significant extent. The effect of the difference in both crossflow and dead-end filtration operation on the foulant deposition can be visualized in Figure 2, where the feed is palm oil mill effluent (POME), an example of highly polluted industrial wastewater.

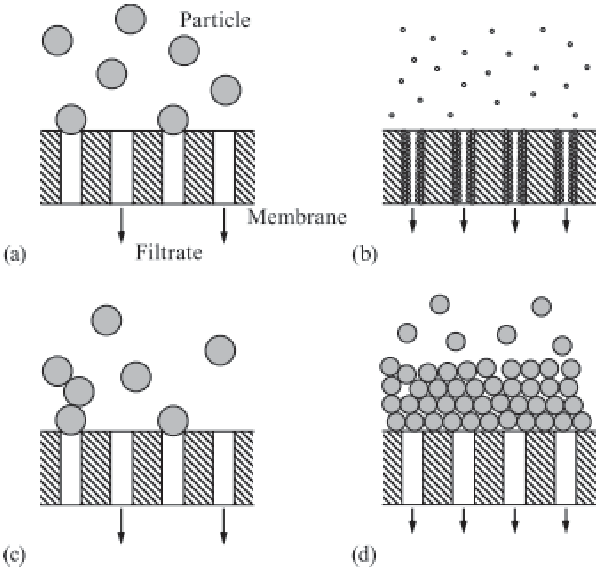

Figure 1: Schematic Diagram of the Four Blocking Filtration Laws: (a) Complete Blocking, (b) Standard Blocking, (c) Intermediate Blocking, and (d) Cake Filtration.

Source: (Iritani & Katagiri, 2016)

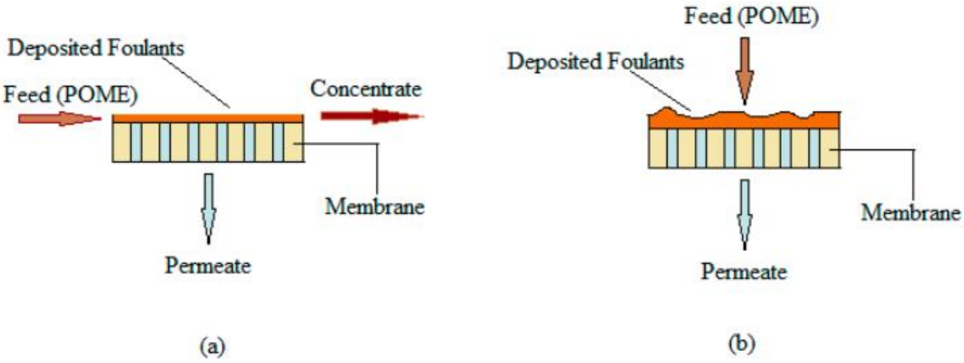

Figure 2: Schematic Diagram of Membrane Operation (a) Crossflow and (b) Dead-End Filtration

Source: (Abdulsalam et al., 2018)

To tackle fouling, the conventional practices employed include rigorous hydraulic regulation and constant chemical cleaning, that impacts environmental sustainability by using large amount of chemicals and heavy energy consumption, and reduces the membrane lifespan (Xiao et al., 2019). By studying the mechanisms involved in a particular type of fouling, the most efficient antifouling method can be devised. The mechanisms that incur fouling primarily depend on the foulant (pore blocking pollutant) type, the membrane type and their interactions (Lin et al., 2010). Both foulant-foulant interaction and membrane-foulant interaction can be explained in terms of covalent and non-covalent interactions, and spatial effects (Xu et al., 2020). Studying these interaction mechanisms enables the possibility of devising antifouling strategies that target these interactions. Antifouling methods can be devised by inhibiting the migration of foulants, modifying membrane surface characteristics, conditioning the foulant and membrane cleaning (Xu et al., 2020).

Membrane Cleaning

Membrane cleaning involves disrupting the foulant-membrane interactions either physically by hydraulic cleaning, air-aided cleaning, ultrasonic cleaning etc. (Lin et al., 2010) or chemically by adding membrane cleaning agents such as acid, alkali, oxidant, reductant, surfactant, enzyme etc. depending on the targeted fouling interaction and foulant type (Xu et al., 2020). Frequent chemical additions along with additional costs for chemicals, result in by-products that are detrimental to the environment and can affect the membrane integrity in the long run. Therefore, comparatively, physical membrane cleaning is an eco-friendlier process, but notably poses a constraint in power consumption and energy costs.

Foulant Migration Inhibition

To inhibit the movement of foulants in ultrafiltration membrane systems, raising crossflow intensity, integrating movable parts to facilitate turbulence, and disrupting the boundary layer of mass transfer through high rotation frequency of spiral flow can be employed (Cabassud et al., 2001; Kondo et al., 2012; Zakrzewska-Trznadel et al., 2009). Applying spiral flow, and increased crossflow intensity can remarkably reduce fouling by inhibiting the foulants to settle into or on the pores due to the force exerted from the varied flow hydrodynamics. However, incorporating moving parts in the membrane system raises the complexity of the overall system and adds up to the obstacles in troubleshooting the membrane system for errors in its operation.

Pre-Treatment

Several researchers have carried out studies that incorporate a physical (Amosa et al., 2016), biological (Tian et al., 2012), photochemical (Alhaji et al., 2016), chemical (Lin et al., 1997) or electrochemical treatment (Moussa et al., 2017; Naje et al., 2017; Tahreen et al., 2020) of water/wastewater to be treated before proceeding to the membrane filtration. Pre-treatment is one of the best strategies to integrate with membrane ultrafiltration, as the pre-conditioning of foulants enables the drastic reduction in membrane fouling and ensuring long term performance efficiency. Therefore, a more controlled initial foulant concentration through the suitable pre-treatment can drastically enhance the membrane filtration system protecting the membrane integrity in the long run. However, the most suitable pre-treatment method must be strategically chosen depending on the foulant type and studying the fouling-membrane interactions. Electrocoagulation has been rapidly advancing in treating a wide range of wastewater with its simple setup, eco-friendly nature and versatility (Aswathy et al., 2016; Bashir et al., 2019; Changmai et al., 2019; Nasrullah et al., 2020; Nawarkar & Salkar, 2019; Tahreen et al., 2020).

Membrane Surface Modification

The fastest growing field in antifouling method development is membrane surface modification. It has played a significant part in propelling membrane technology forward with its effective and sustainable antifouling properties. The prominent methods against the common hydrophobic foulant-membrane interaction include hydrophilic modifications in membrane fabrication in substrate by copolymerization (Wang et al., 2018) or blending (Jin et al., 2019). Beside substrate alteration, grafting/coating of hydrophilic (Li et al., 2015) or super hydrophilic compounds or zwitterions (Shahkaramipour et al., 2020), on the membrane surface has been studied. Deposition of an added layer on the membrane surface contrary to the charge of the occurring electrostatic attraction, can enhance the membrane antifouling properties.

(Liang et al., 2019). Moreover, altering the membrane surface geometry in terms of pore morphology (Fan et al., 2018) and roughness (Feng et al., 2017; Li et al., 2015) contributes to the controlling of the spatial effects for enhancing antifouling properties.

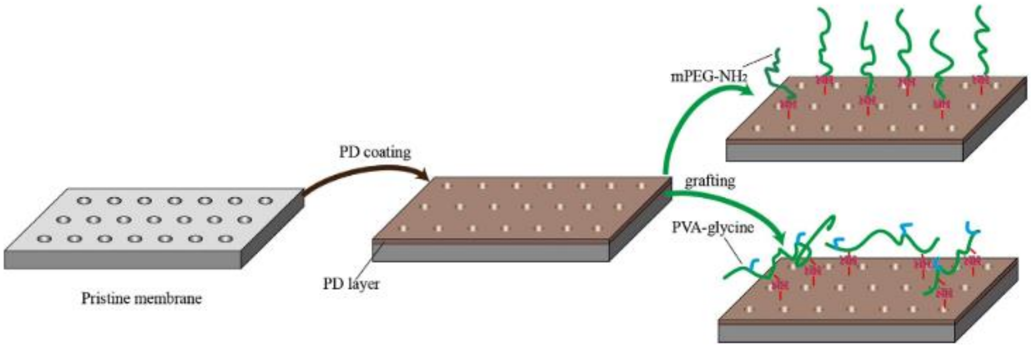

Figure 3: Schematic Diagram of PES Membrane Surface Modification
Source: (Li et al., 2015)

Typical membrane types used for ultrafiltration are polyvinylidenefluoride (PVDF), polyethersulfone (PES), polysulfone (PSf) and sulfonated polysulfone (SPSf). Coating the membrane surface with polydopamine (PD) having grafted hydrophilic polymers has been increasingly employed for antifouling studies (Li et al., 2015). A schematic diagram of the PES membrane coated with PD followed by amine and glycine-based polymer grafting is shown in Figure 3. Prominent grafting polymers and compounds include polyethylene glycol (PEG) (An et al., 2020), polysiloxane (Tran et al., 2020), graphene oxide (GO) (Chen et al., 2020; Hu et al., 2019), zwitterions (Huang et al., 2018; Shahkaramipour et al., 2020) and titanium oxides (TNTs) with fluoride (F) and carboxyl group (COOH) incorporation (Geng et al., 2019). In Table 1, the key results of these studies have been summarised.

Table 1: Recent Notable Advances in Antifouling Strategies

Reference	Membrane Type	Antifouling Strategy	Main Finding
(An et al., 2020)	PVDF	PD/PEG co-deposition	Increased hydrophilicity proved to convert irreversible fouling to reversible
(Chen et al., 2020)	PSf	PD/GO nanosheets grafting	Fouling rate reduced by 63% compared to pristine membrane, critical flux increased by 20%
(Shahkaramipour et al., 2020)	PSf	PD/zwitterion co-deposition	The grafted membrane showed 15% - 25% reduced resistance to water permeation
(Tran et al., 2020)	PSf	PD/Polysiloxane grafting	Fouling rate lowered by 70%
(Hu et al., 2019)	PES/SPSf	GO loading	Enhanced hydrophilicity and GO nano-size effect resulted in 94.2% fouling recovery
(Geng et al., 2019)	PES	TNTs-F-COOH bonding on PES	Increased ratio of flux recovery to 80% after solar irradiation simulation on the fabricated membrane

Conclusion

In this paper, the techniques for improving the antifouling properties of membrane ultrafiltration were reviewed. The recent advancements in membrane antifouling strategies depict remarkably high fouling recovery rates. GO loading proved to be an impressive enhancer of membrane hydrophilicity that led to a fouling recovery of 94.2%. The nano-size effect of GO makes it a promising grafting compound for membrane surfaces to improve membrane antifouling with a finer distribution of hydrophilicity. Besides, incorporation of TNTs on membrane surface, facilitating membrane self-cleaning with solar irradiation, is a remarkable research direction in sustainable membrane technology. Further studies must be undertaken with upscaled membrane ultrafiltration systems with fouling mechanism modelling and its specific antifouling strategy, and the possibility of grafted polymers leaking in treated permeate and its environmental impact.

Acknowledgement

This study had been supported by the grant: FRGS 19-194-0803 by Ministry of Education Malaysia, and TFW 2019 scheme by the Faculty of Engineering, International Islamic University Malaysia.

References

Abdulsalam, M., Man, H. C., Idris, A. I., Yunos, K. F., & Abidin, Z. Z. (2018). Treatment of palm oil mill effluent using membrane bioreactor: Novel processes and their major drawbacks. *Water (Switzerland)*, *10*(9). https://doi.org/10.3390/w10091165

Alhaji, M. H., Sanaullah, K., Lim, S. F., Khan, A., Hipolito, C. N., Abdullah, M. O., … Jamil, T. (2016). Photocatalytic treatment technology for palm oil mill effluent (POME) - A review. *Process Safety and Environmental Protection*, *102*, 673–686. https://doi.org/10.1016/j.psep.2016.05.020

Amosa, M. K., Jami, M. S., Alkhatib, M. F. R., & Majozi, T. (2016). Studies on pore blocking mechanism and technical feasibility of a hybrid PAC-MF process for reclamation of irrigation water from biotreated POME. *Separation Science and Technology (Philadelphia)*, *51*(12), 2047–2061. https://doi.org/10.1080/01496395.2016.1192192

An, Z. H., An, Z. H., Wang, H. Z., & Ruan, G. L. (2020). Robust surface stability and enhanced anti-fouling property on PVDF ultrafiltration membrane surface: PDA/PEG co-deposition versus traditional PDA coating. *IOP Conference Series: Earth and Environmental Science*, *512*(1). https://doi.org/10.1088/1755-1315/512/1/012182

Aswathy, P., Gandhimathi, R., Ramesh, S. T., & Nidheesh, P. V. (2016). Removal of organics from bilge water by batch electrocoagulation process. *Separation and Purification Technology*, *159*, 108–115. https://doi.org/10.1016/j.seppur.2016.01.001

Bashir, M. J., Lim, J. H., Abu Amr, S. S., Wong, L. P., & Sim, Y. L. (2019). Post treatment of palm oil mill effluent using electro-coagulation-peroxidation (ECP) technique. *Journal of Cleaner Production*, *208*, 716–727. https://doi.org/10.1016/j.jclepro.2018.10.073

Cabassud, C., Laborie, S., Durand-Bourlier, L., & Lainé, J. M. (2001). Air sparging in ultrafiltration hollow fibers: Relationship between flux enhancement, cake characteristics and hydrodynamic parameters. *Journal of Membrane Science*, *181*(1), 57–69. https://doi.org/10.1016/S0376-7388(00)00538-X

Changmai, M., Pasawan, M., & Purkait, M. K. (2019). Treatment of oily wastewater from drilling site using electrocoagulation followed by microfiltration. *Separation and Purification Technology*, *210*, 463–472. https://doi.org/10.1016/j.seppur.2018.08.007

Chen, X., Deng, E., Park, D., Pfeifer, B. A., Dai, N., & Lin, H. (2020). Grafting Activated Graphene Oxide Nanosheets onto Ultrafiltration Membranes Using Polydopamine to Enhance Antifouling Properties. *ACS Applied Materials & Interfaces*, *12*(42), 48179–48187. https://doi.org/10.1021/acsami.0c14210

Dideikin, A. T., & Vul', A. Y. (2019). Graphene oxide and derivatives: The place in graphene family. *Frontiers in Physics*, *6*(JAN). https://doi.org/10.3389/fphy.2018.00149

Fan, H., Xiao, K., Mu, S., Zhou, Y., Ma, J., Wang, X., & Huang, X. (2018). Impact of membrane pore morphology on multi-cycle fouling and cleaning of hydrophobic and hydrophilic membranes during MBR operation. *Journal of Membrane Science*, *556*, 312–320. https://doi.org/10.1016/j.memsci.2018.04.014

Feng, S., Yu, G., Cai, X., Eulade, M., Lin, H., Chen, J., … Liao, B. Q. (2017). Effects of fractal roughness of membrane surfaces on interfacial interactions associated with membrane fouling in a membrane bioreactor. *Bioresource Technology*, *244*, 560–568. https://doi.org/10.1016/j.biortech.2017.07.160

Geng, Z., Wang, X., Jiang, H., Zhang, L., Chen, Z., Feng, Y., … Sun, J. (2019). High-performance TiO2 nanotubes/poly(aryl ether sulfone) hybrid self-cleaning anti-fouling ultrafiltration membranes. *Polymers*, *11*(3). https://doi.org/10.3390/polym11030555

Geng, Z., Yang, X., Boo, C., Zhu, S., Lu, Y., Fan, W., … Yang, X. (2017). Self-cleaning anti-fouling hybrid ultrafiltration membranes via side chain grafting of poly(aryl ether sulfone) and titanium dioxide. *Journal of Membrane Science*, *529*, 1–10. https://doi.org/10.1016/j.memsci.2017.01.043

He, J., Cui, A., Deng, S., & Chen, J. P. (2018). Treatment of methylene blue containing wastewater by a cost-effective micro-scale biochar/polysulfone mixed matrix hollow fiber membrane: Performance and mechanism studies. *Journal of Colloid and Interface Science*, *512*, 190–197. https://doi.org/10.1016/j.jcis.2017.09.106

Hermia, J. (1982). *Constant pressure blocking filtration laws: application to power-law non-Newtonian fluids*.

Hu, M., Cui, Z., Li, J., Zhang, L., Mo, Y., Dlamini, D. S., … Matsuyama, H. (2019). Ultra-low graphene oxide loading for water permeability, antifouling and antibacterial improvement of polyethersulfone/sulfonated polysulfone ultrafiltration membranes. *Journal of Colloid and Interface Science*, *552*, 319–331. https://doi.org/10.1016/j.jcis.2019.05.065

Huang, S., Ras, R. H. A., & Tian, X. (2018). Antifouling membranes for oily wastewater treatment: Interplay between wetting and membrane fouling. *Current Opinion in Colloid and Interface Science*, *36*, 90–109. https://doi.org/10.1016/j.cocis.2018.02.002

Iritani, E., & Katagiri, N. (2016). Developments of blocking filtration model in membrane filtration. *KONA Powder and Particle Journal*, Vol. 2016, pp. 179–202. https://doi.org/10.14356/kona.2016024

Jin, Y. tao, Hu, D., Lin, Y. kai, & Shi, L. (2019). Hydrophilic modification of polyvinylidene fluoride membrane by blending amphiphilic copolymer via thermally induced phase separation. *Polymers for Advanced Technologies*, *30*(1), 110–119. https://doi.org/10.1002/pat.4449

Kondo, M., Cumin, J., Hong, Y., Bayly, R., Gao, M., & Rubin, R. (2012). Reexamination of the Gas Sparging Mechanism for Membrane Fouling Control. *Proceedings of the Water Environment Federation*, *2010*(9), 6986–7007. https://doi.org/10.2175/193864710798207495

Li, F., Ye, J., Yang, L., Deng, C., Tian, Q., & Yang, B. (2015). Surface modification of ultrafiltration membranes by grafting glycine-functionalized PVA based on polydopamine coatings. *Applied Surface Science*, *345*, 301–309. https://doi.org/10.1016/j.apsusc.2015.03.189

Liang, S., Li, M., Cao, J., Zuo, K., Bian, Y., Xiao, K., & Huang, X. (2019). Integrated ultrafiltration–capacitive-deionization (UCDI) for enhanced antifouling performance and synchronous removal of organic matter and salts. *Separation and Purification Technology*, *226*(November 2018), 146–153. https://doi.org/10.1016/j.seppur.2019.05.085

Lin, S. H., & Chen, M. L. (1997). Treatment of textile wastewater by-chemical methods for reuse. *Water Research*, *31*(4), 868–876. https://doi.org/10.1016/S0043-1354(96)00318-1

Lin, J. C. Te, Lee, D. J., & Huang, C. (2010). Membrane fouling mitigation: Membrane cleaning. *Separation Science and Technology*, *45*(7), 858–872. https://doi.org/10.1080/01496391003666940

Moussa, D. T., El-Naas, M. H., Nasser, M., & Al-Marri, M. J. (2017). A comprehensive review of electrocoagulation for water treatment: Potentials and challenges. *Journal of Environmental Management*, *186*, 24–41. https://doi.org/10.1016/j.jenvman.2016.10.032

Naje, A. S., Chelliapan, S., Zakaria, Z., Ajeel, M. A., & Alaba, P. A. (2017). A review of electrocoagulation technology for the treatment of textile wastewater. *Reviews in Chemical Engineering*, *33*(3), 263–292. https://doi.org/10.1515/revce-2016-0019

Nasrullah, M., Singh, L., Krishnan, S., Sakinah, M., Mahapatra, D. M., & Zularisam, A. W. (2020). Electrocoagulation treatment of raw palm oil mill effluent: Effect of operating parameters on floc growth and structure. *Journal of Water Process Engineering*, *33*(August 2019), 101114. https://doi.org/10.1016/j.jwpe.2019.101114

Nawarkar, C. J., & Salkar, V. D. (2019). Solar powered Electrocoagulation system for municipal wastewater treatment. *Fuel*, *237*, 222–226. https://doi.org/10.1016/j.fuel.2018.09.140

Shahkaramipour, N., Jafari, A., Tran, T., Stafford, C. M., Cheng, C., & Lin, H. (2020). Maximizing the grafting of zwitterions onto the surface of ultrafiltration membranes to improve antifouling properties. *Journal of Membrane Science*, *601*(January), 117909. https://doi.org/10.1016/j.memsci.2020.117909

Tahreen, A., Jami, M. S., & Ali, F. (2020). Role of electrocoagulation in wastewater treatment: A developmental review. *Journal of Water Process Engineering*, *37*, 101440. https://doi.org/10.1016/j.jwpe.2020.101440

Tian, Y., Li, Z., & Lu, Y. (2012). Changes in characteristics of soluble microbial products and extracellular polymeric substances in membrane bioreactor coupled with worm reactor: Relation to membrane fouling. *Bioresource Technology*, *122*, 62–69. https://doi.org/10.1016/j.biortech.2012.05.009

Tran, T., Chen, X., Doshi, S., Stafford, C. M., & Lin, H. (2020). Grafting polysiloxane onto ultrafiltration membranes to optimize surface energy and mitigate fouling. *Soft Matter*, *16*(21), 5044–5053. https://doi.org/10.1039/d0sm00551g

Wang, Z., Xiao, K., & Wang, X. mao. (2018). Role of coexistence of negative and positive membrane surface charges in electrostatic effect for salt rejection by nanofiltration. *Desalination*, *444*(June), 75–83. https://doi.org/10.1016/j.desal.2018.07.010

Xiao, K., Liang, S., Wang, X., Chen, C., & Huang, X. (2019). Current state and challenges of full-scale membrane bioreactor applications: A critical review. *Bioresource Technology*, *271*, 473–481. https://doi.org/10.1016/j.biortech.2018.09.061

Xu, H., Xiao, K., Wang, X., Liang, S., Wei, C., Wen, X., & Huang, X. (2020). Outlining the Roles of Membrane-Foulant and Foulant-Foulant Interactions in Organic Fouling During Microfiltration and Ultrafiltration: A Mini-Review. *Frontiers in Chemistry*, *8*(June), 1–14. https://doi.org/10.3389/fchem.2020.00417

Zakrzewska-Trznadel, G., Harasimowicz, M., Miśkiewicz, A., Jaworska, A., Dłuska, E., & Wroński, S. (2009). Reducing fouling and boundary-layer by application of helical flow in ultrafiltration module employed for radioactive wastes processing. *Desalination*, *240*(1–3), 108–116. https://doi.org/10.1016/j.desal.2007.10.091

International Research Conference on Applied Sciences and Engineering 2020 (IRCASE 2020)
eISBN 978-967-2426-20-2
13th – 14th December 2020

GENOTYPIC AND PHENOTYPIC CHARACTERISATION OF ISOLATED MARINE BACTERIA AND ITS POTENTIAL TO PRODUCE ALKALINE PROTEASE

Maya Dehimi[1]
Faridah Yusof [2*]
RAHA AHMAD RAUS[3]
NOOR FAIZUL HADRY[4]
RADHIA NEDJAI[5]

[1]Faculty Engineering, International Islamic University Malaysia, (E-mail: mayadehimi@gmail.com).
[2]Faculty Engineering, International Islamic University Malaysia, (E-mail: yfaridah@iium.edu.my).
[3]Faculty Engineering, International Islamic University Malaysia. (E-mail: rahar@iium.edu.my).
[4]Faculty Engineering, International Islamic University Malaysia. (E-mail: faizul@iium.edu.my).
[5]Faculty Engineering, International Islamic University Malaysia. (E-mail: nedjai.redhia@live.iium.edu.my).

Abstract: *In several industries such as food and detergent, enzymes are commonly used out of which microorganisms' proteolytic enzymes are dominant. Microorganisms from marine sources have advantageous commercial characteristics when it comes to protease production. Protease producing bacterial strains were isolated from four different stations in the South China Sea, located at Kuantan, Pahang-Malaysia. The temperature was ranging from 29 to 36.2°C; salinity varied from 36,18 to 37,9 ppt, turbidity from 10.21 to 16.4 NTU. Dissolved Oxygen had an average of 4.44 mg/mL, and pH was around 8. All the bacterial strains were screened for protease activity using Skim Milk agar plates. Out of 18 isolates, ten strains formed a clear zone on skim milk agar plates. Molecular identification by 16S rRNA results revealed that Bacillus spp was the most dominant bacteria, four isolates belong to Bacillus cereus, another 04 identified as Bacillus licheniformis in addition of one isolate was Bacillus safensis. They were followed by one isolate Staphylococcus warneri. Furthermore, a phenotypic characterization is conducted using The Biolog GENIII MicroPlate with 94 phenotypic tests. These tests consist of 71 carbon source utilization assays and 23 chemical sensitivity assays. The proteolytic activity was confirmed through a quantitative protease assay. Where the strain B. cereus-MD152 was the highest yield, followed by B. licheniformis-ABN13. On the contrary, the lowest yield was secreted by B. cereus-IIUM6 with no more than 16.5 U/ml.*

Keywords: *Protease production, bacteria identification, bacteria characterisation, marine Bacillus.*

Introduction

The marine environment is considered the world's most important underwater habitat and the primary biodiversity source on the earth. The biological diversity of aquatic habitats is reckoned to be significantly greater than in tropical rain forests.(Haefner, 2003). (Caron, Worden, Countway, Demir, & Heidelberg, 2009) reported that the new high-throughput technologies have demonstrated about 20,000 species per liter of seawater samples, with 178,000 species dropping below 34 phyla, microorganisms are considered as the foremost plentiful organisms in the oceans (UEPA, 2006). A significant portion of the maritime microbial population has been obscure such as the least explored naval protists (Hahn, 2006). Bacterial distribution, relying on variations in water salinity, temperature as well as other physicochemical parameters (Alavandi, 1990). Marine habitats display unusual characteristics arising from the rare mixture of multiple physical factors. These habitats allow microorganisms to survive At high pressure, low temperatures in the Arctic and Antarctic cold waters, differing pHs, and salinity (Faulkner, 2001) Much of these microorganisms are used in a large variety of biotechnological applications to provide new companies with innovative bioactive compounds and biocatalysts (de Pascale, De Santi, Fu, & Landfald, 2012; Kennedy et al., 2011). The cumulative bioactive compounds discovered by marine sources account for 70 % of bacteria, whereas the rest are for fungi and other domains (Prabavathy, Mathivanan, & Murugesan, 2006).

In comparison to chemical catalysts, microbial enzymes economically and ecologically improve bioprocess reactions by their unique characteristics, including pH resistance, temperatures, and other harsh reaction conditions(Nigam, 2013). *Bacillus* species create fully half of the enzymes generated on the world market, and about 60% of these are proteases(Reddy, Wee, Yun, & Ryu, 2008). Even so, there have been limited studies on the

alkaline protease production from marine microorganisms (Chi et al., 2005).

Proteases are a group of enzymes, which have a catalytic function to disintegrate peptide bonds of proteins and break them down into small peptides or amino acids (Fulzele, Desa, Yadav, Shouche, & Bhadekar, 2011; Prabakaran. V1, Soma Prabha. A2. And Blessy Thayalin, 2016) produced in their exponential phase of the growth curve (Nurullah, 2012). Proteases have applications in different manufacturers such as food detergent, pharmaceuticals, leather, and silk, and for recovery of silver from used X-ray films as well. Furthermore, they are applied in some medical applications and for meat tenderization (Fulzele et al., 2011). Where, they constitute one of the three largest groups of enzymes in industry, with about two-thirds of whole enzymes utilized today (H. Cui, Yang, Wang, & Xian, 2015; J. D. Cui & Jia, 2015). The current study was conducted in the Southern South China Sea (SSCS) as a part of studies on bacterial diversity to add to the knowledge of Malaysian waters and is indeed part of the SSCS. That it is supposed to be the heart that links Eurasia with the Americas, as the largest shipping port in the world is situated here (Arai, 2014; Onuoha, Ismail, Ismail, & Mansor, 2016) This study aims to determine the distribution of bacterial proteolytic communities that exist in the South China Sea by isolating and identifying them. As well, marine bacteria that produce alkaline protease have been characterized using Biolog GenIII.

Methodology

Samples collection

Seawater and sediment samples were collected in sterile containers from four different stations in the South China Sea, located at Kuantan–Pahang–Malaysia. Seawater samples have been collected from different distances (400, 700, 1500, and 2000 meters) utilizing the Van Dorn water sampler, while the sediment has been collected using the Ekman dredge bottom sampler.

Physicochemical parameters

Hydrolab DS5 DataSonde was used for field observation of physicochemical parameters such as coordinates, temperature, pH, dissolved oxygen (DO), turbidity, salinity, and conductivity.

Bacteria isolation

To isolate the bacteria from seawater and sediment samples, 10 g of marine sediment was added to 20 mL of sdH_2O (Sterile distilled water) that were vortexed till it became homogeneous. After that, the samples were incubated at 37°C for 30 min using an orbital shaker (200 rpm) and were then centrifuged for 20 min at 5000 rpm. The supernatants were transferred to new centrifuge tubes, and from each supernatant, 1 mL was taken to conduct serial dilution. On the other hand, 10 mL of seawater was pipetted into a centrifuge tube, and just 1 ml of distilled water was transmitted into another tube containing 9 ml to perform serial dilution. Ultimately, serial dilutions (from 10-1 to 10-6) were prepared for both sediment and seawater samples (Jalal et al., 2010).

Screening of proteolytic ability

The proteolytic activities of all strains were assayed using skim milk agar plates. They were incubated for 24 to 48h at 37 °C, and enzyme activity was observed. Positive colonies degraded the casein in the milk (Padmapriya, Rajeswari, Nandita, & Raj, 2012).

Bacteria identification

The isolates were sent to **1st BASE Products and Services** for Full-Length 16S rRNA Sequencing. OmniLog® Data Collection, Biolog's Microbial Identification Systems program was used to identify the bacterium from its phenotypic pattern in the GEN III MicroPlate.

Protease Enzyme Production

A preparation of 2% Casein, 1% Dextrose, 1% Peptone, 2% KH_2PO_4, 0.2% NaCl2 and 0.002% $CaCl_2$ at pH 7.0 was used as protease enzyme source. The isolates have been inoculated in nutrient broth for 24h. 1% of inoculum was transferred in 250 ml conical flasks containing 50 ml of the enzyme production medium and incubated at 37°C for three days. Afterward, the supernatant was gathered and used as a crude enzyme after centrifugation at 10,000 rpm for 10 min (Prabakaran. V1, Soma Prabha. A2. And Blessy Thayalin, 2016).

Enzyme Assay

Protease activity was determined by the standard assay (V. Mardina, Yusof, & Alam, 2015) The reaction mixture contained 2.5 ml of casein (1%w/v, prepared in 50 mM of tris buffer, pH 8), and an aliquot of 0.5 was incubated in a 37°C water bath for 10 min. After that, 2.5 ml of 0.11M trichloroacetic acid was added to the solution to stop the reaction and can remain for 45 min at room temperature. 1ml of supernatant was obtained by centrifugation at 10,000xg for 10 min at four °C and used for color development, which was achieved by mixing 1 ml of supernatant with 2.5 ml of 0.5 M Na_2CO_3 and 0.5 ml of 0.1N Folin Ciocalteu's Phenol Reagent for 30 min. Eventually, the absorbance was read at 660nm against the blank sample. One enzyme activity unit was defined as the amount needed to release one µg of tyrosine per ml per min under assay conditions.

Results and Discussion

Sample collection

Table 1 represents the conditions of the physicochemical parameters of the four different stations, which sit at different distances (400, 700, 1500, and 2000 meters) that show Fig.1.

The highest value of salinity was 37.9 ppt that located in the station (3), whereas the lowest value was placed in the station (4), with 36.18 ppt. Changes in salinity levels can influence sea organisms. Salinity is one of the essential environmental components that affect the reproduction, growth, and dissemination of a variety of marine life forms (Kumlu & Jones, 1995). The aquatic water quality parameters such as temperature, dissolved oxygen, and conductivity can be affected by the salinity levels within the water (Mohamad Hamzah et al., 2020). The range of temperature at all stations was between 29 to 36.2°C. The ocean water temperature varies from 28°C to 32°C (Mohamad Hamzah et al., 2020), while (Bartram, Lynch, Stearns, Moreno-Hagelsieb, & Neufeld, 2011) indicate that the body of water retains temperature variations. Conductivity showed the lowest value (55.3 mS/cm) in the station (3) and the highest value (56.6 mS/cm) in the station (1). pH values of the four stations were almost similar and ranged from 8.05 to 8.1. The lowest value of dissolved oxygen (DO) was 4.05 mg/L in the station (2), which sited at 400 meters, while the highest value was in the station (4), with 4.86 mg/L. Indeed, the amount of dissolved oxygen in seawater is affected by many factors such as the atmospheric pressure, temperature, ion activity, the number of organisms utilizing oxygen for respiration, and the volume and velocity of the seawater (Jalal et al., 2010). Among the sampling station areas, station (2) was the most polluted. Perhaps, a high number of microorganism communities have existed at this station. Therefore, they have been used more dissolved oxygen compared to other stations. The presence of *Staphylococcus* at this station can also be explained that the domestic sewage run-off pathogenic bacteria present in huge quantities (Jalal et al., 2010). This was owing to dissolved oxygen (DO) necessary for the marine systems, growth, and existence of many marine organisms. UNESCO WHC* Reported that Seawater requires at least four mg/L of oxygen and, preferably, five mg/L of oxygen for a biological environment that functions at optimum levels for aquatic. Turbidity represents the combination of sand and xenobiotic compounds that have accumulated over decades. The highest turbidity value (16.4 NTU) was recorded in the station (4) at 2000m, while the lowest value (10.21 NTU) was in the station (2) at 400m from shore. Much of the time, this event would result in harmful effects on aquatic sediment.

These results demonstrate that the physicochemical parameters of coastal waters of the Southern South China Sea in the four different stations were insignificant, which revealed that the sea was well mixed. Similar to the finding recorded by (Schmidt, Seitz, Hassel, & Wolf, 2018). A significant association between salinity and conductivity for all stations is primarily caused by variations in temperature, dissolved oxygen, and conductivity. There was a connection between temperature and salinity. DO increases when the temperature and salinity decrease except for station (1). Those results were in line with (Sverdrup et al., 1942).

Isolation of Bacteria and Screening of its Ability to Produce Protease

In the present study, eighteen strains were isolated from eight different samples (sediments and seawater) from the South China Sea. However, only ten strains were found able to produce the protease enzyme by forming a transparent hydrolytic zone on skim milk agar, which could be owing to casein hydrolysis. This finding is similar to (Asha & Palaniswamy, 2018; H. Cui, Wang, & Yu, 2015; Fulzele et al., 2011). Simple and quick plate test used for primary inspection of protease production was very effective and successful; it enables a significant number of proteolytic colonies to be screened for a very short time (Singh, Singh, & Yadav, 2013). The colony morphology and Gram staining of the ten isolates have been examined. The cultural morphological and physiological characteristics of selected bacterial isolates are presented in Table (2) below.

Molecular characterization

The proteolytic strains were identified employing 16S rRNA sequencing. The sequences of seven isolates were reported in the GenBank database under accession numbers shown in Table 2 and then it has been matched with those available in the NCBI database. On the other hand, the sequencing findings indicate that samples 06 and 09 are mixed isolate samples. Therefore, the results cannot be used in the BLAST analysis. The Phylogenetic test revealed that *Bacillus genus* was found predominantly, the strains (ABN13, AD242, TB212, NID706) were *B. licheniformis, (those findings are similar to the results reported by (Vivi Mardina & Yusof,* *2016)*, other two strains (MD152 and ISD488) were identified as *Bacillus cereus (Abou-Elela, Ibrahim, Hassan, Abd-Elnaby, & El-Toukhy, 2011)*. While, KRF402 displayed a similarity to *Bacillus safensis* (Liu et al., 2013) with a similarity of 99% to strain (NBRC100820). The strain DK131 was identified as *Staphylococcus warneri*, *which was* found at St2, 400 meters from the shore. *This can be referred to* as the domestic waste discharges and the food industry by the coast *(Gunn, Keiser, & Colwell, 1983; Jalal et al., 2010)*.

Biolog GEN III MicroPlate Characterisation

In the biochemical test conducted by **Biolog GENIII MicroPlate,** positive reactions are indicated by forming a purple color due to the tetrazolium redox dye reduction.

The four *Bacillus cereus* strains are also positive to the following Amino-acids: Gelatine and L-Histidine, similar to IIUM6 and which are positive even to L-Glutamic Acid. Unlike sugar sources, these strains' positivity to Hexose-Acids is likely less, with all *B. cereus* strains positive only to D-Galacturonic Acid and to D-Gluconic Acid. The reaction with L-Lactic Acid, Acetoacetic Acid was positive for the four strains. Also, IIUM6 was positive for Methyl Pyruvate, where IIUM9 was positive for Methyl Pyruvate, Formic Acid, and acetic acid, the same as MD152. As an exception, ISD488 and IIUM6 were negative to Acetic Acid. The tolerance level of *Bacillus cereus* strains to pH was at pH6. All strains showed salt tolerance at 1 and 4% NaCl and 1% Sodium Lactate concentrations. They were positive to salt compounds D-Serine -except strain IIUM9-, Guanidine HCl, Lithium Chloride, Potassium Tellurite (except MD152), Aztreonam, and Sodium Butyrate. Additionally, MD152 had a higher salt tolerance concentration at 8% NaCl. However, IIUM9 and MD152 had no tolerance for D-Serine and Potassium Tellurite, respectively.

B.licheniformis -NID706 could assimilate Dextrin and D-trehalose only while *B. safensis*- KRF402 and B3 reacted to each of Dextrin, D-maltose, and sucrose in addition to D-turanose by *B. safensis*- KRF402 also. All *B.licheniformis* strains catabolized D-salicin and N-acetyl-D-glucosamine, where *B. safensis*-KRF402, *B.licheniformis*-ABN13, *B. licheniformis-AD242*, and *B. licheniformis* -NID706 showed positive reaction only with D-salicin, N-acetyl-D-glucosamine, N-acetyl-D-galactosamine, and β-methyl-D-glucoside, respectively. Both *B. safensis*- KRF402 and *B. licheniformis- AD242* reacted positively to D-serine and D-fructose. Additionally, *B. licheniformis- AD242* was also positive for D-fucose and inosine with *B. licheniformis* ABN13. However, *B. safensis*- KRF402 was alone capable of disassembling D-galactose and *B. licheniformis*-ABN13 to L-fucose. Furthermore, the results showed that bacteria *B. safensis*- KRF402 and B3 were able to break down D-sorbitol, D-mannitol, D-arabitol, Myo-inositol, glycerol, D-glucose-6-PO4, and D-fructose-6-PO4, except for *B.licheniformis*-ABN13, which was significant with D-serine, same as *B. licheniformis-AD242*, but ineffective with D-sorbitol. *B.licheniformis* -NID706, otherwise, reacted positively to D-glucose-6-PO4 and D-fructose-6-PO4 only. Moreover, gelatin, L-alanine, L-aspartic-acid, L-glutamic acid, and L-serine were catabolized by all strains when *B.licheniformis*-ABN13 was found positive with L-pyro-glutamic acid together with *B. safensis*- KRF402 and *B.licheniformis* -NID706, which, in turn, responded to L-histidine. D-saccharic acid, exceptionally, is consumed by *B. safensis*- KRF402, *B.licheniformis*-ABN13, and *B.licheniformis*-NID706. However, all strains are positive for pectin. *B.licheniformis*-ABN13 and *B.licheniformis*-NID706 responded positively to methyl pyruvate, citric acid, **α**-keto-glutaric acid, D-malic acid, L-malic acid, and Bromo-succinic acid. *B. licheniformis-AD242* was also positive but to L-lactic acid, **α**-keto-glutaric acid, and L-malic acid only.

Quantitative estimation of protease activity using crude cell

Figure 4 showed that with more than 33 U/ml, *B. cereus*-MD152 had the highest protease activity, followed by *B. licheniformis*-ABN13 with 29 U/ml. Both were in St1. In comparison, with no more than 13,5 U/ml isolated from St2, the lowest output was reported for *B.cereus-ISD488*. When *B. safensis*-KF402 showed a yield of 21 U/ml. (Singh et al., 2013) stated that *B. safensis* potentially secretes protease in its stationary phase.

Conclusion

In this study, the results show a negligible difference in the physicochemical parameters of seawater between the four different stations of the South China Sea, which have shown that the sea is well blended. Ten strains out of 18 isolates were able to produce protease enzyme to *Bacillus cereus, B. safensis, B. lichenoformis,* and *Staphylococcus warneri* based on the molecular identification of 16S rRNA gene and Biolog GEN III Microplate. Isolates of MD152 and ABN13 *B. cereus* and *B. lichenoformis*, respectively, were found to be the most promising proteolytic producers based on their quantitative enzyme production results.

The purpose of this research was to explain the connections between the physicochemical parameters and the bacterial communities that flourish in the Southern South China Sea. The knowledge of bacterial diversity gives us a profound impression of the potential behavior of the microbe. However, the results do not reveal any signs of serious pollution.

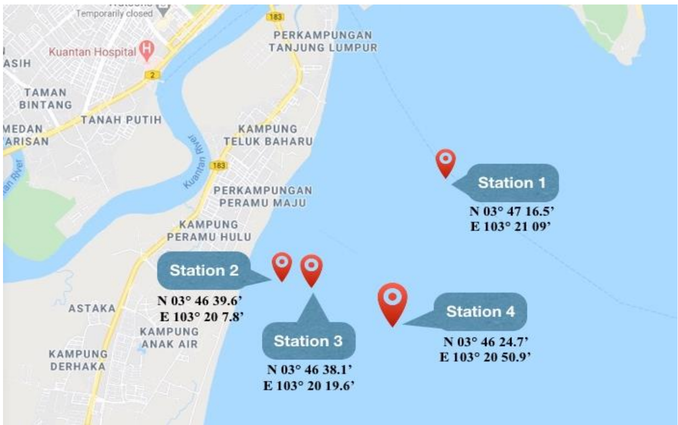

Figure 1: South China Sea and Its Designated Sampling Area.
(adapted from Google-Map © data 2020).

Figure 2: Degradation Of Skim Milk Agar Plates by Different Marine Bacteria.
Bacterial strains producing protease indicated by the formation of clearance zones around the bacterial colonies.

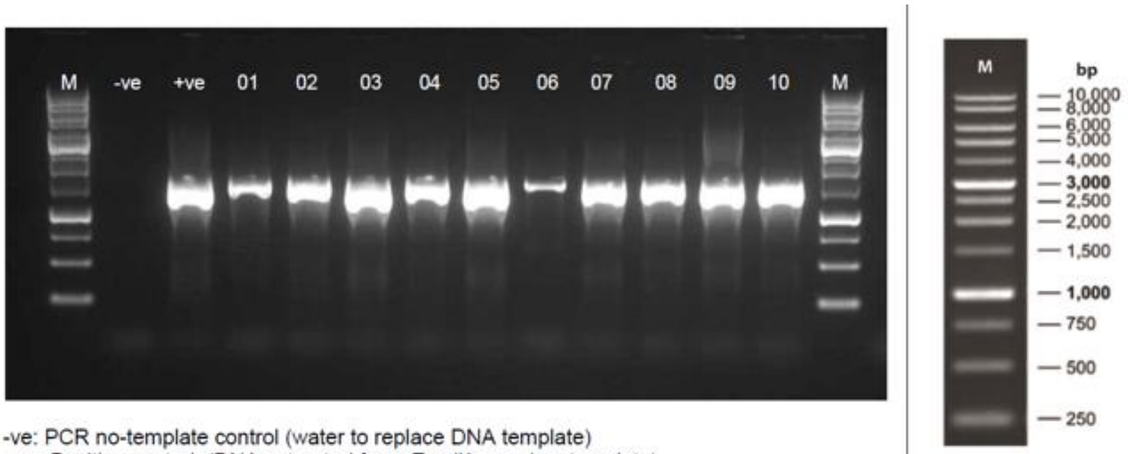

-ve: PCR no-template control (water to replace DNA template)
+ve: Positive control (DNA extracted from *E.coli* is used as template)

Figure 3: Agarose Gel Electrophoresis for 10 Isolates Producing Protease.

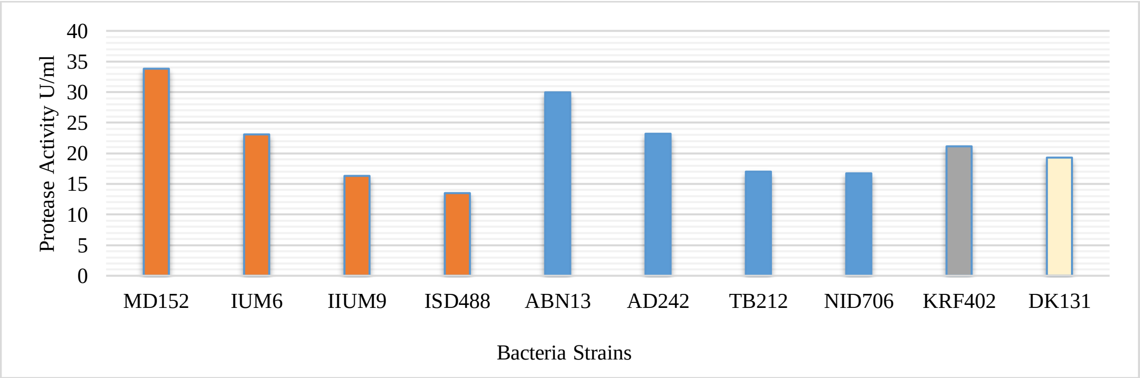

Figure 4: Protease Production For 10 Isolates.

🟧 *Bacillus cereus,* 🟦 *Bacillus lichenoformis,* ⬛ *Bacillus safensis,* ⬜ *Staphylococcus warneri*

Table 1: Physicochemical Parameters Conditions of The Different Four Stations.

Stations	Coordinates	Temperature (C°)	conductivity (mS/cm)	pH	Salinity (ppt)	Turbidity (NTU)	DO (mg/L)	Distance (Meter)
Station (1)	N 03° 47 16.5 E 103° 21 09	29	56.6	8.1	37.9	14.2	4.53	1500
Station (2)	N 03°46 39.6 E 103° 20 7.8	36.2	56.4	8.04	37.78	10.21	4.05	400
Station (3)	N 03° 46 38.1 E 103° 20 19.6	32.6	55.3	8.05	37.24	12.32	4.33	700
Station (4)	N 03° 46 24.7 E 103° 20 50.9	30.04	55	8.07	36.18	16.4	4.86	2000

Table 2: Morphological Characteristics, Accession Numbers and Names of Identified Isolates.

Bacteria	N°	Strain name	Accession number	Source	Station	Protease activity U/ml	Morphological characteristics
Bacillus cereus	01	MD152	**MT642947**	S	St3	33.82	Gram-positive bacteria with creamy white colonies, glistening, translucent, small, circular, raised. Some are irregular.
	06	IIUM6	---	S	St2	23.09	
	09	IIUM9	---	S	St1	16.31	
	10	ISD488	---	S	St4	13.50	
Bacillus licheniformis	04	ABN13	**MT642943**	W	St3	29.96	Gram-positive bacteria Circular white small colonies, dull and glistening. Earlier, the colonies got bigger, dry, dull, and filamentous. They are firmly adhered to the agar.
	05	AD242	**MT642944**	S	St4	23.2	
	07	TB212	**MT642945**	W	St1	17.01	
	08	NID706	**MT642946**	S	St1	16.73	
Bacillus safensis	02	KRF402	**MT642941**	S	St4	21.14	Gram-positive, raised colonies. with irregular margins
Staphylococcus warneri	03	DK131	**MT642942**	W	St2	19.30	Gram-positive bacteria. Very small circular beige to yellowish colonies, glistening and raised.

Acknowledgement

The authors are grateful to the Department of Biotechnology Engineering, Faculty of Engineering, International Islamic University Malaysia to carry out this study.

References

Abou-Elela, G. M., Ibrahim, H. A. H., Hassan, S. W., Abd-Elnaby, H., & El-Toukhy, N. M. K. (2011). Alkaline protease production by alkaliphilic marine bacteria isolated from Marsa-Matrouh (Egypt) with special emphasis on Bacillus cereus purified protease. *African Journal of Biotechnology*, *10*(22), 4631–4642. https://doi.org/10.5897/AJB10.2111

Alavandi, S. (1990). Relationship between heterotrophic bacteria and suspended particulate matter in the Arabian Sea. *Indian Journal of Marine Sciences*, *30*(I), 89–92.

Arai, T. (2014). Diversity and conservation of coral reef fishes in the Malaysian South China Sea. *Reviews in Fish Biology and Fisheries*, *25*(1), 85–101. https://doi.org/10.1007/s11160-014-9371-9

Asha, B., & Palaniswamy, M. (2018). Optimization of alkaline protease production by Bacillus cereus FT 1 isolated from soil. *Journal of Applied Pharmaceutical Science*, *8*(2), 119–127. https://doi.org/10.7324/JAPS.2018.8219

Bartram, A. K., Lynch, M. D. J., Stearns, J. C., Moreno-Hagelsieb, G., & Neufeld, J. D. (2011). Generation of multimillion-sequence 16S rRNA gene libraries from complex microbial communities by assembling paired-end Illumina reads. *Applied and Environmental Microbiology*, *77*(11), 3846–3852. https://doi.org/10.1128/AEM.02772-10

Caron, D. A., Worden, A. Z., Countway, P. D., Demir, E., & Heidelberg, K. B. (2009). Protists are microbes too: A perspective. *ISME Journal*, *3*(1), 4–12. https://doi.org/10.1038/ismej.2008.101

Chi Z, Liu ZQ. (2005). Marine yeasts and their applications in mariculture. *Collection Studys Nat Conf High Tech Marine Biotechnol*, (3) 243–247.

Cui, H., Wang, L., & Yu, Y. (2015). Production and characterization of alkaline protease from a high yielding and moderately halophilic strain of SD11 marine bacteria. *Journal of Chemistry*, *2015*. https://doi.org/10.1155/2015/798304

Cui, H., Yang, M., Wang, L., & Xian, C. J. (2015). Identification of a new marine bacterial strain SD8 and optimization of its culture conditions for producing alkaline protease. *PLoS ONE*, *10*(12), 1–13. https://doi.org/10.1371/journal.pone.0146067

Cui, J. D., & Jia, S. R. (2015). Optimization protocols and improved strategies of cross-linked enzyme aggregates technology: Current development and future challenges. *Critical Reviews in Biotechnology*, *35*(1), 15–28. https://doi.org/10.3109/07388551.2013.795516

de Pascale, D., De Santi, C., Fu, J., & Landfald, B. (2012). The microbial diversity of Polar environments is a fertile ground for bioprospecting. *Marine Genomics*, *8*, 15–22. https://doi.org/10.1016/j.margen.2012.04.004

Faulkner, D. J. (2001). Marine natural products. *Natural Product Reports*, *18*(1), 1–49. https://doi.org/10.1039/b006897g

Fulzele, R., Desa, E., Yadav, A., Shouche, Y., & Bhadekar, R. (2011). Characterization of novel extracellular protease produced by marine bacterial isolate from the Indian Ocean. *Brazilian Journal of Microbiology*, *42*(4), 1364–1373. https://doi.org/10.1590/S1517-83822011000400018

Gunn, B. A., Keiser, J. F., & Colwell, R. R. (1983). Numerical taxonomy of staphylococci isolated from clinical sources. *International Journal of Systematic Bacteriology*, *33*(4), 738–750. https://doi.org/10.1099/00207713-33-4-738

Haefner, B. (2003). Drugs from the deep: Marine natural products as drug candidates. *Drug Discovery Today*, *8*(12), 536–544. https://doi.org/10.1016/S1359-6446(03)02713-2

Hahn, M. W. (2006). The microbial diversity of inland waters. *Current Opinion in Biotechnology*, *17*(3), 256–261. https://doi.org/10.1016/j.copbio.2006.05.006

Jalal, K. C. A., Kamaruzzam, Y., Fairuz, A., Akbar, B., Shahbudin, S., & Faridah, Y. (2010). Bacterial Communities in Kuantan Estuary of Pahang Malaysia. *Journal of Applied Sciences*, *10*(8), 652–657. https://doi.org/10.3923/jas.2010.652.657

Kennedy, J., O'Leary, N. D., Kiran, G. S., Morrissey, J. P., O'Gara, F., Selvin, J., & Dobson, A. D. W. (2011). Functional metagenomic strategies for the discovery of novel enzymes and biosurfactants with biotechnological applications from marine ecosystems. *Journal of Applied Microbiology*, *111*(4), 787–799. https://doi.org/10.1111/j.1365-2672.2011.05106.x

Kumlu, M., & Jones, D. A. (1995). Salinity tolerance of hatchery-reared postlarvae of Penaeus indicus H. Milne Edwards originating from India. *Aquaculture*, *130*(2–3), 287–296. https://doi.org/10.1016/0044-8486(94)00319-J

Liu, Y., Lai, Q., Dong, C., Sun, F., Wang, L., Li, G., & Shao, Z. (2013). Phylogenetic Diversity of the Bacillus pumilus Group and the Marine Ecotype Revealed by Multilocus Sequence Analysis. *PLoS ONE*, *8*(11), e80097. https://doi.org/10.1371/journal.pone.0080097

Mardina, V., Yusof, F., & Alam, M. Z. (2015). Statistical optimization of physicochemical factors for protease production by bacillus licheniformis on skim latex serum fortified media. *Journal of Engineering Science and Technology*, *10*(Spec.issue6), 42–52.

Mardina, Vivi, & Yusof, F. (2016). Purification and Characterization of Surfactant-Stable Protease from Bacillus Licheniformis: A Potential Additive for Laundry Detergent. *International Journal of Advanced Biotechnology and Research*, *7*(2), 976–2612. Retrieved from http://www.bipublication.com

Mohamad Hamzah, F., Mohammed, S. N. S., Syed Abdullah, S. M., Abdul Maulud, K. N., Mohd Razali, S. F., & Kamarudin, M. K. A. (2020). The effect of marine parameters on salinity via statistical approaches. *Journal of Physics: Conference Series*, *1489*(1). Institute of Physics Publishing. https://doi.org/10.1088/1742-6596/1489/1/012035

Nigam, P. S. (2013). Microbial enzymes with special characteristics for biotechnological applications. *Biomolecules*, *3*(3), 597–611. https://doi.org/10.3390/biom3030597

Nurullah, A. (2012). High level production of extracellular protease from Bacillus licheniformis ATCC 12759 in submerged fermentation. *Research Journal of Biotechnology*, *7*(3), 46–51. https://doi.org/10.5897/AJB11.2183

Onuoha, M. D. U., Ismail, I., Ismail, A. S., & Mansor, M. F. (2016). Experimental determination of flow patterns and water holdup of low viscosity oil-water system in horizontal pipes. *Sains Malaysiana*, *45*(11), 1635–1640.

Padmapriya, B., Rajeswari, T., Nandita, R., & Raj, F. (2012). Production and purification of alkaline serine protease from marine Bacillus species and its application in detergent industry. *European Journal of Applied Sciences*, *4*(1), 21–26.

Prabakaran. V1, Soma Prabha. A2. And Blessy Thayalin, T. S. (2016). Screening, Production and Industrial Application of Protease Enzyme From Marine Bacteria. *International Journal of Current Microbiology and Applied Sciences*, *5*(7), 863–874. https://doi.org/10.20546/ijcmas.2016.507.099

Prabavathy, V. R., Mathivanan, N., & Murugesan, K. (2006). Control of blast and sheath blight diseases of rice using antifungal metabolites produced by Streptomyces sp. PM5. *Biological Control*, *39*(3), 313–319. https://doi.org/10.1016/j.biocontrol.2006.07.011

Reddy, L. V. A., Wee, Y. J., Yun, J. S., & Ryu, H. W. (2008). Optimization of alkaline protease production by batch culture of Bacillus sp. RKY3 through Plackett-Burman and response surface methodological approaches. *Bioresource Technology*, *99*(7), 2242–2249. https://doi.org/10.1016/j.biortech.2007.05.006

Schmidt, H., Seitz, S., Hassel, E., & Wolf, H. (2018). The density–salinity relation of standard seawater. *Ocean Science*, *14*(1), 15–40. https://doi.org/10.5194/os-14-15-2018

Singh, R. S., Singh, R. P., & Yadav, M. (2013). Molecular and biochemical characterization of a new endoinulinase producing bacterial strain of Bacillus safensis AS-08. *Biologia (Poland)*, *68*(6), 1028–1033. https://doi.org/10.2478/s11756-013-0259-2

Sverdrup, H. U., Johnson, M. W., & Fleming, R. H. (1942). "The Oceans". 1087 pp. Prentice-Hall Inc., New York.

UEPA (United States Environmental Protection Agency) (2006). Marine ecosystems. http://www.epa.gov/bioiweb1/aquatic/marine.html.

UNESCO WHC*: Anon UNESCO World Heritage Centre - New Inscribed Properties (1978)

**International Research Conference on Applied Sciences
and Engineering 2020 (IRCASE 2020)
eISBN 978-967-2426-20-2
13th – 14th December 2020**

INTERACTION AND OPTIMIZATION OF MACHINE PARAMETER TOWARDS MECHANICAL PROPERTIES OF NEW COMPOSED COMPOSITE: DYNAGLASS PPG3637

**Nur Syamimi Rusli[1*]
Izyan Dayana Jonid[2]**

[1]Electrical Engineering Department, Politeknik Port Dickson, Malaysia, (E-mail: syamimi@polipd.edu.my)
[2]Mechanical Engineering Department, Politeknik Muadzam Shah, Malaysia, (E-mail: izyan@pms.edu.my)

Abstract: *This study reveals the interaction and optimization of machine parameter towards mechanical properties of new composed composite. The new composed composite is polypropylene reinforced with fiber glass composite. Injection molding machine is utilized in this study. The processing parameters involved on the experimental are melting temperature (MeT) (250°C – 280°C, injection pressure (IP) (22 MPa – 28 MPa) and cooling time (Ct) (60s – 90s). The optimum processing parameters value that gives highest tensile strength, highest tensile modulus and shortest elongation were studied. From the result analysis, it is found that the injection pressure is the most significant parameter that affected tensile strength and percentage of elongation. Meanwhile, melting temperature shows the most significant parameter affected on the tensile modulus. The optimum parameters affected the tensile strength are 250°C for MeT, 22 MPa for IP and 77.97s for Ct. Further, optimum parameters affected the tensile modulus are 262.4°C for MeT, 27.0 MPa for IP and 60s for Ct. Finally, optimum parameters affected the percentage of elongation are 250°C for MeT, 28 MPa for IP and 90s for Ct.*

Keywords: *(Interaction, Optimization, Machine Parameter, Mechanical Properties)*

Introduction

There is very competitive production of composite material based on polypropylene (PP) and fiber glass. Due to low cost, flexible processability, high abundance and recyclability justify their use in a wide range of application, mostly in automotive industry. Polypropylene (PP) is one of the most commonly thermoplastic polymers used in a wide variety of application worldwide. In general, PP offers a good balance of properties and cost unachieved by most thermoplastics. It is lightweight yet stronger in such high flexural strength due to its semi-crystalline nature and has good impact strength. Meanwhile, fiber glass is the most commonly used fiber to reinforce thermoset and thermoplastic resins across a wide variety of applications and processes. Glass reinforcements in which added or molded with other materials, help improve the surface aspect as it allows a uniform impregnation (with resins) and are not subject to cracking, breaking or splitting. It has a greater specific resistance in such higher tensile strength compared to steel. This characteristic is the primary reason for the use of glass strand in the production of high-performance composites. Injection molding machine is one of the most commonly used methods of producing plastic product in high volumes due to its ability to fast production and highly efficient.

Thus, this study investigates the interaction and optimization of the injection molding machine parameter such as melting temperature, injection time and cooling time towards mechanical properties such as tensile strength, tensile Young’s modulus and the percentage elongation of composite PP with fiber glass type PPG 3637 using response surface method.

Problem Statement

Many plastic injection molding companies having problem to setting injection molding optimum parameters during the production run especially for new mold and new plastic materials are introduced. Application of design of experiment (DOE) becomes more essential in optimization parameters. Therefore, trial and error practice in industry can be replaced by using systematical approach. One of DOE method is using response surface method (RSM). RSM is statistical method that uses quantitative data from appropriate experiments in order to determine and simultaneously solve multivariant equations. RSM is useful for the modeling and analysis of programs in which a response of interest is influenced by several variables and the objective is to optimize this response. Therefore by using RSM, the optimum factor of the machine parameter can be identified towards tensile strength, tensile Young's modulus and the elongation of composite PP with fiber glass.

Objective of the study

i. To determine the interaction of process parameters on tensile strength, tensile modulus and percentage of composite PP with fiber glass type PPG 3637
ii. To optimize machine parameter that related to the tensile strength, tensile Young's modulus and the elongation of the composite PP with fiber glass type PPG 3637 using single and multiple objective optimizations.

Literature Review

Properties of Polypropylene Reinforced with Fiber Glass

Polypropylene (PP) is one of the fastest growing polymers today. The glass fiber reinforced PP is used in a variety of applications such as building construction, marine, automotive industries and others. According to Harutun, (2003) the main advantages of glass fiber reinforced PP over the other engineering plastics are low cost and low specific gravity. In response to Harutun, (2003), Maria et al. 2004 added that PP filled with particulate fillers will improve the hardness and modulus. High particle loadings result in products with much higher weight than that of the pure polymers. Hence a composite with improved properties at low particle concentration is always the optimum choice. A research has been conducted by Sinto (2009) PP reinforced with short glass fiber was modified with precipitated nanosilica by using melt mixing method. The study found that the amount of the glass fiber required for a particular modulus could be reduced by the addition of nanosilica. This is due to the hydrophobic nature of polypropylene, which limits its adhesion to the 'hydrophilic' filler. The problem has been overcome by tailoring the affinity between the inorganic material and the organic polymer by in-situ polymerization, employment of coupling agents and other strategies. Such modifications have shown improvement in mechanical properties.

On the other hand, (Azuddin, 2017), conducted a study on fiberglass reinforced polypropylenes (PP) with various glass fiber percentage. The study commenced with the fabrication of micro tensile specimens at three different injection temperatures which is 260°C, 270°C and 280°C for different percentage by weight of fiberglass reinforced PP. It was found that 20% fiberglass reinforced PP possessed the greatest percentage increase of tensile strength with increasing temperatures.

In similar with Izzudin et al. 2017 and Ota, (2005) investigate the study on the combined effect of injection temperature and fiber content on the properties of polypropylene-glass fiber composites. The study focuses on correlations between physical and mechanical properties of PP and PP reinforced with glass fiber molded at different injection temperatures and fiber weight fractions (20% and 30%). The result from the experiment shows that the melting flow index (MFI) of the composites was dependent on fiber content, fiber length distributions, a slight additional thermal protection due to the fibers and PP chain scission. Besides, the finding from the experiment shows that tensile strength and elastic modulus of the PP composites increased linearly with fiber content. In addition, the other outcome from the research reveals that the injection temperature can decrease elastic modulus to a point that the different composites showed statistically comparable rigidities.

Injection Molding

Injection Molding is a type of manufacturing process that produce parts in large volume. It is typically used in almost across mass-production processes where the same part is being created in high repeatability with a good succession rates. According to Gurjeet Singha, (2017) most thermoplastic polymers can be processed by injection molding process. Over 30% of all the plastic parts are manufactured by the injection molding process (Mathivanan, 2010). This is one of the process that are greatly preferred in manufacturing industry because it can produce complex-shape plastic products and having good dimensional accuracy with short cycle times typical examples are automobile industry, casings and housings of products such as computer monitor, mobile phone and which has a thin shell feature (Gurjeet Singha, 2017). Injection molding is also used to produce daily routine items such as toothbrushes or small plastic toys. Many medical devices, including valves and syringes, are manufactured using injection molding as well.

Many studies and researches have been conducted in order to find the appropriate parameter of injection molding machine. (Ozcelik, 2016) considers the melt temperature, packing time, cooling time, and injection pressure as the parameter in order to examine mechanical properties of material using Taguchi method. In addition (Liu, 2004) conducted an experiment of the manufacturing of thermoplastic composites with the help of injection-molding technology. They study injection molding condition by process parameter water pressure, water temperature, water injection delay time, melt temperature, mold temperature and hold time with the help of Taguchi method.The proper injection capacity in the injection unit is found that shot weight of 70 to 80% of the injection capacity. This is due to at the side where the capacity is small, plasticizing time and injection time become long, and it is used at the narrow capacity of the molding machine. That is, the filling shortage is caused due to the extension of molding cycle and slow filling rate. On the other hand, at the side where the capacity is large, dwell time of the resin inside the cylinder becomes long, and the resin thermally decomposes.

Response Surface Methodology

Response surface methodology is a set of mathematical techniques that describe the relation between several independent variables and one or more responses (Anna et al. 2014). Research surface method was developed by Box and Wilson (1951) and since then it has been widely used as a technique for designing experiments. According to Montgomery, (2002) defined response surface methodology (RSM) as a collection of statistical and mathematical techniques useful for developing, improving, and optimizing processes.

The crucial applications of RSM are in the particular situations where there are several input variables that potentially influence some performance measure or quality characteristic of the process. The response is related to performance measure or quality characteristic. In general, the input variables are called independent variables, and are subject to the control of the researchers. Finding from Montgomery, (2002) indicates that the field of response surface methodology consists of the experimental strategy for exploring the space of the process or independent variables, empirical statistical modeling to develop an appropriate approximating relationship between the yield and the process variables, and optimization methods for finding the values of the process variables that produce desirable values of the response. In similar with Douglas, (2005) he defined that RSM is a collection of mathematical and statistical techniques for empirical model building, in which a response of interest is influenced by several variables and the objective is to optimize this response.

One of the main objectives of RSM is the determination of the optimum settings of the control variables that result in a maximum (or a minimum) response over a certain region of interest R (Akbarian, 2014). This method requires having a ‘good’ fitting model that provides an adequate representation of the mean response because such a model is to be utilized to determine the value of the optimum. Optimization techniques used in RSM depend on the nature of the fitted model.

For first-degree models, the method of steepest ascent is a viable technique for sequentially moving toward the optimum response. Khuri, (1979) developed certain improvements regarding the stopping rule used in the execution of this method. The first-degree model is usually used at the preliminary stage of a response surface investigation. Second-degree models are used after a series of experiments have been sequentially carried out leading up to a region that is believed to contain the location of the optimum response (Siuli, 2010).

In general second factorial design is often used to fit linear and non-linear (second order) response surface models for some number of input variables. Meanwhile experimental designs for first-order models such as factorial designs can be used when the data set does not present curvature. On the other hand, the experimental designs for quadratic response surfaces should be used, such as three- level factorial, Box–Behnken, central composite, and Doehlert designs (Bezerra et al., 2008).

Methodology

Introduction

The overall process flow throughout the experimental work is explained in the Figure 3.1 below. At initial stage of the study, the data were collected from the experimental procedure. Next the data acquired was consumed in Design Expert software in order to achieve the optimization. The method used in Design Expert is Response Surface Methodology (RSM) particularly using Box–Behnken design. Then the analysis of variance can be done by ANOVA. Hence the optimization achieved.

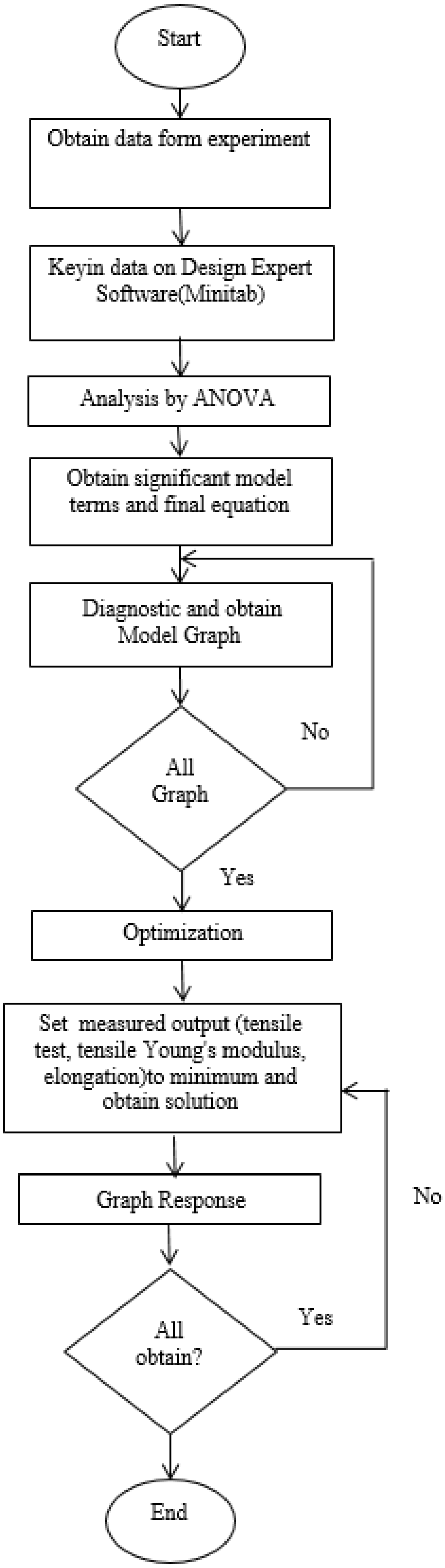

Figure 3.1: The Overall Process Flow Throughout the Experimental Work

At initial stage of the study, the data were collected from the experimental procedure. Next the data acquired was consumed in Design Expert software (*Minitab*) in order to achieve the optimization. The method used in Design Expert is Response Surface Methodology (RSM) particularly using Box–Behnken design. Then the analysis of variance can be done by ANOVA. Hence the optimization is achieved.

Methodology

RSM is suggested as a standard procedure for optimizing any process parameters. This study is planned to use Response Surface Methodology (RSM) particularly using Box–Behnken design. In general, Box–Behnken developed a 3-level incomplete factorial design as an alternative to the labour extensive full factorial design. The steps involved in Box–Behnken:

1. Define the independent input variables (material melting temperature, injection pressure, cooling time)
2. Adopting the Box–Behnken design to plan the experimental design.
3. Performed the experiments according to Box–Behnken design matrix. Experiment matrices are built by means of two level factorial designs (+1(high), -1(low)) with incomplete block designs.
4. The final matrix is completed with several replications of the central point, what improves precision. There are no experimental points in this design, where all factors have extreme values. This feature might be beneficial in experiments where undesired phenomena might occur in extreme conditions.
5. Perform the regression analysis with the quadratic model response.
6. Carry out the statistical analysis.
7. Obtain the optimal design parameters for the desired output.
8. Conduct the confirmation to verify the optimal design parameter settings.

Materials

PP reinforced with constant fiber glass contents; type DYNAGLASS PPG3637 that appears in black granule was used in the study. Figure 3.2 shows the PP reinforced with 20% fiber glass type DYNAGLASS PPG3637 used during experimental work.

Figure 3.2: Composite PP Reinforced With 20% Fiber Glass DYNAGLASS PPG3637

The composed composite has heat stability up to 280°C, while the molding temperature is between 190-210°C. Table 3.1 shows the characteristic of PP reinforced with fiber glass.

Table 3.1: The characteristic of PP reinforced with fiber glass DYNAGLASS PPG3637

Characteristic	Value
Glass fiber content	20%
Heat stability	280 °C
Drying temperature	80° C/ 2 hours
Molding temperature	190-210 ° C

Experimental plan and procedure

Selection of Process Parameters And Level

For the experimental work, the three process parameter each at two level have been decided. It is desirable to have two level of process parameters to reflect the actual behavior of the measured output parameter. The process parameters are named as factors and they are located in the adjacent column. The level of the individual process parameters or factors are given in Table 3.2. PP reinforced with constant 20% glass fiber contents is processed by using different combination of processing parameter at different combinations of material melting temperature, injection pressure and mold cooling time.

Table 3.2: The Level Of The Individual Process Parameter

Parameter	Level Low	Level High
Melting Temperature,(MeT) (°C)	250	280
Injection Pressure,(IP) (MPa)	22	28
Cooling time, (Ct)(s)	60	90

As per experimental design (Box-Behken), a set of two levels assigned to each process parameter. The matrix is completed with five replications of the central point, in order to improve precision. Hence the final matrix comprised of 17 runs as per Table 3.3.

Table 3.3: The Experimental Plan Using BB Design

No. of experiment	Melting Temperature, (°C)	Injection Pressure,(MPa)	Cooling time, (s)
1	250	22	75
2	280	22	75
3	250	28	75
4	280	28	75
5	250	25	60
6	280	25	60
7	250	25	90
8	280	25	90
9	265	22	60
10	265	28	60
11	265	22	90
12	265	28	90
13	265	25	75
14	265	25	75
15	265	25	75
16	265	25	75
17	265	25	75

Injection Molding Machine

In this experiment, PP reinforced with fiber glass, type DYNAGLASS PPG3637 used. A series of experiment were conducted using an injection molding machine model Arburg 420C 800-250 as shown in Figure 3.3.

Figure 3.3: Injection Molding Machine Used In The Experimental Work.

PP reinforced with glass fiber contents is processed by using different combination of processing parameter, material melting temperature, injection pressure and mold cooling time. Table 3.4 shows the capabilities of the injection molding machine used in the experimental work.

Table 3.4: The Capabilities Of The Injection Molding Machine

Parameter	Value
Maximum injection pressure (MPa)	180
Maximum injection rate (cm^3/s)	5000
Maximum clamping force (tonne)	7000

Mechanical Testing

The mechanical properties of all specimens is tested by using universal testing machine as per Figure 3.4. The universal testing machine is supported by electro- mechanical or hydraulic system. The system is equipped with the suitable specimen grips, an extensometer and with software capable of strain rate control and recording stress-strain data.

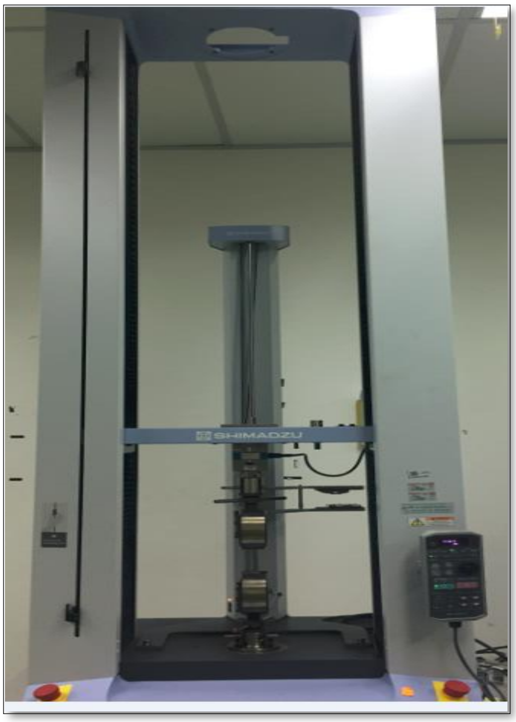

Figure 3.4: The Universal Testing Machine Used During Experimental Work

Data analysis and Discussion

Interaction Machine Parameter On Tensile Strength

Figure 4.1 and 4.2 show the contour plot relationship between MeT, IP and Ct towards the tensile strength. While, Figure 4.3 and 4.4 and shows the 3D plot of relationship between MeT, IP and Ct with respect to the tensile strength. From Figure 4.1 it shows that the highest tensile strength is achieved when both MeT and IP at the lowest value. The contour plot from Figure 4.2 indicates the highest tensile strength is attained at certain range value of Ct.

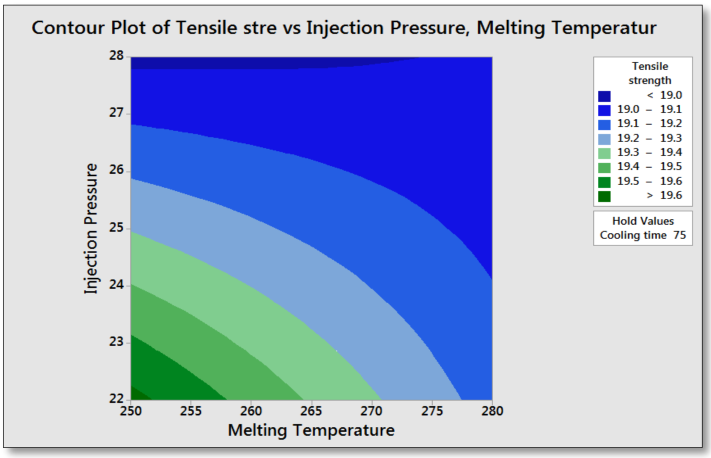

Figure 4.1: Contour Plot Of Tensile Strength vs IP, MeT

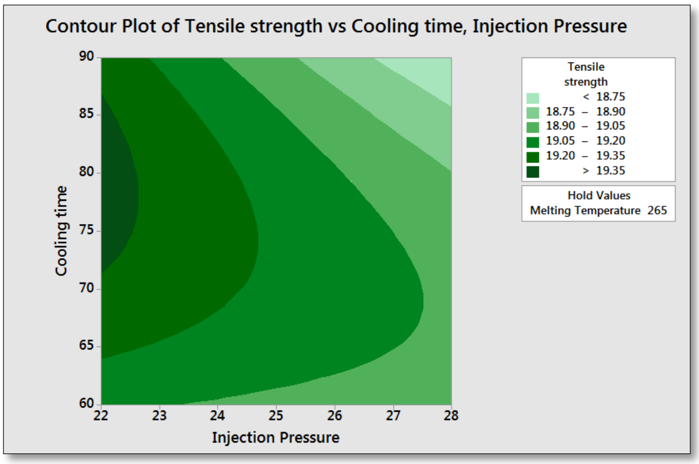

Figure 4.2: Contour Plot Of Tensile Strength vs IP, Ct

The highest tensile strength occurred when the value of Ct is between 70 seconds to 85 seconds and when the IP at the lowest value (22MPa).

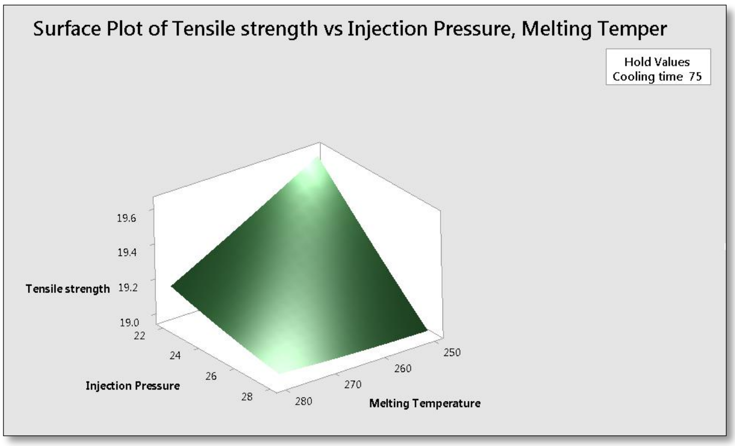

Figure 4.3: Surface Plot Of Tensile Strength vs IP, MeT

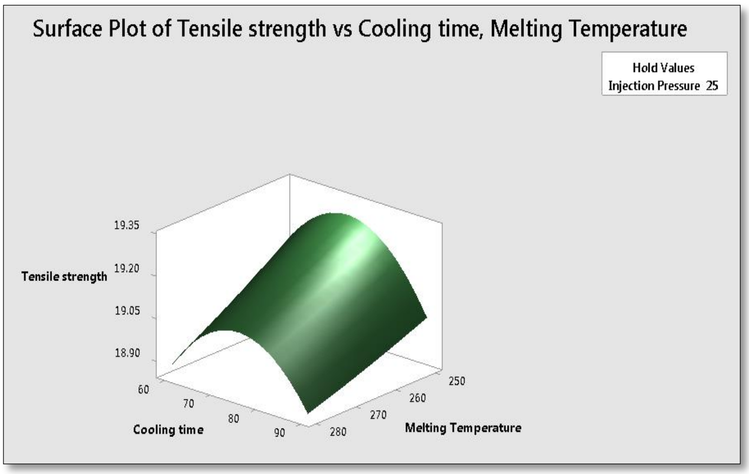

Figure 4.4 : Surface Plot of Tensile Strength vs Ct, MeT

From Figure 4.3, it displays the combination of low IP and high MeT contribute towards highest value of tensile strength. Meanwhile, surface Plot of tensile strength vs Ct, MeT in Figure 4.4 shows that interaction of mid-range value of Ct and low IP towards highest value of tensile strength.

Interaction Machine Parameter On Tensile Modulus

Figure 4.6 and 4.7 show the contour plot relationship between MeT, IP and Ct towards the tensile modulus. While, Figure 4.8 and 4.9 and shows the 3D plot of relationship between MeT, IP and Ct with respect to the tensile modulus. From Figure 4.6 it shows that the highest tensile modulus is achieved at certain range value of MeT and IP, which is the value of MeT from 235°C to 275°C and IP from value 23MPa to 28 MPa. The contour plot from Figure 4.7 indicate the highest tensile modulus is attained significantly at both highest and lowest value of Ct together with certain range value of IP. The highest tensile strength occurred at two conditions. First, when the value of Ct at the lowest value: 60 seconds and the value of IP is between 25 MPa to 28 MPa. Next the highest tensile modulus is achieved when the Ct is 90 seconds and the value of IP is in between 23 MPa to 26 MPa.

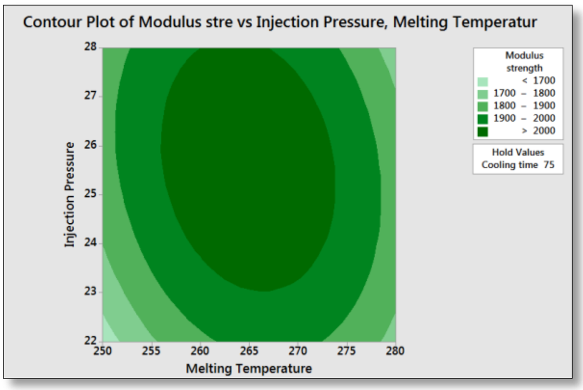

Figure 4.6: Contour Plot Of Tensile Modulus vs IP, MeT

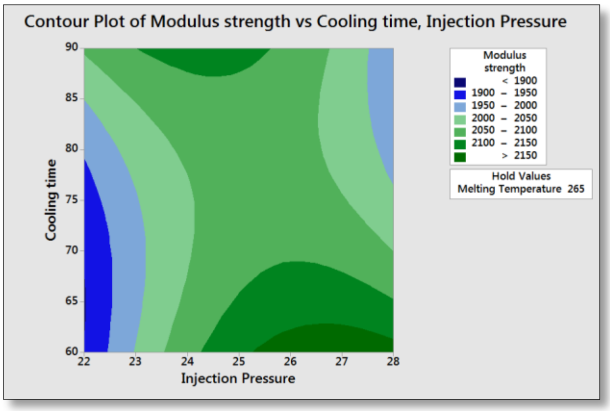

Figure 4.7: Contour Plot Of Tensile Modulus vs IP, Ct

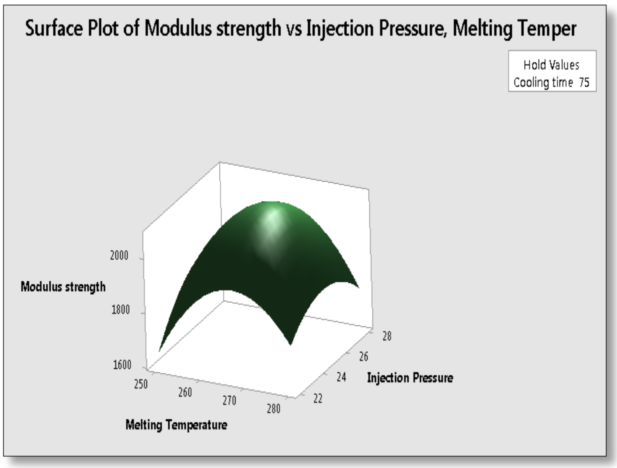

Figure 4.8: Surface Plot Tensile Modulus vs IP, MeT

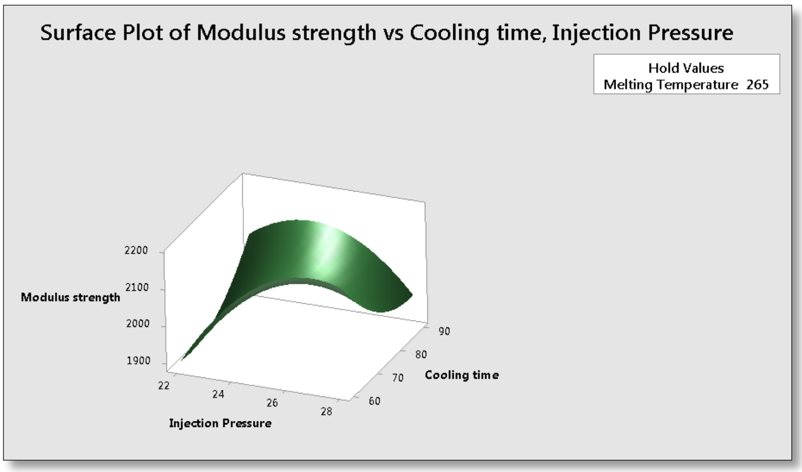

Figure 4.9: Surface Plot of Tensile Modulus vs Ct, IP

From Figure 4.8, it displays the combination of both mid-range value of IP and MeT contribute towards highest value of tensile modulus. Meanwhile, surface Plot of tensile modulus vs Ct and IP in Figure 4.9 shows that interaction of lowest and highest value of Ct and mid-range value of IP towards highest value of tensile modulus.

Interaction parameter on Elongation

Figure 4.10, 4.11 and 4.12 shows the contour plot relationship between MeT, IP and Ct towards the elongation. While, Figure 4.13, 4.14 and 4.15 and shows the 3D plot of relationship between MeT, IP and Ct with respect to the elongation. The contour plot from Figure 4.10 indicate the highest elongation is attained significantly at both highest and lowest value of Ct together with certain range value of IP. Figure 4.13, 4.14 and 4.15 displays the combination surface plot of elongation vs MeT, Ct and IP.

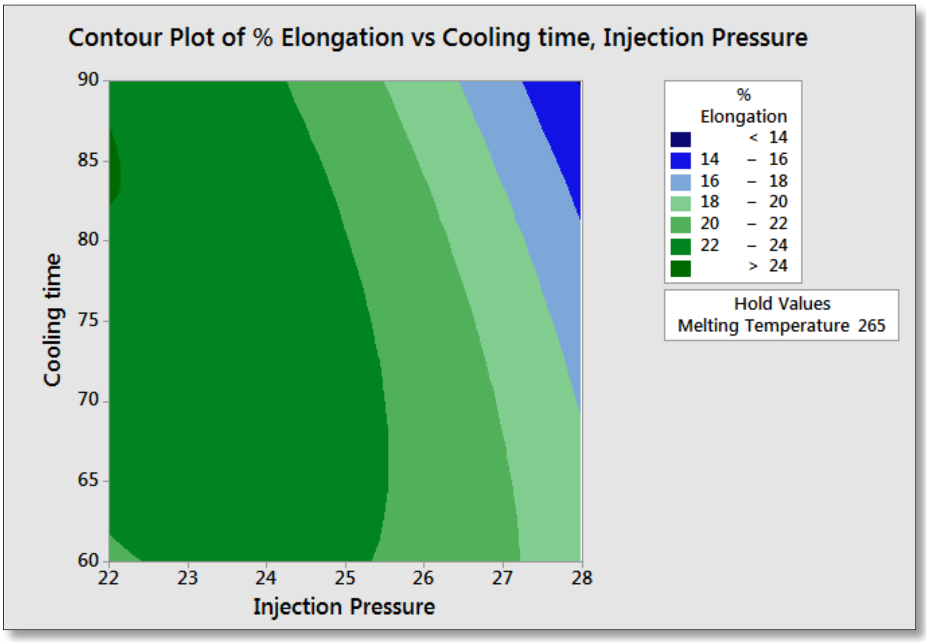

Figure 4.10: Contour Plot of Elongation vs IP, Ct

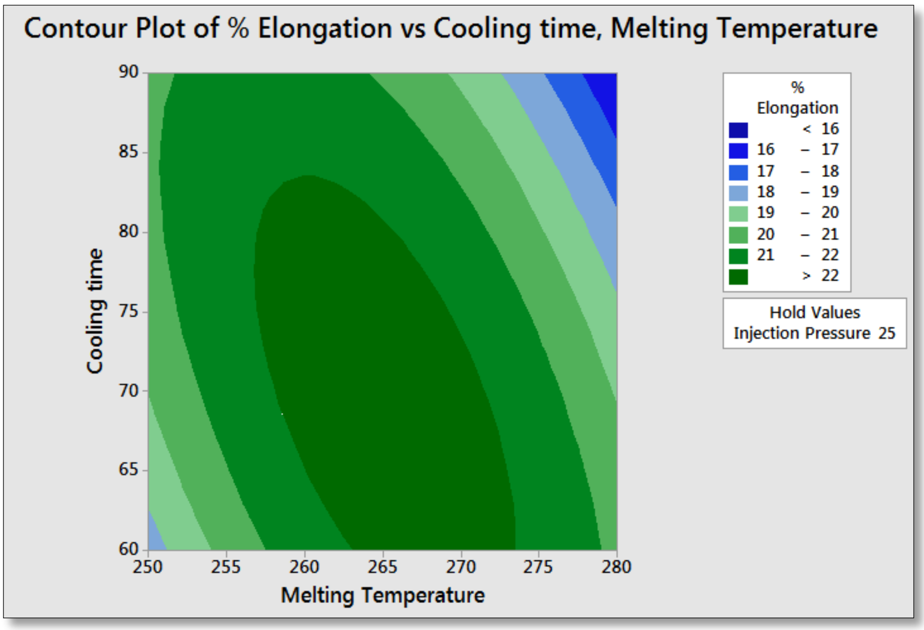

Figure 4.11: Contour Plot of Elongation vs Ct, MeT

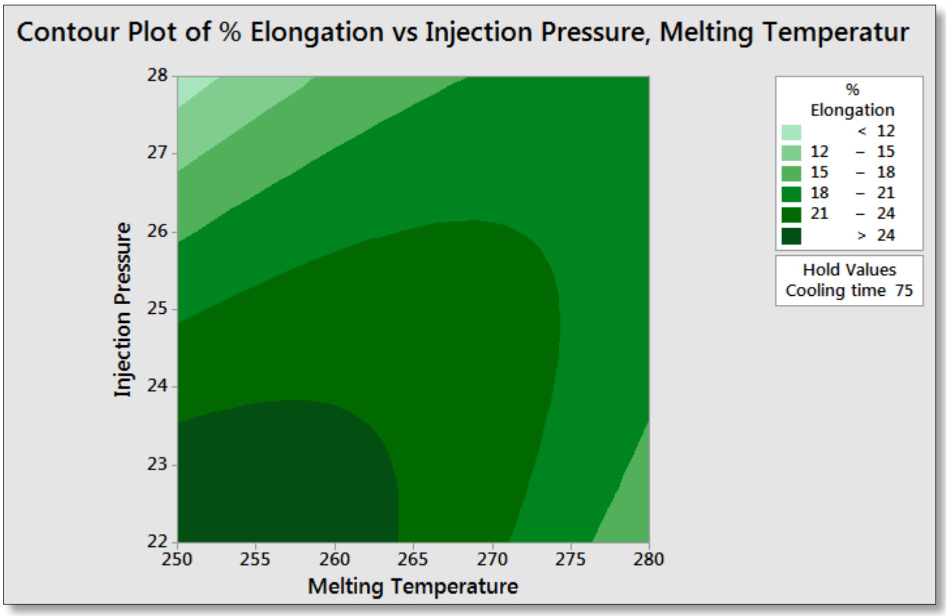

Figure 4.12: Contour Plot of Elongation vs IP, MeT

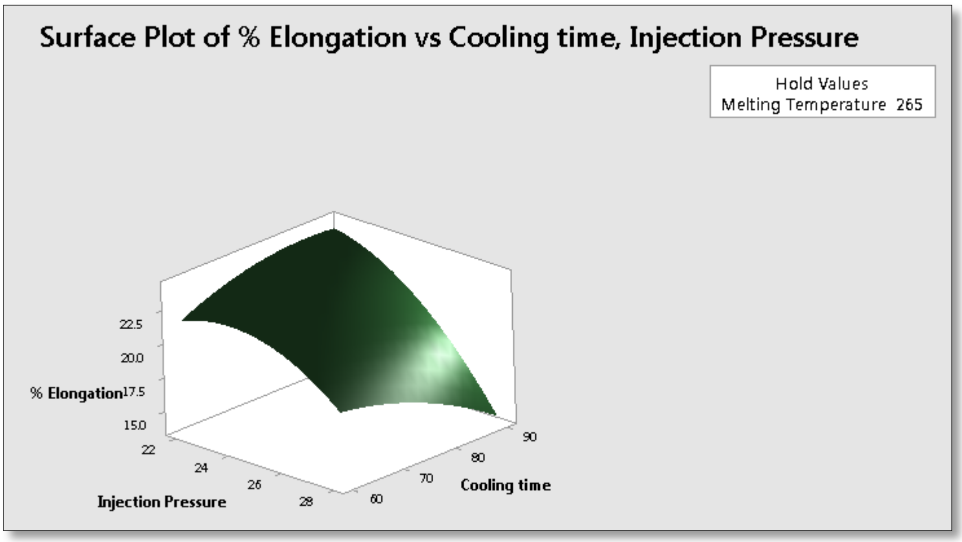

Figure 4.13: Surface Plot of Elongation vs IP, Ct

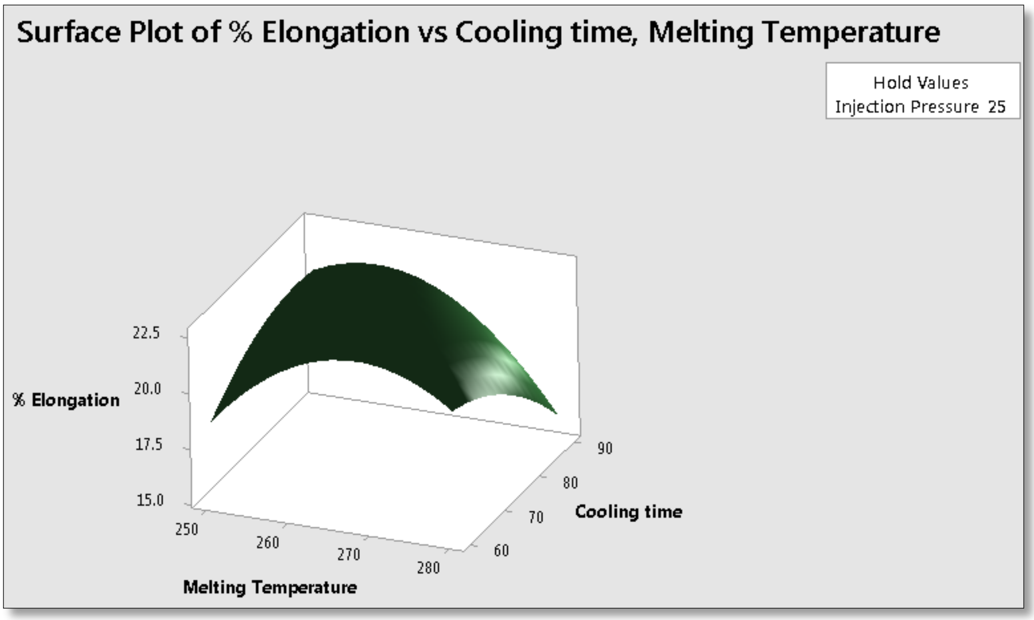

Figure 4.14: Surface Plot of Elongation vs Ct, MeT

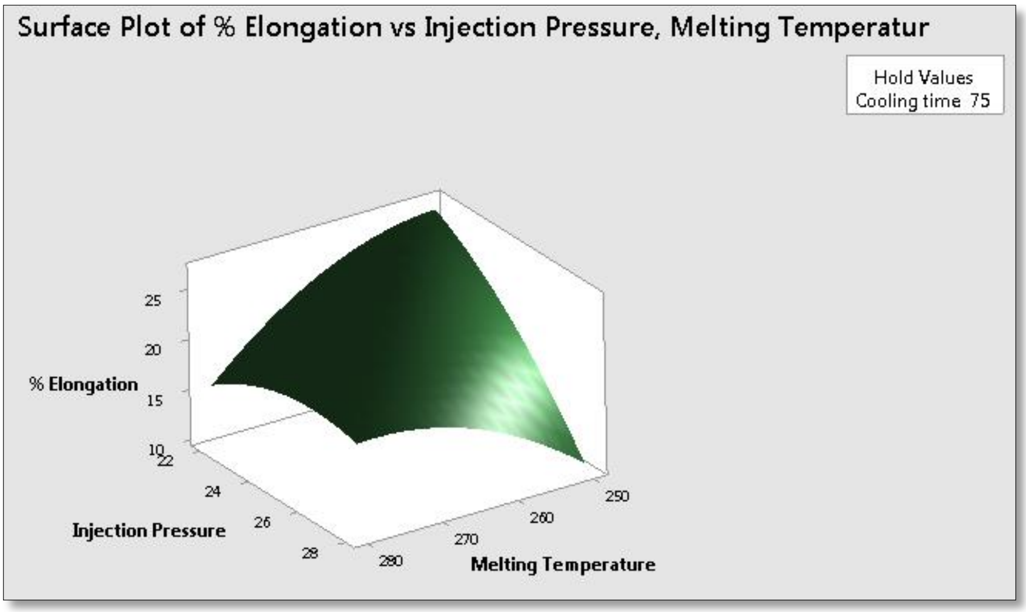

Figure 4.15: Surface Plot of Elongation vs IP, MeT

Single Optimization of Tensile Strength, Tensile Modulus and Elongation

One of the advantages of RSM is able to determine the optimized parameters based on target setting. The target can be decided based on minimum, maximum or even specific target value of response. For the experimental work, the target is to find the highest tensile strength within the range value of varied parameters. Figure 4.16 shows the optimized parameters based on the target and parameters set.

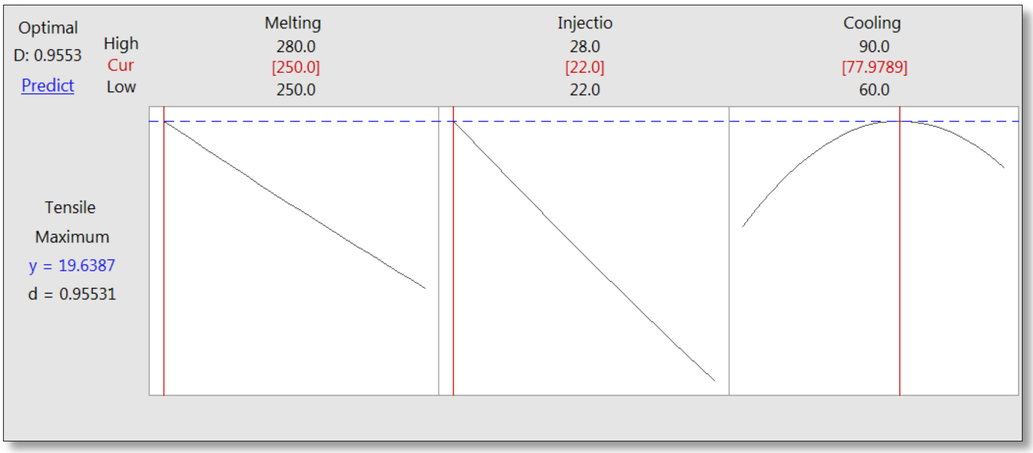

Figure 4.16: Optimization Plot Of Tensile Strength

From Figure 4.16, it displays that the optimized parameters values are 250°C MeT, 22 MPa IP and Ct of 77.97 seconds. These optimized parameters have 0.95531 desirability to achieve the highest value of tensile strength. From the optimized set of parameters, the predicted value of achievable tensile strength is equal to 19.6387 N/m^2. Meanwhile, Figure 4.31 shows the optimized parameters based on the target and parameters set for tensile modulus.

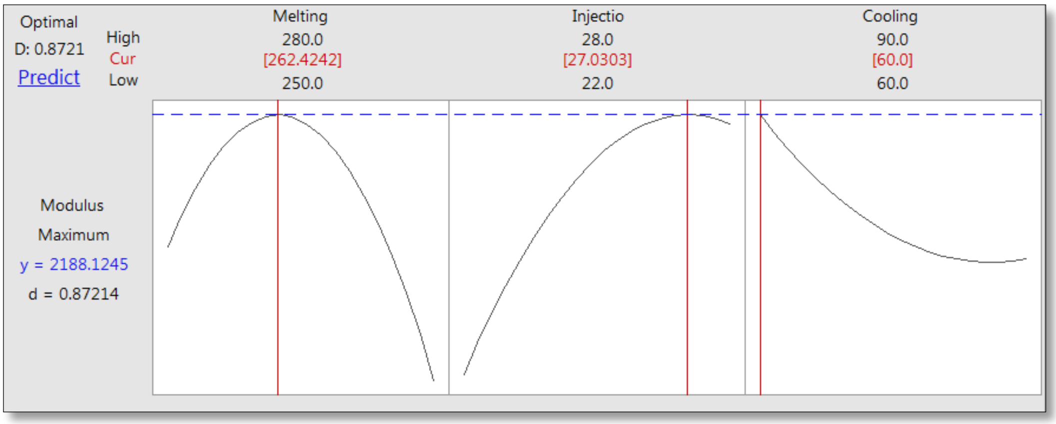

Figure 4.17: Optimization Plot Of Tensile Modulus

From Figure 4.17, it displays that the optimized parameters values are 262.4°C MeT, 27.03 MPa IP and Ct of 60 seconds. These optimized parameters have 0.87214 desirability to achieve the highest value of tensile modulus. From the optimized set of parameters, the predicted value of achievable tensile modulus is equal to 2188.12 N/mm. On the other hand, Figure 4.18 shows the optimized parameters based on the target and parameters set for elongation.

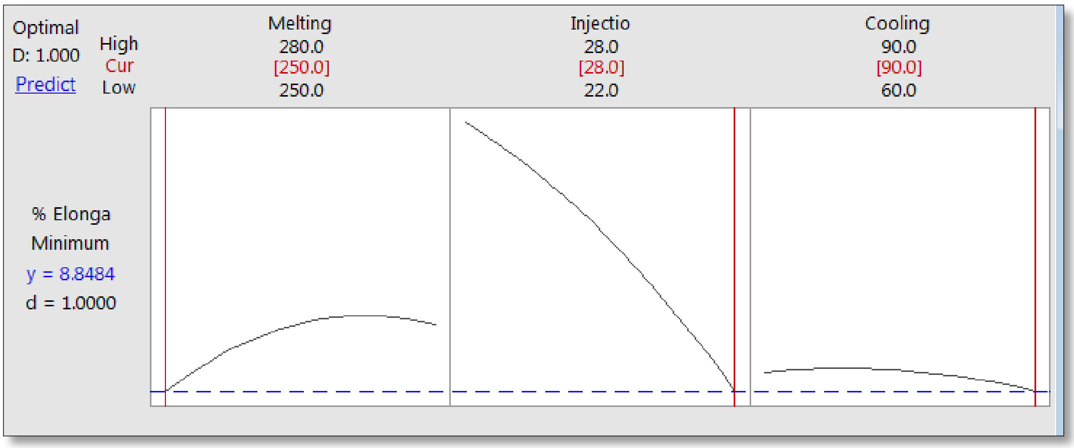

Figure 4.18: Optimization Plot Of Elongation

From Figure 4.18, it displays that the optimized parameters values are 250°C MeT, 28 MPa IP and Ct of 90 seconds. These optimized parameters have 1.0 desirability whereby it is 100% success of achieving the shortest elongation. From the optimized set of parameters, the predicted value of achievable shortest elongation equal to 8.85%.

Multiple Optimization of Tensile Strength, Tensile Modulus and Elongation

In the first part of the optimization, the three responses are optimized individually; tensile strength, tensile modulus and elongation. Apart of single optimization, RSM is able to perform multiple optimizations whereby all three responses can be optimized simultaneously according to varied parameter. Therefore, all three responses; tensile strength, tensile modulus and elongation can be decided based on minimum, maximum or even specific target value of response. For the experimental work, the target is to find the highest tensile strength, highest tensile modulus and shortest elongation within the range value of varied parameters. Figure 4.20 shows the multiple optimized responses based on the target and parameters set. From Figure 4.20, it displays that the multiple optimized parameters values are 252.4°C MeT, 27.8 MPa IP and Ct of 60 seconds. These optimized parameters lead to 0.361 desirability to achieve the highest value of 18.99 N/m^2 tensile strength. Meanwhile, for tensile modulus, the desirability to achieve the highest value for tensile modulus is 0.716. This value of desirability results the highest tensile modulus of 2092.53 N/mm. The greatest desirability of the multiple optimization parameter belongs to elongation response. It contributes 0.9984 desirability in order to achieve the shortest elongation.

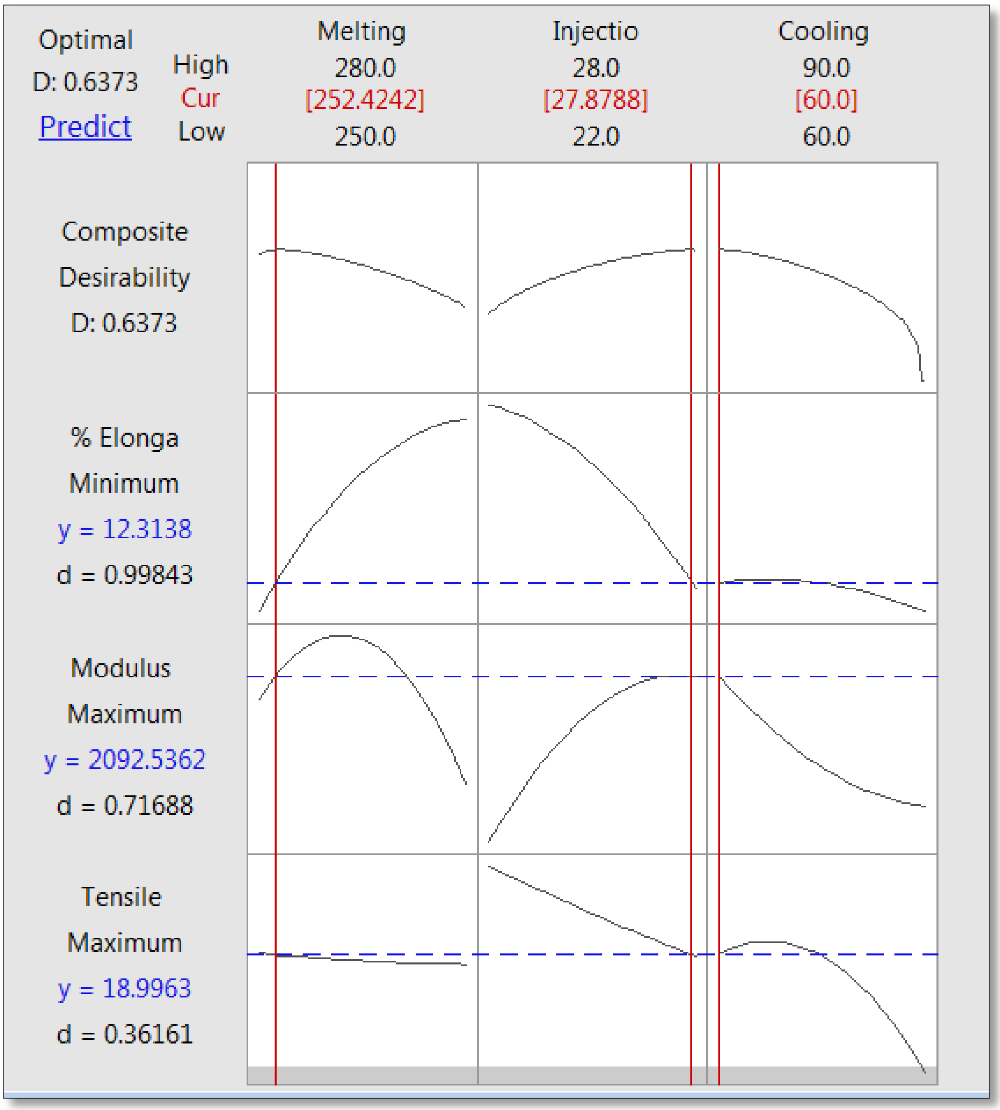

Figure 4.20: Multiple Optimization Plot

Conclusion

Based on the analysis of results, the following conclusions are drawn. As for the interaction among parameter, it can be concluded that the highest tensile strength is achieved when the injection pressure (IP) is in the lowest value. The maximum tensile modulus is attained significantly during cooling time at both lowest and highest value. Besides, the longest elongation occurred ultimately at both lowest and highest value of cooling time.

For the single optimization is found that the optimized parameters values are 250°C MeT, 22 MPa IP and Ct of 77.97 seconds. These optimized parameters have 0.95531 desirability to achieve the highest value of tensile strength. Meanwhile for the in order to obtain the highest tensile modulus, the optimized parameters values are 262.4°C MeT, 27.0 MPa IP and Ct of 60 seconds. For the elongation, it displays that the optimized parameters values are 250°C MeT, 28 MPa IP and Ct of 90 seconds. These optimized parameters have 1.0 desirability whereby it is 100% success of achieving the shortest elongation.

As for multiple optimizations, the multiple optimized parameters values are 252.4°C MeT, 27.8 MPa IP and Ct of 60 seconds. These optimized parameters lead to 0.361 desirability to achieve the highest value of 18.99 N/m^2 tensile strength. Meanwhile, for tensile modulus, the desirability to achieve the highest value for tensile modulus is 0.716. This value of desirability results the highest tensile modulus of 2092.53 N/mm. The greatest desirability of the multiple optimization parameter belongs to elongation response. It contributes 0.9984 desirability in order to achieve the shortest elongation.

Reference

Akbarian, A. M. (2014). Application of response surface methodology: Design of Experiments and Optimization: A mini review. *Indian Journal of Fundamental and Applied Life Sciences*, pp. 2434-2439.

American Chemistry Council . (2018 ,21). Retrieved from American Chemistry Council : https://plastics.americanchemistry.com/How-Plastics-Are-Made/

AnnaWitek-Krowiak, K. P. (2014). Application of response surface methodology and artificial neural network methods in modelling and optimization of biosorption process. *Bioresource Technology*, pp. 150-160.

Azuddin, T. T. (2017). Influence of injection temperatures and fiberglass compositions on mechanical properties of polypropylene . *International Technical Postgraduate Conference*, (p. 012080).

Carbon fiber vs. fiberglass. (2018). Retrieved 13, 2018, from Carbon fiber vs. fiberglass: https://infogram.com/carbon-fiber-vs-fiberglass-1gdk8pd471dvpq0

Dominick V. Rosato, D. V. (2000). *Injection Molding Handbook*. Kluwer Academic.

Douglas, M. (2005). *esign and Analysis of Experiments Response Surface Method and Designs*. New Jersey: John Wiley and Sons, Inc.

Fiberglass. (2018). Retrieved from How products are made : http://www.madehow.com/Volume-2/Fiberglass.html

Fiberglass and Composite Material Design Guide. (2018, 12). Retrieved from Performance Composites Inc.: http://www.performancecomposites.com/about-composites-technical-info/122-designing-with-fiberglass.html

G. Karian Harutun. (2003). *Handbook of polypropylene and polypropylene composite* . Marcei Dekker, Inc,.

Gurjeet Singh, M. K. (2015). Effect of Injection Moulding Process Parameter on. *International Journal of Mechanical, Aerospace, Industrial, Mechatronic and Manufacturing Engineering*, pp. 9.

Gurjeet Singha, A. V. (2017). A Brief Review on injection moulding manufacturing process. *Materials Today: Proceedings*, pp. 1423–1433.

Hassan, H. (2013). An experimental work on the effect of injection moldingparameters on the cavity pressure and product weight. *Int J Adv Manuf Technol*, 675–686.

K. Madan Shankar, D. K. (2017). Analyzing sustainable manufacturing practices – A case study in Indian context. *Journal of Cleaner Production, 164*, pp. 1332-1343.

Khuri, M. R. (1979). *A new procedure for steepest ascents*. Communications in Statistics - Theory and Method.

Lin, Y. H. (2007). Optimization of injection molding process for tensile and wear properties of polypropylene components via Taguchi and design of experiments method. *Polymer-Plastics Technology and Engineering*, pp. 96-105.

Liu, S.-J. a.-S. (2004). The manufacturing of thermoplastic composite parts by water-assisted injection-molding technology. *Composites Part A: Applied Science and Manufacturing 35,*, pp. 171-180.

Marcos Almeida Bezerraa, R. E. (2008). Response surface methodology (RSM) as a tool for optimization in analytical chemistry. *Talanta 76*, pp. 965–977.

Mathivanan, D. M. (2010). Minimization of sink mark defects in injection molding process–Taguchi approach. *International Journal of Engineering, Science and Technology 2*, pp. 13-22.

Montgomery, M. R. (2002). *Response Surface Methodology: process and product optimization using designed experiment,.".* A Wiley-Interscience Publication.

Mulroy, J. (2017, 75). *How to Run a Plastic Injection Molding Machine*. Retrieved 4 1, 2018, from https://careertrend.com/how-7816018-run-plastic-injection-molding-machine.html

Ozcelik, B. a. (2006). Comparison of the warpage optimization in the plastic injection molding using ANOVA, neural network model and genetic algorithm. *Journal of materials processing technology 171*, pp. 437-445.

Pareek, R. &. (2013). Optimization of Injection Moulding Process using Taguchi and ANOVA. *Journal of Scientific and Engineering Research*.

Park, G.-J. (2007). *Analytic Methods for Design Practice.* Springer-Verlag London.

Plastic Material Melt And Mould Temperatures. (2018). Retrieved from PlastikCity: https://www.plastikcity.co.uk/useful-stuff/material-melt-mould-temperatures

Polmak Plastik . (2011). Retrieved from Dr. BOY Injection Molding Machines: http://www.polmakplastik.com/en/representation-dr-boy-injection-molding-machines-58.html

Polypropylene . (2010). Retrieved 1 1, 2018, from United Plastic Component : http://www.upcinc.com/resources/materials/PP.html

Propylene (PP). (2010). Retrieved from United Plactic Component : http://www.upcinc.com/resources/materials/PP.html

Qualitest . (1999). Retrieved from Universal Testing Machine - Tensile Tester: http://www.worldoftest.com/universal-testing-machine-tensile-tester

Sinto Jacob, K. K. (2009). Modification of Polypropylene/Glass Fiber. *Macromol. Symp*, pp. 138–143.

Sinto Jacob, K. K. (2009). Modification of Polypropylene/Glass Fiber Composites with Nanosilica. *Macromol. Symp.*, pp. 138–143.

Siuli, A. K. (2010). *Response surface methodology. In: Computational Statistics.* John Wiley & Sons, Inc.

Sven-Olaf Lindert, G. R. (2014). Identification and Control of an Injection Moulding Machine. *Proceedings of the 19th World Congress* . Cape Town: The International Federation of Automatic Control.

Uzair Ahmed Dar, Y. J.-U. (2016). The effect of injection molding process parameters on mechanical and fracture behavior of polycarbonate polymer. *Journal of applied polymer Science* , pp. 44474.

W.N. Ota, S. A. (2005). Studies on the combined effect of injection temperature and fiber content on the properties of polypropylene-glass fiber composites. *Composites Science and Technology*, pp. 873–881.

Yan SY, L. pp. L. (1996). Experimental study of injection compression molding of cylindrical parts. *Polym Proc*, pp. 205–223.

Zhu, J. C. (2004). Tensile Strength and Optimization of Injection Molding Processing Parameters Using the Taguchi Method. *The International Journal of Modern*

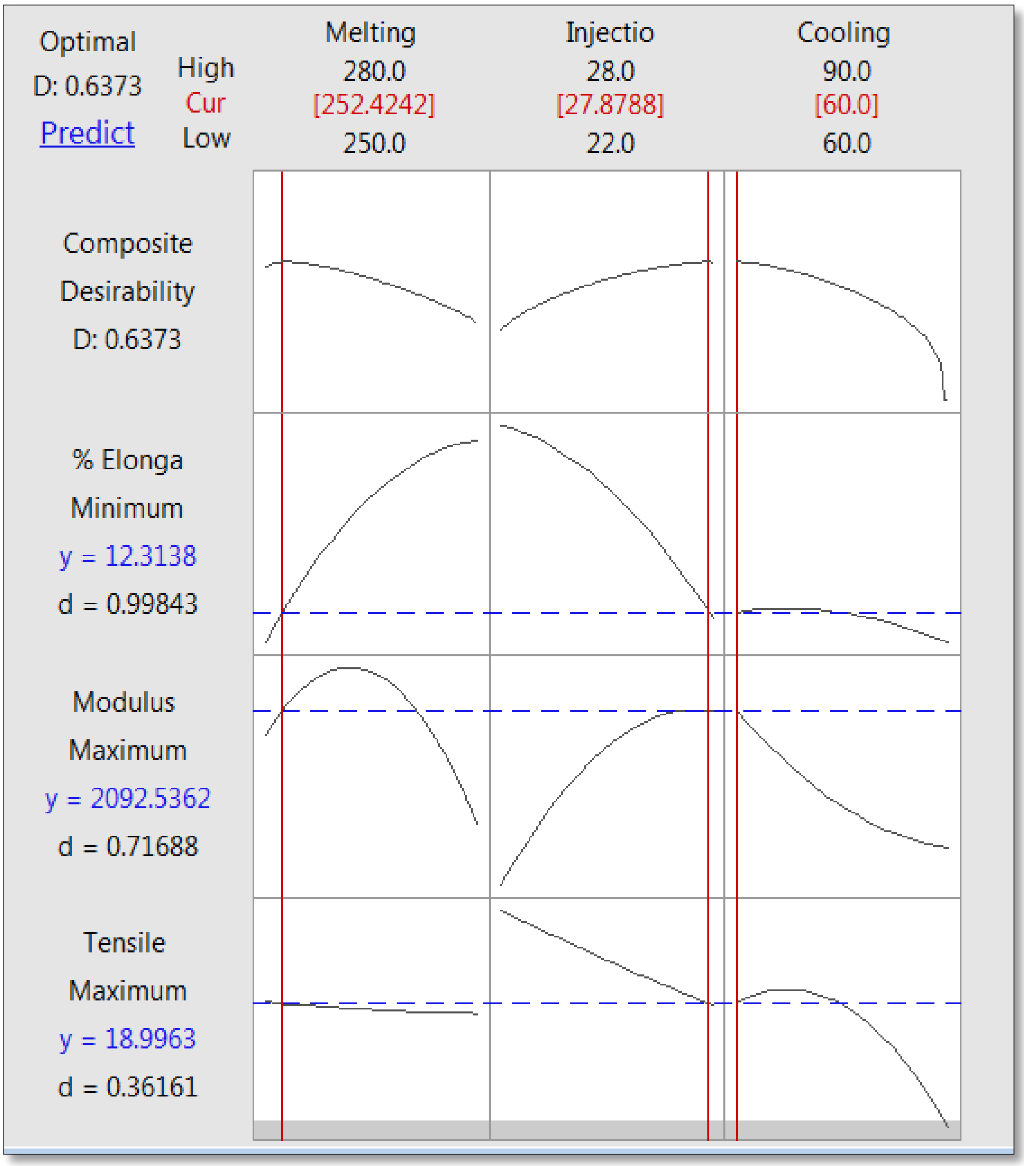

Figure 4.33: Multiple optimization plot

EXPERIMENTAL INVESTIGATION ON THE EFFECT OF DIVERGENT TOWER SOLAR CHIMNEY ON THE THEORETICAL POWER POTENTIAL

Ahmad Jawad
Mohd Suffian Misaran[1]
Md. Mizanur Rahman[2]
Mohd Azlan Ismail[1]

[1]Faculty of Engineering, Universiti Malaysia Sabah (UMS), Malaysia, (E-mail: suffian@ums.edu.my)
[2]Mechatronics Engineering Department, World University Bangladesh, Bangladesh, (E-mail: mizanur.rahman@mte.wub.edu.bd)

Abstract: *Solar chimney power plant is a sustainable alternative for electricity generation using solar as the source of energy. In general, the main body of a solar chimney plant requires a tall structure which is costly and challenging to construct. Thus, it is important to increase the performance of the solar chimney power plant and have a better energy-cost ratio. This study aims to experimentally investigate the influence of divergent solar chimney as opposed to a cylindrical chimney on solar chimney performance. Three divergent scaled-down solar chimney model at 1-meter, 1.5-meter and 2-meter were fabricated and tested for its performance at various simulated heat loads. The test results were compared with similar heights cylindrical solar chimney. The experiments show that divergent solar chimney increases the theoretical power generation potential and improves the stalk effect and have higher outlet velocity compared to a cylindrical solar chimney. The power potential of the divergent chimney is increased up to 18 times with the maximum theoretical power obtain at 0.183W on the 2-meter divergent chimney. Higher temperature was recorded on the 2-meter divergent chimney outlet at 341.3k compared to 330.4k on the cylindrical chimney indicates better stack effect. The highest average velocities in the divergent and cylindrical chimneys were recorded under the electric heat load of 2 kW at 0.994 m/s and 0.820 m/s respectively in the 1-meter configuration. It is also observed that the air velocity in a shorter divergent chimney is higher than taller divergent chimney models while better compared to all cylindrical height. This study finds that a shorter divergent solar chimney produces greater energy compared to a higher cylindrical solar chimney. Therefore, it is possible to reduce the overall cost of solar chimney by reducing the height of the main structure without sacrificing the performance of the solar chimney.*

Keywords: *Solar Energy, Solar Chimney, Divergent Chimney, Performance Enhancement*

Introduction

Solar energy has been used for centuries as it is one of the most reliable and sustainable sources of energy available. The most common form of solar energy would be Solar PV systems, however, the systems does have its fair share of disadvantage such as efficiency degradation over time and toxic materials used. Alternatively, a solar chimney power plant (SCPP) uses solar radiation to generate electric power as well as a hybrid system using secondary waste heat from a plant or a geothermal, without the quirks of a solar PV system. This allows the SCPP systems to operate continuously day and night at moderate weather. Solar chimney power plant working principle is simple; solar collectors gather solar radiation to heat the air, this hot air naturally rises upwards due to the buoyancy effect channelled to the chimney. Bladed turbine mounted inside the chimney converts kinetic energy into mechanical energy and generate electric power in the generator. The hot air is released harmlessly to the surrounding air from the chimney outlet at several hundred meters above base.

A first functional prototype of solar chimney was launched in Spain in the year of 1982 it lasts for 8 years has chimney height of 195 meters long and while diameter was 10 meters wide and had generating capability of 50 kW(Haaf et al. 1983). Solar chimney power plants projects generally less successful, cancelled, and postponed due to high capital cost and limited power generation capability. This motivates researchers to study ways of reducing cost caused by the structure size and boost the performance of solar chimney power plant. Fasel et al. (2012) studied several scaled version of the Manzanares prototype using CFD method, the study suggests that power generation increases with the increment of chimney height and solar collector size of solar chimney power plants. Various approach has been proposed to reduce the cost associated with the solar chimney main structure. Papageorgiou (2010) introduced the concept of the floating chimney made with fabric that is cost-effective and safe during an earthquake, however, crosswinds can deflect the chimney affecting the chimney performance. Aurybi et al. (2018a) propose a solar chimney integrated with a thermal power plant, it uses the hot waste flue gas as a heat source to operate the solar chimney during night time or at low solar radiation intensity (Aurybi et al. 2018b). Hu et al. (2017a,2017b) performed numerical solution on cylindrical, divergent and various shape of diffuser chimney. Numerical outcomes conclude that divergent shaped chimney is 13 times more efficient than the cylindrical chimney(Hu, Leung, and Chan, 2017). Moreover, the study validated numerical solution with outcomes obtained from the CFD performed on a divergent shaped chimney with different area ratios and cylindrical chimney, the results suggest a 100-meter divergent chimney can generate 380kW which exceed the power generated by a 200 meter and 300-meter cylindrical chimney (Hu and Leung 2017). Convergent chimney performance was also studied by several researchers(Ubhale, 2016;Pattanashetti and Madhukeshwara, 2014). The study concludes divergent chimney is more efficient compared to a convergent shaped chimney because it has higher kinetic energy at the base where the turbine is located(Pattanashetti and Madhukeshwara, 2014; Koonsrisuk and Chitsomboon, 2013a). Furthermore, high velocity at the exits of the chimney equates to low pressure possibly causing chocking phenomena (Kubo, Miyazato, and Matsuo 2010).

Current literature has reported the advantage of using divergent solar chimney using simulated results, however, few laboratory experiments on the subject are available. Thus, this study aims to experimentally investigate the performance of divergent solar chimney compared to a cylindrical chimney in a laboratory condition.

Methodology

A scaled-down model of the solar chimney was designed and fabricated in the lab based on the physical dimension of the Manzanares prototype SCPP as shown in Table 1. The natural buoyancy Equation was used to calculate the theoretical air velocity inside the chimney as shown in Equation 1 (Schlaich 1995), and the diameter of the chimney was calculated using the Fourier Equation as shown in Equation 2 (Chakrabarti 2005).

Table 1: Physical Parameters of Manzanares Prototype

Height (m)	Diameter (m)	Air velocity (m/s)	Temperature difference (K)	Ambient Temperature (k)
194.6	10	9.1	20	293

$$v = \sqrt{\frac{2gh\Delta T}{T_\infty}} \quad (1)$$

$$fr = \frac{v}{\sqrt{gD}} \quad (2)$$

Ahmed and Patel (2017) reported that the divergent chimney performance is optimal at the throat angle of 2°. Thus, the divergent shaped chimney was designed and fabricated with the throat angle fixed at 2°. Bellmouth parameters were obtained using Equation no. 3 (Idelchik 1986). Figure 1 shows the important dimensions of a diverged solar chimney.

$$BM_h = 0.2\sim0.8 \times D_h \quad (3)$$

$$BM_r = 0.2\sim0.4 \times D_h \quad (4)$$

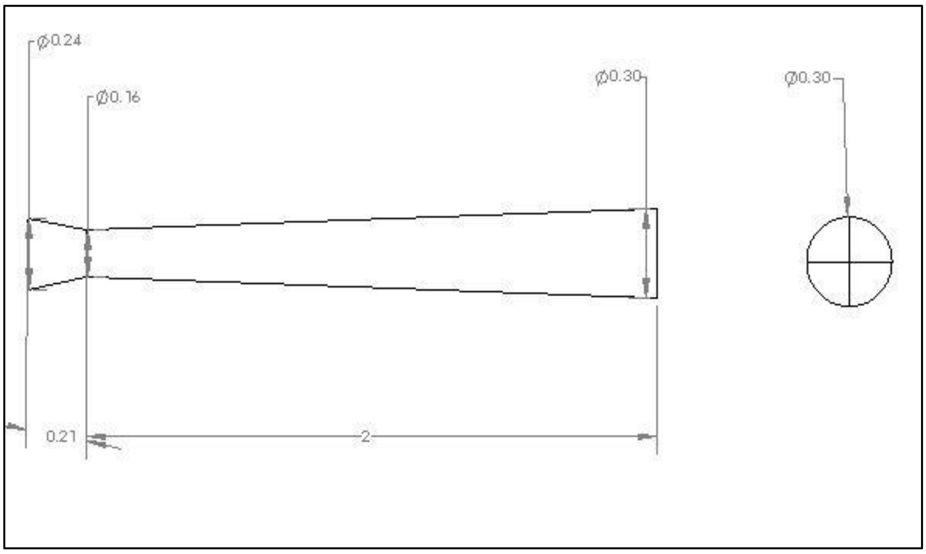

Figure 10: Schematic Figure of A Divergent Chimney

The final dimension of the scaled-down model of the Manzanares Solar Chimney is as shown in Table 2. This study designed and fabricated 3 solar chimney model; 1-meter, 1.5-meter and 2-meter diverged solar chimney as shown in Figure 2 (a).

Table 2: Dimension for The Chimney Models

Height (m)	Divergent Chimney			Cylindrical Chimney
	Diameter (m)	Bellmouth Height (m)	Bellmouth Diameter (m)	Diameter (m)
2	0.3	0.21	0.24	0.28
1.5	0.23	0.161	0.092	0.21
1	0.15	0.105	0.06	0.14

Three matching cylindrical chimney model were experimented as well to study and compare the performance of each chimney compared to the equivalent divergent chimney. The height and diameter of cylindrical solar chimney models are as shown in Table 2.

(a) (b)

Figure 11:(A) Divergent Chimneys (B) Cylindrical Chimneys

In this experiment, heating coil of 2kW was used as a replacement heat source located at the inlet of the chimney. Voltage regulator and digital multimeter were used to control the required electric heat load which is varied from 0.9kW to 2.0kW. The exit air velocity was measured using an anemometer model CENTER 330. The temperature variation was measured using K-type thermocouple and a data logger model 18200-40 (Cole Palmer). Four thermocouples were located in the following location; inside the chimney (T1), exit of the chimney (T2), 10 centimetres above the exit of the chimney (T3) and ambient lab temperature (T4). All the thermocouples were further attached with a data logger which was set to record temperature reading at every five seconds. The schematic diagram of the experimental setup is as shown in Figure 3.

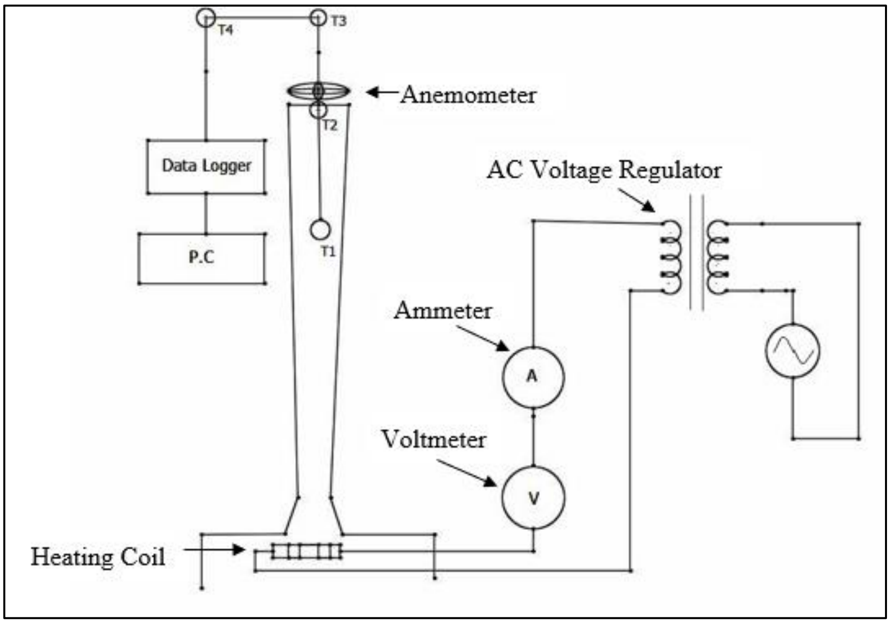

Figure 12: Schematic Diagram Of The Experimental Setup

The performance of the chimneys was measured based on the operating parameter at various electric heat loads; 0.9 kW, 1.3 kW, 1.6 kW and 2 kW. The temperature and air outlet velocity at the specified heat loads were measured and recorded. Density was calculated from the hot saturated air properties as shown in Equation 5 using air properties between 0°C and 120°C for air properties at 1atm pressure (Cengel 2014). Air velocity at the throat was calculated using energy balance Equation as shown in Equation 6. The mass flow rate was calculated using Equation 7.

$$\rho = 1\text{E-}05T^2 - 0.0045T + 1.29 \qquad (5)$$

$$V_1A_2 = V_2A_2 \qquad (6)$$

$$\dot{m} = \rho A_{ch} V \qquad (7)$$

The power potential of each solar chimney was calculated using Equation 8 (Bernardes and von Backström 2010). In the case of divergent shaped chimney, air velocity at the throat was further used for the theoretical power generation potential. Theoretical electric power generation was calculated using Equation 9.

$$P_{wind} = \frac{1}{2}\rho \times A_{ch} \times V^3 \qquad (8)$$

$$P_{electric} = P_{wind} \times \eta_t \times \eta_g \qquad (9)$$

Results and Analysis

Average Velocity

Experiments were conducted on the different models of divergent and cylindrical chimney under different electric heat loads. Figure 5 represents the air velocity of divergent and cylindrical chimneys under different heat loads. The highest average velocities in the divergent and cylindrical chimneys were recorded under the electric heat load of 2 kW at 0.994 m/s and 0.820 m/s respectively in the 1m configuration. The lowest average velocity of the cylindrical chimney was recorded as 0.41 m/s while 0.49 m/s was recorded in the divergent chimney at electric heat load of 0.9 kW and 2m configuration. It is observed that the air velocity at the outlet decreases with an increase in solar chimney height. This is because the divergent chimney height from the throat and section area effect air velocity; shorter chimney tends to have shorter distance and smaller section area from the throat compared to a taller chimney.

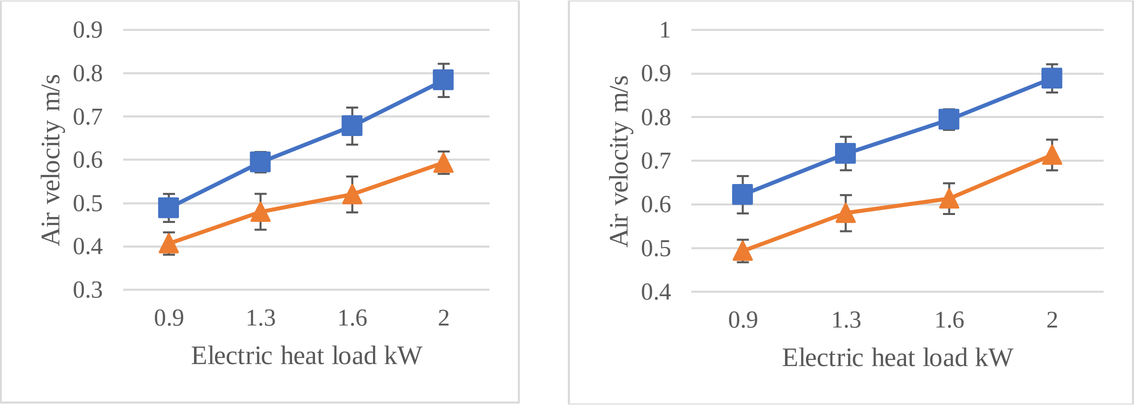

(a) (b)

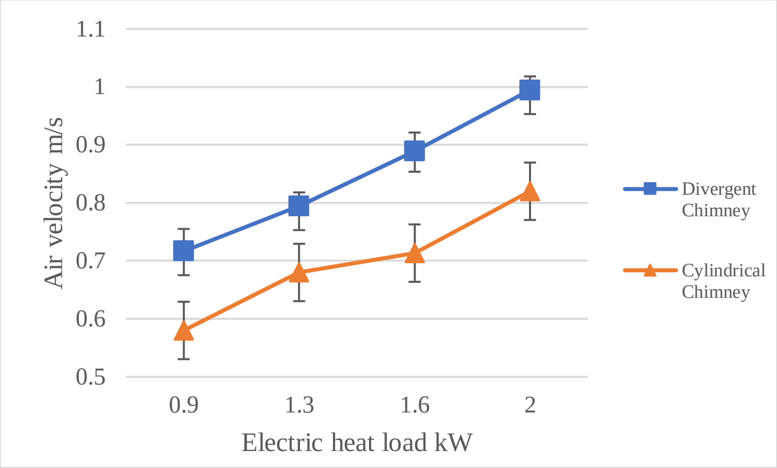

(c)

Figure 13: Air Velocity Comparison of Divergent And Cylindrical Chimneys Under Different Electric Heat Loads (A) 2-Meter (B) 1.5-Meter (C) 1-Meter

Airflow in a solar chimney is explained through the concept of the stack effect. Amongst others, the stack/stack impact overall performance relies on temperature differences at the inlet and the top of the chimney. Thus, it is essential to analyze the temperature variations in the divergent and cylindrical solar chimney. All temperature measurement shows that divergent chimneys have greater temperatures differences compared to cylindrical chimneys as shown in Table 3. Maximum average temperature scale recorded was 55.4 K in the 1-meter divergent chimney as oppose to 38.9 K in the cylindrical chimney. This indicates that the divergent shape of chimney improves the stalk effect.

Table 3: Outlet Temperature of the 1 m, 1.5 m and 2 m divergent and cylindrical chimney at different electric heat loads

Electric heat load	Outlet temperature in divergent chimney, T2			Temperature difference with inlet/ambient			Outlet temperature in cylindrical chimney, T2			Temperature difference with inlet/ambient		
	1 m	1.5 m	2 m	1 m	1.5 m	2 m	1 m	1.5 m	2 m	1 m	1.5 m	2 m
kW	K	K	K	K	K	K	K	K	K	K	K	K
0.9	341.9	330.1	326.5	38.9	27.1	23.5	334.9	324.1	320.2	31.9	21.1	17.2
1.3	350.2	339.4	335.9	47.2	36.4	32.9	335.8	327.8	324.0	32.8	24.8	21.0
1.6	354.5	341.1	337.6	51.5	38.1	34.6	339.2	330.7	326.0	36.2	27.7	23.0
2	358.4	342.5	341.3	55.4	39.5	38.3	341.9	334.9	330.4	38.9	31.9	27.4

Temperature measurement in the experiment shows that higher temperature data is recorded in shorter chimney configuration. This is because the collector size is kept constant at 0.8 m^2 for all chimney models. Since a 1-meter chimney is smaller in footprint size compared to the 2 m chimneys (scaled), more surface area is available to heat the air inside the collector resulting in a higher temperature at the inlet. This higher temperature increases the buoyancy effect that increases air velocity in a short chimney model compare to tall chimney models. Furthermore, shorter chimney has fewer air frictions and thermal losses due to smaller size compared to the large-scaled chimney. Thus the higher temperature difference in short scaled models causes higher air velocity due to the buoyancy (Schlaich 1995). Therefore, this greater temperature difference in short scaled cylindrical chimney models causes greater air velocity due to the fact of the buoyancy (Schlaich, 1995)

Mass Flow Rate

Mass flow rate is a crucial property to calculate the power potential of the chimneys. Although air velocity was higher in short-scale chimneys, the mass flow rate increases in line with the chimney scale. Figure 6 shows the mass flowrate in the 1, 1.5 and 2-meter divergent shaped chimneys. It is observed that the mass flowrate in the 1.5-meter divergent chimney is 1.5 times greater mass flowrate in contrast to 1-meter divergent chimney, whereas 2-meter divergent chimney has 1.5 times more mass flowrate in compared to 1.5-meter divergent chimney and 2.2 times greater compared to 1-meter divergent chimney using electrical heat load 2 kW. Similar trends are observed in the case of the cylindrical chimney. The highest mass flow rate was calculated in the tallest chimney because of the big cross-section area though air velocity was low compared to small scale chimney.

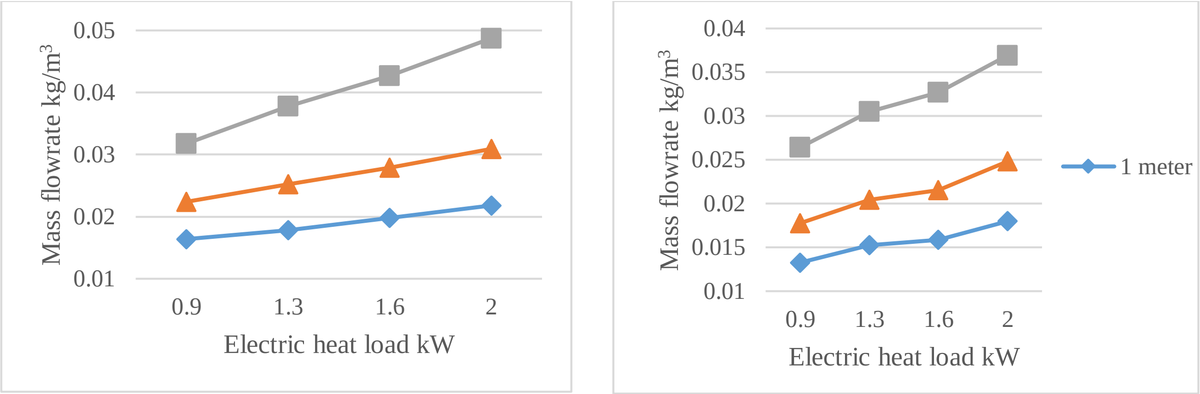

(a) (b)

Figure 6:Mass flowrate of (a) divergent chimney and (b) Cylindrical chimney under different electric heat loads

Theoretical Electric Power Potential

The experimental outcomes obtained from divergent and cylindrical chimneys were used to calculate the theoretical wind power potential using Equation (9) and theoretical energy generation using Equation (10). The results were compared with the electric heat load used in the divergent and cylindrical chimney experiment. Theoretical wind power potential increases with an increment of the electric heat load and height of chimneys. Also, the wind power potential is greater in the divergent solar chimneys compared to the cylindrical chimneys. Such behaviour occurs because the velocity at the throat in a divergent chimney increases due to a reduction of the area and results in greater kinetic energy compared to a straight cylindrical chimney(Bouabidi et al. 2018).

The theoretical wind power potential was further used to simulate theoretical electric power generated by using Equation (10); the turbine efficiency and generator efficiency was assumed at 85% and 90% respectively. Figure 7 and 8 shows the theoretical electric power generation for 3 different heights of the divergent and cylindrical solar chimney at various electric heat loads. Calculated data shows a large difference in theoretical power generated between 1-meter and 2-meter divergent chimney models which were not observed in cylindrical chimneys. The theoretical electric power generation of 1-meter chimney is 0.068 Watt whereas the 2-meter solar chimney is capable to generate 0.183 Watt at 2 kW electric heat load, a variance of 169%. The larger cross-sectional area of the 2-meter chimney contributes to higher mass flow rate and in turn higher theoretical electric power potential. However, although cylindrical chimney does shows an increase in theoretical power potential with chimney height increment; the increase was insignificant at 11%.

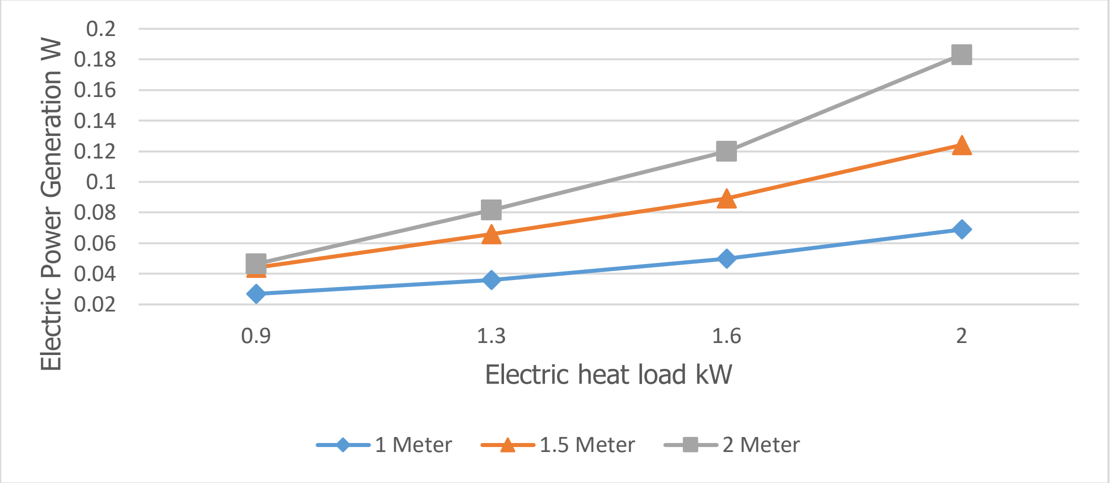

Figure 9: Theoretical Electric Power Generation in Divergent Chimneys

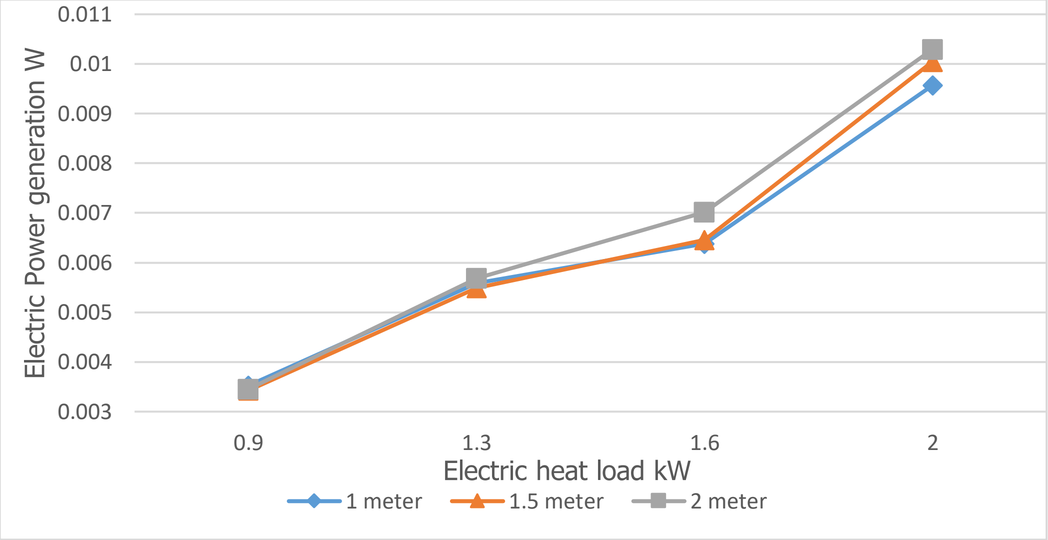

Figure 10: Theoretical Electric Power Generation In Cylindrical Chimneys

The theoretical electric power generation shows that divergent chimney has a greater potential to generate higher electric power compared to a cylindrical chimney. This phenomenon is contributed to the pressure recovery mechanism within the divergent chimney due to the particular shape of its diffuser as critically analysed by some researchers (Koonsrisuk and Chitsomboon 2013b)(Hu, Leung, and Chen 2017). The divergent chimney is 1.5 to 26 times more efficient compared to the cylindrical chimney depending on the parameters like the throat angle, chimney height and solar radiation intensity (Hu, Leung, and Chan 2017). The results obtained from the current experiment shows 6 to 18 times better theoretical electric power generation in divergent chimney compared to cylindrical chimneys.

Conclusion

This study has successfully measured experimentally the performance of divergent solar chimney in a laboratory condition and compared the result data with cylindrical chimney performance. The result shows divergent chimneys have better theoretical electric generation performance up to 18 times better compared to a cylindrical chimney at the same height ratio. At the highest electric heat load and tallest chimney, the theoretical electric power generation in a divergent chimney achieve 0.183 Watt whereas only 0.01 Watt was theoretically generated in a cylindrical chimney. The experiments also suggest that shorter divergent chimney has a greater electric power generation potential compared to the taller cylindrical chimney. Thus, a shorter divergent solar chimney suggests capital cost reduction while producing higher electric power. This study suggests that in the future, the experiments should be conducted with the following recommendation; use a different height of solar chimney using the same base area, using an actual wind turbine to generate electricity and to conduct experimental work in an actual condition.

Acknowledgements

The authors wish to convey sincere gratitude to Universiti Malaysia Sabah (UMS) for supporting the current research work thru UMSGreat research grant, project no. GUG0171.

References

Ahmed, M. Rafiuddin, and Sandeep K. Patel. 2017. “Computational and Experimental Studies on Solar Chimney Power Plants for Power Generation in Pacific Island Countries.” *Energy Conversion and Management* 149:61–78. doi: 10.1016/j.enconman.2017.07.009.

Aurybi, Mohammed A., S. I. Gilani, Hussain H. Al-Kayiem, and Ali A. Ismaeel. 2018a. “Mathematical Evaluation of Solar Chimney Power Plant Collector, Integrated with External Heat Source for Non-Interrupted Power Generation.” *Sustainable Energy Technologies and Assessments* 30(December 2016):59–67. doi: 10.1016/j.seta.2018.06.012.

Bernardes, Marco Aurélio dos Santos, and Theodor W. von Backström. 2010. “Evaluation of Operational Control Strategies Applicable to Solar Chimney Power Plants.” *Solar Energy* 84(2):277–88. doi: 10.1016/j.solener.2009.11.009.

Bouabidi, Abdallah, Ahmed Ayadi, Haytham Nasraoui, Zied Driss, and Mohamed Salah Abid. 2018. “Study of Solar Chimney in Tunisia: Effect of the Chimney Configurations on the Local Flow Characteristics.” *Energy and Buildings* 169:27–38. doi: 10.1016/j.enbuild.2018.01.049.

Cengel, Yunus. 2014. *Heat and Mass Transfer: Fundamentals and Applications*. McGraw-Hill Higher Education.

Chakrabarti, Subrata K. 2005. “Physical Modelling of Offshore Structures.” Pp. 1001–54 in *Handbook of Offshore Engineering*. Elsevier.

Fasel, Hermann, Ehsan Shams, and Andreas Gross. 2012. “CFD ANALYSIS FOR SOLAR CHIMNEY POWER PLANTS.” (1):1524–32.

Haaf, W., K. Friedrich, G. MAYR, and J. Schlaich. 1983. “Part I: Principle and Construction of the Pilot Plant in Manzanares.” *International Journal of Solar Energy* 2(1):3–20. doi: 10.1080/01425918308909911.

Hu, Siyang, and Dennis Y. C. Leung. 2017. “Mathematical Modelling of the Performance of a Solar Chimney Power Plant with Divergent Chimneys.” *Energy Procedia* 110(December 2016):440–45. doi: 10.1016/j.egypro.2017.03.166.

Hu, Siyang, Dennis Y. C. Leung, and John C. Y. Chan. 2017. “Numerical Modelling and Comparison of the Performance of Diffuser-Type Solar Chimneys for Power Generation.” *Applied Energy* 204:948–57. doi: 10.1016/j.apenergy.2017.03.040.

Hu, Siyang, Dennis Y. C. Leung, and Michael Z. Q. Chen. 2017. “Effect of Divergent Chimneys on the Performance of a Solar Chimney Power Plant.” *Energy Procedia* 105:7–13. doi: 10.1016/j.egypro.2017.03.273.

Idelchik, Isaak E. 1986. “Handbook of Hydraulic Resistance.” *Washington, DC, Hemisphere Publishing Corp., 1986, 662 p. Translation.*

Koonsrisuk, Atit, and Tawit Chitsomboon. 2013a. “Effects of Flow Area Changes on the Potential of Solar Chimney Power Plants.” *Energy* 51:400–406. doi: 10.1016/j.energy.2012.12.051.

Koonsrisuk, Atit, and Tawit Chitsomboon. 2013b. “Mathematical Modeling of Solar Chimney Power Plants.” *Energy* 51:314–22. doi: 10.1016/j.energy.2012.10.038.

Kubo, Kazunori, Yoshiaki Miyazato, and Kazuyasu Matsuo. 2010. “Study of Choked Flows through a Convergent Nozzle.” *Journal of Thermal Science* 19(3):193–97. doi: 10.1007/s11630-010-0193-3.

Papageorgiou, Christos D. 2010. *Floating Solar Chimney Technology*.

Pattanashetti, Jagadeesh S., and N. Madhukeshwara. 2014. “INTERNATIONAL JOURNAL OF RESEARCH IN Numerical Investigation and Optimization of Solar Tower Power Plant .” 2(1):92–104.

Schlaich, Jorg. 1995. *The Solar Chimney: Electricity from the Sun*. Edition Axel Menges.

Ubhale, Nilesh N. 2016. “Improving the Gained Power from Solar Chimney by Changing Radius and Height Roof Inlet Radius D.” (June).

International Research Conference on Applied Sciences
and Engineering 2020 (IRCASE 2020)
eISBN 978-967-2426-20-2
13th – 14th December 2020

FEASIBILITY OF USING SOLAR PV WASTE HEAT TO REGENERATE LIQUID DESICCANT IN SOLAR LIQUID DESICCANT AIR CONDITIONING SYSTEM

Zulkurnain Bin Hassan [1]
Mohd Suffian Bin Misaran@Misran[2]
Nancy Julius Siambun[3]
Ag Sufiyan Abd Hamid[4]
Mohd Amran Madlan[5]

[1]Faculty of Engineering, (UMS), Kota Kinabalu, Sabah, Malaysia (E-mail: zulkurnainhassan@gmail.com)
[2]Faculty of Engineering, (UMS), Kota Kinabalu, Sabah, Malaysia, (E-mail: suffian@ums.edu.my)
[3]Faculty of Engineering, (UMS), Kota Kinabalu, Sabah, Malaysia, (E-mail: nancyjs@ums.edu.my)
[4]Faculty of Science and Natural Resources, (UMS, Kota Kinabalu, Sabah, Malaysia, (E-mail: pian@ums.edu.my)
[5]Faculty of Engineering, (UMS), Kota Kinabalu, Sabah, Malaysia, (E-mail: amran.madlan@ums.edu.my)

Abstract: *(Hybrid Photovoltaic (PV) units are systems that produce both electrical and thermal energy in a single unit. The purpose of this research is to investigate the feasibility of using PV solar waste heat to regenerate liquid desiccant in the solar air conditioning system. A typical liquid desiccant regenerator requires a temperature range between 50˚C and 60˚C. Thus, the heat recovery system is designed on a 50W solar PV that focuses on recovering, delivering, and transferring of heat from panel PV to heat the circulating water. This paper also discusses the comparison of output power and efficiency between heat recovered and a standard solar photovoltaic panel. The calculated maximum output power for heat recovered and standard solar PV system was 52.20W and 40.15W, with an efficiency of 11.72% and 9.65% respectively. The maximum temperature for the heat recovered system was 55.10˚C at 1.00 pm and the standard system was found at 62.30˚C. The experiment results show that stored water temperature in the reservoir able to reach 55˚C, within the range of a preferred liquid desiccant regenerator. Thus, it is possible to utilise the solar PV waste heat for desiccant solution regeneration and simultaneously benefit from the added benefit of improved efficiency.*

Keywords: *PV Temperature, Liquid desiccants, Waste heat, Solar panel, Cooling system*

Introduction

Numerous researches have been done to reduce the operating temperature of a solar PV to increase its efficiency and energy output. Proper cooling can improve the electrical efficiency, and decrease the rate of cell degradation over time, resulting in maximisation of the life span of photovoltaic modules. Usually, the heat removed from the solar panel is treated as waste heat and is rejected to the environment or is used on secondary applications such as for water heating. Solar air-conditioning using a liquid desiccant system is a possible application for solar PV waste heat utilisation. This system consists of a liquid desiccant dehumidifier unit and an evaporative cooling unit. Driving the fans pumping and regenerating desiccant throughout the regeneration process is the only energy used in this technique.

Liquid desiccants require lower regenerating temperature, mostly in the range of 40-900C (Kassem & Alisaimy, 2013; Ghafoor & Munir, 2015). Utilising solar energy for the desiccant regeneration process can save primary energy in the operation of a desiccant air cooling system. Thermal energy, at a temperature as low as 40–500C required for regenerating of the liquid desiccant can efficiently be obtained using a flat plate collector (Nesreen, Kamel

& Antoine, 2003). Low-grade energy sources can be utilised for regeneration (about 65–80°C). A solar desiccant cooling system can work with lower heat source temperatures from 60-70°C and have thermal COP over 1 (Fong & Chow, 2010). Solar desiccant cooling systems have the lowest heat source temperature and the highest thermal COP (Guo & Lin, 2017). A solar desiccant cooling prototype able to supply air temperatures as low as 11-12°C using heat source temperatures of 60-70°C provided by solar evacuated tube collectors (George & Gerald, 1988).

Several researchers (Fesharaki & Dehghani, 2011; Borkar & Prayagi, 2014; Fontenault, 2012; Sobhan, 2015) reported that the rise in PV cell temperature decreases its efficiency. Thus, solar cooling systems have been proposed (Krauters, 2004; Royne & Dey, 2005; Daghigh & Ruslan, 2011). There were many cooling techniques had been proposed from past research to overcome this overheating issue. Irwan (Irwan & Leow, 2015) tested the PV panel performance of an air-cooled solar PV and standard solar PV using DC brushless fan. The temperature of the PV panel with a DC brushless fan decrease 6.1 °C compared to the PV panel without a cooling system. While, the voltage, current and power had increased by 3.47%, 29.55% and 32.23% respectively. Catalin (Catalin & Sebastian, 2016) presented a numerical approach for temperature reduction of PV panel by using air-cooled heat sinks. The numerical model was analysed using ANSYS Fluent software for turbulent flow, and results are presented for the average temperature of the PV panel. Sobhan (Sobhan, 2015) designed and experimented with a hybrid photovoltaic/thermal (PV/T). The authors designed a parallel array of ducts with an inlet/outlet manifold for uniform airflow distribution. With the cooling mechanism, the temperature dropped significantly, leads to an increase in efficiency from 12% to 14%. It has been demonstrated that the solar PV module with the cooling system produces more energy than the non-cooling system. By using water, the temperature of the solar cells dropped by 8°C and the efficiency of the solar PV module increased by 3%. Naturally, the water cooling system has good potential in providing electricity and produce higher power output than the air cooling system (Ahmad, 2010; Colt, 2016; Sreejith & Rajesh, 2016). It shows that with the cooling system, it enhances the power generated.

The objective of this study is to investigate the probability of using solar waste heat to regenerate liquid desiccant in a solar air conditioning system thru the heating of circulated water and its effect on solar PV performance

Methodology

In this paper, a standard commercial PV module is converted to a hybrid PV system by adding a heat exchanger unit at its backside. This heat exchanger was designed and fabricated using copper tubes. Copper tubes are used for the fabrication of the device due to its better thermal conductivity and ease in fabrication. The copper heat exchangers are used as the waste heat recovery method to increase the temperature of water in the reservoir to a designated temperature. The components of the system include a water pump, piping, pipe insulation, copper tube, and a tank. The assembly of the copper heat exchanger on the solar PV back surface was simple and good contact was ensured to maximise heat transfer. Figure 1 shows the schematic drawing of the PV module and copper tubes assembly functioned as waste heat recovery from the solar panel.

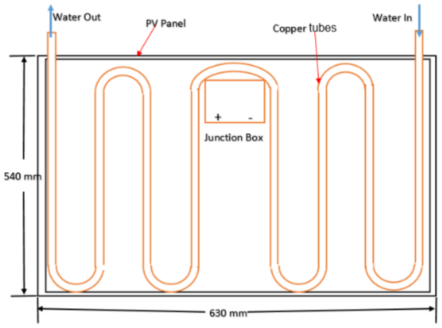

Figure 1. Solar Panel with Cooper Pipe System

In this experiment, the PV module used was the PVM-50 (mono-crystalline silicon) with maximum power (P_{mp}) 50 WP, open-circuit voltage (V_{oc}) 21.6 V, maximum power voltage (V_{mp}) 18 V, maximum system voltage DC 1000 V, maximum power current 2.8 A, (I_{mp}) 2.78 A, short circuit current (I_{sc}) 3.1 A, collector area 0.4288 m^2 and size 630 mm X 540 mm x 18mm. A 20W (water flow of 0.042 Kg/sec) water pump was used to circulate the water to the tank. The water flows to the heat collector, absorbing heat from the solar PV module and produces warm water which is measured using thermocouples. Solar PV power output and efficiencies were calculated using the following equation.

The power output for PV, $P_{out} = V_{oc} \text{ x } I_{sc}$ (1)
Electrical efficiency $\eta = I_m * V_m / Apvt * G$ (2)
Thermal efficiency $\eta = \dot{m} * C_p * (T_o - T_i) / Apvt * G$ (3)

η - efficiency, Apvt -Collector area [m2], G- Irradiance [W/m2], I_m – Max Current, V_m – Max Voltage, T_o - Collector outlet[°C], Ti - Collector inlet [°C], $\dot{m}$ - Mass flow rate [kg/s], C_p - Specific heat of Water [J/kg K]

The experiment was conducted in Universiti Malaysia Sabah, Kota Kinabalu at a location of 6.0367°N, 116.1186°E (Sukarno & Abd Hamid, 2015; Sukarno & Abd Hamid, 2017). The measurement was taken for two days which was on the 26th and 28th of August 2020, from 10.00 am to 3.00 pm period. The corresponding maximum global solar radiation was 1052.9 W/m² on 26th August 2020 at 2 pm whereas the highest hourly average was 970.17 W/m2 at 1 pm. A 50 W mono-crystalline photovoltaic panel module PVM-50 was used in this research. RTD-PT100 thermocouple was used to measure the temperature of the solar PV module, and a 5-in-1 environmental meter was used to measure the environment temperature. All readings were recorded manually for peak PV powerpoint. Readings of the inlet and outlet temperatures, water flow rate flowing through the heat exchanger were collected, which were further used to calculate the thermal power, PV efficiency, and performance ratio of the hybrid system. The heat exchanger comprises of 12 mm diameter copper tube, 8.5 meters in length and the pitch between two consecutive tubes was set at 75 mm. In this experiment, the measurement was taken to calculate the electrical power generated and thermal energy transferred to compare the effect of heat recovery on solar PV performance and water temperature. The tilt angle for the solar panel was inclined at the 15° facing to the southern hemisphere. A similar experiment was performed simultaneously without heat recovery systems for comparison purposes as shown in Figure 2. Whereas Figure 3 shows actual experimental work done to test the waste heat recovery system.

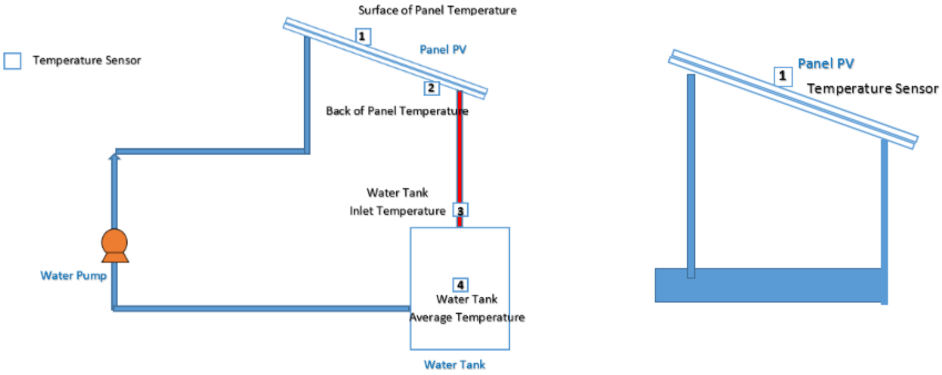

(a) (b)

Figure 2: Experimental Set-up of (a) Waste-heat recovery and (b) Standard System

Figure 3: Experimental Work on Waste-heat recovery system

Result and Discussion

Experimental Result

The study investigates the possibility of using a solar PV waste heat to regenerate liquid desiccant in a solar air conditioning system by observing the temperature of water in the tank, inlet water tank temperature and surface panel temperature. The measure and calculated experimental data are as shown in Table 1.

Table 1: Production of Solar Panel

Technical parameters	**Performance of PV (standard solar PV)**			**Performance of PV (heat recovered solar PV)**		
	Average	**Max**	**Min**	**Average**	**Max**	**Min**
Voltage (V)	18.16	19.12	15.60	19.34	20.53	18.00
Current (A)	2.02	2.10	2.00	2.09	2.36	2.08
PV power (W)	36.68	40.15	31.20	42.36	52.20	37.44
PV Efficiency (%)	10.11	13.18	8.49	12.24	15.22	11.06
Thermal efficiency (%)				21.95	33.77	20.68
Water Tank Average Temperature (°C) #4				50.23	55.50	40.10
Top module temperature (°C) #1	53.70	62.30	43.00	46.70	55.10	38.10

Thermal Behaviour

The surface temperature of both panels gradually increased and peaked at 1.00 pm as shown in Figure 4. International Journal of Renewable Energy Research Comparing the average surface temperature of these two setups also shows the cooler surface temperature of the solar PV with a heat recovery system. The maximum temperature for the cooling system (top surface) was found 55.10˚C at 1.00 pm while the temperature for the standard (top surface) system was 62.30˚C. This shows that with the heat recovery system, it can lead to an increase in conversion efficiency and power output of PV cells due to the reduction of the panel temperature.

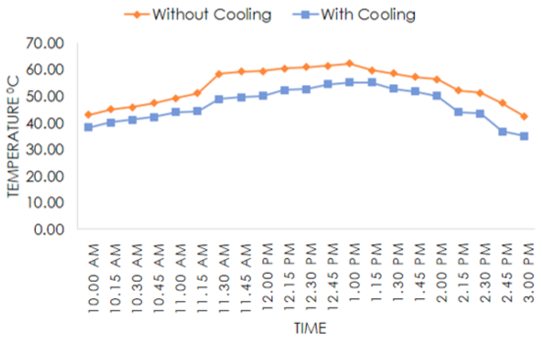

Figure 4: Surface Temperature of Solar PV

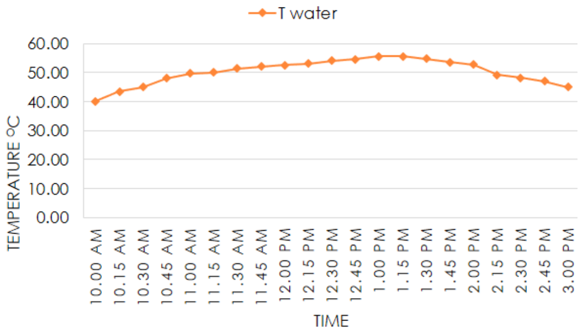

Figure 5: Water Temperature in The Tank

The temperature in the tank is as shown in Figure 5. The water temperature inside the reservoir initially starts at 40.10˚C early in the day and gradually increases to 55.5˚C. This is the result of heat recovery from the solar PV waste heat and it shows a stable profile before going down towards the afternoon. The average thermal efficiency for the heat exchangers was calculated at around 21.95%. The temperature achieves indicates that the waste heat recovery from a solar PV system is capable of being used to regenerate the liquid desiccant solution in a liquid desiccant air conditioning system.

Electrical Performance

Measured power output shows both panels generate power gradually in the morning and decrease in the afternoon due to the variance of solar radiation as shown in Figure 7. The power generated by the solar PV system with a waste heat recovery system produces better power output compared to the standard configuration and thus better efficiency as shown in Figure 8. This is expected as the cooler surface temperature would translate to better efficiency with maximum efficiency recorded at 15.22%. The total power produced by the system with a cooling PV panel is 261.43 Wh/d and a non-cooling PV panel is 212.76 Wh/d.

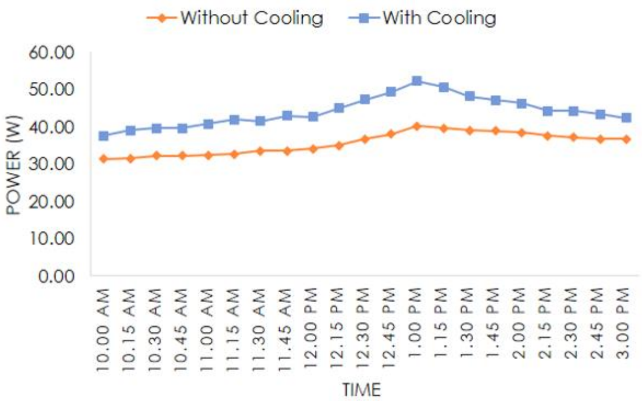

Figure 7: Power Output of Solar PV System

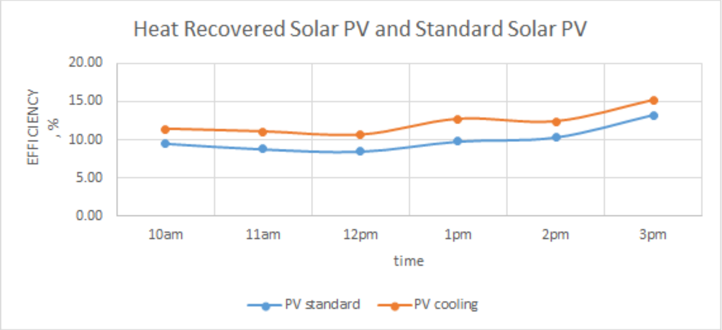

Figure 8: Efficiency of Solar PV system

Conclusion and Recommendation

In this study, a waste heat recovery system for a 50Watt solar PV was designed, fabricated and experimentally analysed. The experimental result shows that waste heat from solar PV was able to increase the temperature of the circulated water by 15.50°C and remain stable at 55.50°C. The temperature gained indicates that it is possible to use this setup to regenerate liquid desiccant solution for solar air conditioning system, which requires a minimum temperature of 40°C - 70°C to function effectively.

Waste heat recovery on solar PV also reduces the average operating temperature of the solar PV resulting and improvement in efficiency and power output. The maximum power output for the solar PV with heat recovery was 52.20 W while the standard solar PV was able to achieve 40.15W. Furthermore, this will benefit the system in terms of improved longevity and durability of the system.

Acknowledgement

The authors wish to convey sincere gratitude to Universiti Malaysia Sabah (UMS) for supporting the current research work thru the Acculturation research grant, project no. SGA0100-2019.

References

Borkar DS, Prayagi SV, Gotmare J. Performance Evaluation of Photovoltaic Solar Panel Using Thermoelectric Cooling.International Journal of Engineering Research. 2014; 3: 536-539.

C. S. Sreejith, P. Rajesh and M. R. Unni, “Experimental study on efficiency enhancement of PV systems with combined effect of cooling and maximum power point tracking”, International Conference on Inventive Computation Technologies, Coimbatore, India, 26-27 August 2016.

Catalin GP, Sebastian VH, Theodor DM, Nelu-Cristian C. Efficiency Improvement of Photovoltaic Panels by Using Air Cooled Heat Sinks. Energy Procedia. 2016; 425-432.

Daghigh R, Ruslan MH, Sopian K. Advance in Liquid Based Photovoltaics/Thermal (PV/T) Collectors. Renewable and Sustainable Energy Reviews.2011; 4: 4156-4170.

Fesharaki VJ, Dehghani M, Fesharaki JJ. The effect of temperature on photovoltaic cell efficiency. Proceedings of the 1st International Conference on ETEC. 2011.

Fong KF, Chow TT, Lee CK, Lin Z, Chan LS. Comparative study of different solar cooling systems for buildings in subtropical city'. Solar Energy 2010;84:227-44

Fontenault B. Active Forced Convection Photovoltaic/Thermal Efficiency Optimisation Analysis. Rensselaer Polytechnic Institute Hartford. 2012.

G. Colt, “Performance evaluation of a PV panel by rear surface water active cooling”, International Conference on Applied and Theoretical Electricity, Craiova, Romania, 6- 8 October 2016.

G. Nesreen, G. Kamel, N. Antoine, Use of desiccant dehumidification to improve energy utilisation in air-conditioning systems in Beirut, International Journal of Energy Research 27 (2003) 1317–1338.

George OGL, Gerald C, Thomas B. Performance of a solar desiccant cooling system. Journal of Solar Energy Engineering 1988;110:165-71.

Ghafoor A,Munir A (2015). Worldwide overview of solar thermal cooling technologies Renewable and Sustainable Energy Review vol.43 pp.763-764][2]Ghafoor et al, 2015

Guo J, Lin S, Bilbao JI, White SD, Sproul AB. A review of photovoltaic thermal (PV/T) heat utilisation with low temperature desiccant cooling and dehumidification. Renewable and Sustainable Energy Reviews 2017;67:1-14

H. Ahmad, “Phase Change Materials for Thermal Regulation of Building Integrated

Irwan YM, Leow WZ, Irwanto M, Fareq M, SIS, Hassan, Safwati I, Amelia AR. Comparison of Solar Panel Cooling System by Using DC Brushless Fan and DC Water. Journal of Physics: Conference Series 622. 2015; 1-10

K. Sukarno, A. S. Abd Hamid, J. Dayou, M. Z. H. Makmud and M. S. Sarjadi, “Measurement of global solar radiation in Kota Kinabalu Malaysia”, ARPN Journal of Engineering and Applied Science, vol. 10, No. 15, pp. 6467-6471, 2015

K. Sukarno, A. S. Abd Hamid, J. H. W. Chang, F. P. Chee and J. Dayou, "Comparison of Power Output between Fixed and Perpendicular Solar Photovoltaic Panel in Tropical Climate Region", Advanced Science Letters, vol. 23, No. 2, pp. 1259–1263, 2017

Kassem Talal K, Alosaimy Ali S, Hamed Ahmed M, Fazian Mohammad. Solar powered dehumidification systems using desert evaporative coolers: Review. International Journal of Engineering and Advanced Technology (IJEAT) 2013;3(1).ISSN: 2249 – 8958.

Krauters S. Increased Electrical Yield Via Water Flow Over the Front of Photovoltaic Panels. Solar Enegery Materials & Solar Cells.2004; 82. Photovoltaics” PhD thesis, Dublin Institute of Technology, Ireland, 2010.

Royne A, Dey CJ, Mills DR. Cooling of Photovoltaics Cells Under Concentrated Illumination: A Critical ReviewSolar Energy Materials & Solar Cells. 2005; 86: 451-483.

Sobhan D. Evaluating the Radiation and Temperature Effect on Photovoltaic Systems. Buletin of Electrical Engineering and Informatics. 2015; 4(1): 1-6.

International Research Conference on Applied Sciences and Engineering 2020
(IRCASE 2020)

ORGANIZING COMMITTEE

Chairman:
Ts. Dr. Wan Azani Wan Mustaf

Treasurer:
Zafira Zainudin

Technical Committee:
Norhaslinda Mohd Kamil

Technical Reviewer:
Asst. Prof. Dr. Raja Norshad Jamil
Dr. Ferial Ghaemi
Dr. Ali Tighnavard Balasbaneh

Liaison Officer:
Nuratikah Amid Dudin

Published by:
Global Academic Excellence (M) Sdn. Bhd.
(1257579-U)
KELANTAN, MALAYSIA

eISBN 978-967-2426-20-2
9 789672 426202

GAE'S CONFERENCES 2021

2nd PIMC 2021

2nd Penang International Multidisciplinary Conference 2021 (2nd PIMC 2021)
Date: 23-24 January 2021
Venue: Penang, Malaysia
Website: https://submit.confbay.com/conf/pimc2 @ http://2pimc2021.egax.org/
Email: pimcconferences@gmail.com; conference2@egax.org

4th ICGBSS 2021

4th International Conference on Global Business and Social Science 2021 (4th ICGBSS 2021)
Date: 20-21 February 2021
Venue: Kuala Lumpur, Malaysia
Website: https://submit.confbay.com/conf/4icgbss2021 @ http://icgbss2021.egax.org/
Email: icgbssofficial@gmail.com; conference2@egax.org

3rd LIMC 2021

3rd Langkawi International Multidisciplinary Conference 2021 (3rd LIMC 2021)
Date: 13-14 March 2021
Venue: Langkawi, Malaysia
Website: https://submit.confbay.com/conf/limc3 @ http://3limc2021.egax.org/
Email: limcconf2019@gmail.com; conference2@egax.org

6th ICEBIT 2021

6th International Conference on Education, Business, Islamic and Technology 2021 (6th ICEBIT 2021)
Date: 3-4 April 2021
Venue: Ipoh, Perak, Malaysia
Website: https://submit.confbay.com/conf/icebit6 @ http://icebit2021.egax.org/
Email: icebitofficial@gmail.com; conference2@egax.org

5th ICBTT 2021

5th International Conference Business, Tourism and Technology 2021 (5th ICBTT 2021)
Date: 24-25 April 2021
Venue: Online
Website: https://submit.confbay.com/conf/icbtt5 / http://icbtt2021.egax.org/
Email: icbttofficial@gmail.com; conference2@egax.org

3rd IRCMST 2021

3rd International Research Conference on Multidisciplinary in Social Sciences and Technology 2021 (3rd IRCMST 2021)
Date: 26-27 June 2021
Venue: Cameron Highland, Malaysia
Website: https://submit.confbay.com/conf/ircmst3 @ http://ircmst2021.egax.org/
Email: ircmstofficial@gmail.com; conference2@egax.org

4th ICTTBM 2021

4th International Conference on Tourism, Technology and Business Management 2021 (4th ICTTBM 2021)

Date: 1-2 August 2021
Venue: Kota Bharu, Kelantan, Malaysia
Website: https://submit.confbay.com/conf/icttbm4 @ http://icttbm2021.egax.org/
Email: icttbmofficial@gmail.com; conference2@egax.org

4th IRCHST 2021

4th International Research Conference on Humanities, Social Sciences and Technology 2021 (4th IRCHST 2021)

Date: 21-22 August 2021
Venue: Kuala Lumpur, Malaysia
Website: https://submit.confbay.com/conf/irchst4 @ http://irchst2021.egax.org/
Email: icgbssofficial@gmail.com; conference2@egax.org

3rd PIMC 2021

3rd Penang International Multidisciplinary Conference 2021 (3rd PIMC 2021)

Date: 25-26 September 2021
Venue: Penang, Malaysia
Website: https://submit.confbay.com/conf/pimc3 @ http://3pimc2021.egax.org/
Email: pimcconferences@gmail.com; conference2@egax.org

6th ICSHT 2021

6th International Conference on Social Sciences, Humanities and Technology 2021 (6th ICSHT 2021)

Date: 23-24 October 2021
Venue: Sabah, Malaysia
Website: https://submit.confbay.com/conf/icsht6 @ http://icsht2021.egax.org/
Email: icshtofficial@gmail.com; conference2@egax.org

4th LIMC 2021

4th Langkawi International Multidisciplinary Conference 2021 (4th LIMC 2021)

Date: 20-21 November 2021
Venue: Langkawi, Malaysia
Website: https://submit.confbay.com/conf/limc4 @ http://4limc2021.egax.org/
Email: limcconf2019@gmail.com; conference2@egax.org

5th ICIEL 2021

5th International Conference on Islamic, Education and Law 2021 (5th ICIEL 2021)

Date: 18-19 December 2021
Venue: Ipoh, Perak, Malaysia
Website: https://submit.confbay.com/conf/iciel5 @ http://iciel2021.egax.org/
Email: ircmstofficial@gmail.com; conference2@egax.org

GLOBAL ACADEMIC EXCELLENCE

"KNOWLEDGE FOR FUTURE"

admin@egax.org

www.egax.org

+6097406346
+60108428094

@GAExcellence

_GAExcellence

Global Academic
Excellence GAE

@gaesbofficial